CHANGES TO THE ELECTROLYTE IN AGED LI-ION CELLS

by

Lauren M. Thompson

Submitted in partial fulfillment of the requirements
for the degree of Master of Science

at

Dalhousie University
Halifax, Nova Scotia
August 2018

To my families in Kennebunk and Halifax,

TABLE OF CONTENTS

LIST OF FIGURES

ABSTRACT

Electrolyte composition is crucial to the lifetime, cycling capability and safety of Li-ion cells. Many studies have measured electrolyte changes after formation or during the first few charge and discharge cycles, while very few consider long-term changes that occur to Li-ion electrolytes. This work highlights some previous research and describes rigorous electrolyte analysis methods. The development of the electrolyte extraction method, which allows for the reconstruction of electrolyte composition, is discussed and applied to cells which have been cycled for many months.

The developed centrifuge and GC-MS/ICP-MS methods are presented in this work along with results from cells cycled to various upper cutoff potentials and from cells containing a low-viscosity co-solvent. Results from μ-XRF transition metal analysis of the negative electrode are also presented. The findings indicate some salt loss from electrolyte in cells cycled to the higher upper cutoff potentials and minimal Mn deposition found on the negative electrode. Potential reaction mechanisms to describe the observed changes are discussed and compared to previous studies. Now that the methods for rigorous analysis of the electrolyte have been established, many additional projects have been proposed as future work.

LIST OF ABBREVIATIONS AND SYMBOLS USED

CCCV	Constant current - constant voltage
DEC	Diethyl carbonate
DEOHC	Diethyl-2,5-dioxahexane carboxylate
DMC	Dimethyl carbonate
DMOHC	Dimethyl-2,5-dioxahexane carboxylate
DTA	Differential thermal analysis
DTD	Ethylene sulfate
EC	Ethylene carbonate
EI	Electron impact ionization
EIS	Electrochemical impedance spectroscopy
EMC	Ethyl methyl carbonate
EMOHC	Ethyl methyl-2,5-dioxahexane carboxylate
FEC	Fluoroethylene carbonate
FTIR	Fourier transform infrared spectroscopy
GC	Gas chromatography
GC-MS	Gas chromatography coupled with mass
ICP-MS	Inductively coupled plasma - mass spectrometry
KED	Kinetic energy discrimination
LCO	$LiCoO_2$
LEDC	Lithium ethylene dicarbonate
LiMO2	Lithium transition metal dioxide
LiOR	Lithium alkoxide
LiTFSI	Lithium bis(trifluoromethanesulfonyl)imide
MA	Methyl acetate
MEC	Methylene ethylene carbonate
MMDS	Methylene methanedisulfonate
MS	Mass spectrometry
NaCMC	Sodium carboxymethylcellulose
NCA	$Li(Ni_xCo_yAl_{1-x-y})O_2$
NMC532	$Li[Ni_{0.5}Mn_{0.3}Co_{0.2}]O_2$
NMC662	$Li[Ni_{0.6}Mn_{0.2}Co_{0.2}]O_2$
OE-MS	Online-electrochemical mass spectrometry
PES	Propene sultone
PP	Polypropylene
PTFE	Polytetrafluoroethylene
PVDF	Polyvinylidene fluoride

SBR	Styrene butadiene rubber
SEI	Solid electrolyte interphase
TCD	Thermal conductivity detector
VC	Vinylene carbonate
μ-XRF	micro-X-ray fluorescence

A^+	Cation fragment
AB	Molecule
$B^\bullet$	Neutral radical species
c_m	Concentration of compound in mobile
c_s	Concentration of compound in stationary
dQ/dV	Differential capacity
e^-	Electron
eV	Electron volts
I	Intensity
I_o	Initial intensity
k	Retention factor
K	Distribution constant
L	Length
M	Transition metal
m	Mass of an ion
M	Molecule
$M^{\bullet+}$	Radical cation of molecule
μ_l	Linear attenuation coefficient
n	Number of samples
Q_c	Charge capacity
Q_d	Discharge capacity
s	Standard deviation
t	Sample thickness
t_M	Projected travel time through column
t_R	Retention time of compound
t_R'	Delay due to stationary phase
$\bar{u}$	Average linear velocity of the mobile
V	Voltage
V_m	Volume of mobile phase
V_s	Volume of stationary phase
x	Individual instrument reading
$\bar{x}$	Average instrument reading
X	Halide
y	Confidence interval

z	Charge of an ion
z_t	Student's T value
β	Mobile phase to stationary phase volume

ACKNOWLEDGEMENTS

I would like to thank NSERC along with Tesla Canada for partial funding of this work.

I would like to thank my supervisor, Dr. Jeff Dahn, for his time, knowledge, guidance, feedback, encouragement and enthusiasm. I am very thankful for the opportunity to learn from him and to become a better research scientist. I would also like to thank Heather Andreas for her guidance and support as my committee member and as my professor. I would like to thank Giselle Andrews and Lea Gawne along with the graduate chemistry office for their help throughout my degree.

I would like to thank the members of the Dahn Lab, both past and present, for their continued support, knowledge and friendship. I am lucky to work with so many kind and hard-working people.

I would like to thank my family and friends in the chemistry department, in the city, in the states and next door for their love, support, visits, runs, inspiration and snacks throughout this degree.

I would like to also thank Dylan and Beta for their love, encouragement and laughs.

I am very thankful for all the support I have both here in Halifax and in Maine. I feel very fortunate to have made so many valued friendships.

1. CHAPTER 1 – INTRODUCTION

Justification

In Nova Scotia and beyond, individuals and governments are recognizing the long-term costs of non-renewable energy production and focusing emphasis on more renewable sources such as solar, wind, geothermal and hydroelectric.[1] Countries such as Iceland and Costa Rica produce close to 100% of their electrical energy from renewable sources and are investing in clean transport and smart grid technologies.[2] In 2013, Nova Scotia produced 20% of its electrical energy from renewable sources and will increase production to 40% by 2020.[1] To increase significantly beyond 40%, electrical energy storage devices are needed.[1]

The popularity of electric vehicles has increased dramatically over the past eight years as an alternative to fossil fuel-powered vehicles. In 2017, electric and hybrid vehicle production increased almost 60% from 2016.[3] Still, according to the International Energy Agency, renewable energy representation in the transportation sector is limited.[4] If electrical energy storage becomes less expensive, electric vehicles become more affordable and larger transport vehicles such as buses and trucks convert to clean energy, then this large gap in renewable energy implementation can be closed.

In order for renewable energy sources to attain wide implementation, electrical energy storage will be required on a large scale which may require multiple technologies such as pumped hydro, redox flow batteries, lithium-ion batteries, etc.[1,4,5]

Lithium-ion batteries are the most common portable rechargeable energy storage device available today. They can be tailored for small devices such as cell phones, laptops, and power tools as well as for large devices such as hybrid/electric vehicles, home energy storage and large-scale grid energy storage.[5] However, it is important to reduce their cost, and improve their lifetime, energy density and safety.[5,6]

The work presented in this thesis primarily focuses on studies associated with improving the lifetime of Li-ion cells. The studies included have been designed to help identify the mechanisms that lead to cell failure at elevated temperatures, with various electrolyte compositions and higher upper cutoff potentials. Once such mechanisms have been elucidated, they can hopefully be eliminated and extend cell lifetime.

Li-ion cells

Li-ion cells store electric energy in the form of electrochemical potential energy via Li^+ atoms transferred from one host structure to another.[6] Figure 1.1 shows a schematic of a Li-ion cell. Figure 1.1a shows the ion and electron movement during charge, where an electric current is provided to the cell, delivering electrons to the negative electrode (graphite). The added negative charge is balanced by positive charge which is delivered via Li^+ cations traveling through the electrolyte and intercalating between the graphite layers.

During this time, the change of lithium content in the electrode materials causes the positive and negative electrode potentials to change as shown Figure 1.2. During a charge of a Li-

ion cell, the lithiated negative electrode experiences a decrease in potential to about 0.08 V vs. Li/Li^+ upon intercalation (red line) while the delithiated positive electrode

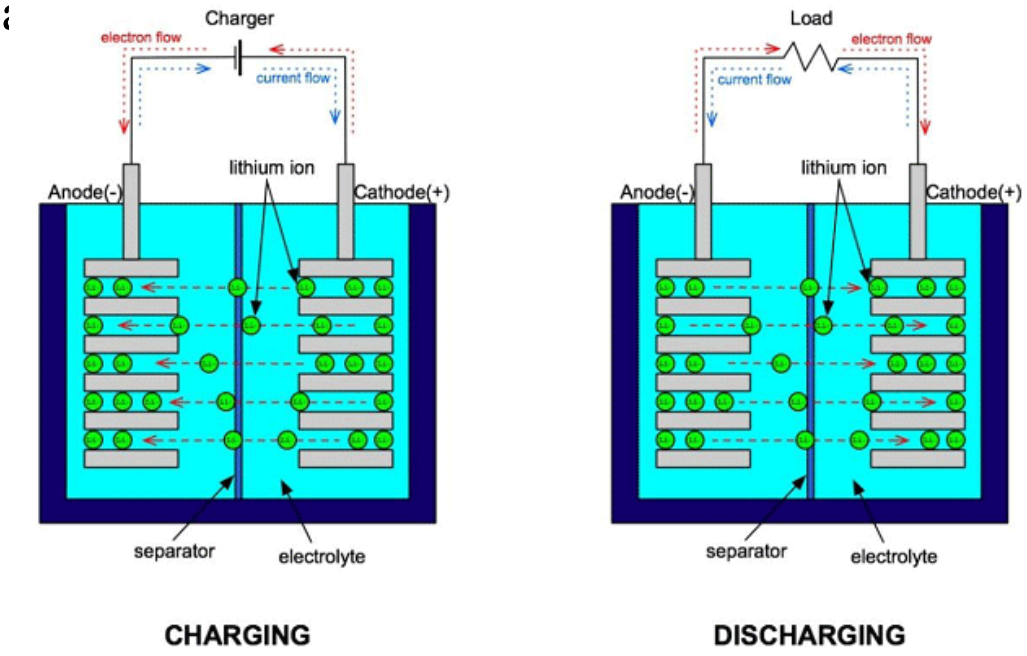

Figure 1.1 - a.) Li-ion cell during charging. b) Li-ion cell during discharging.[7]

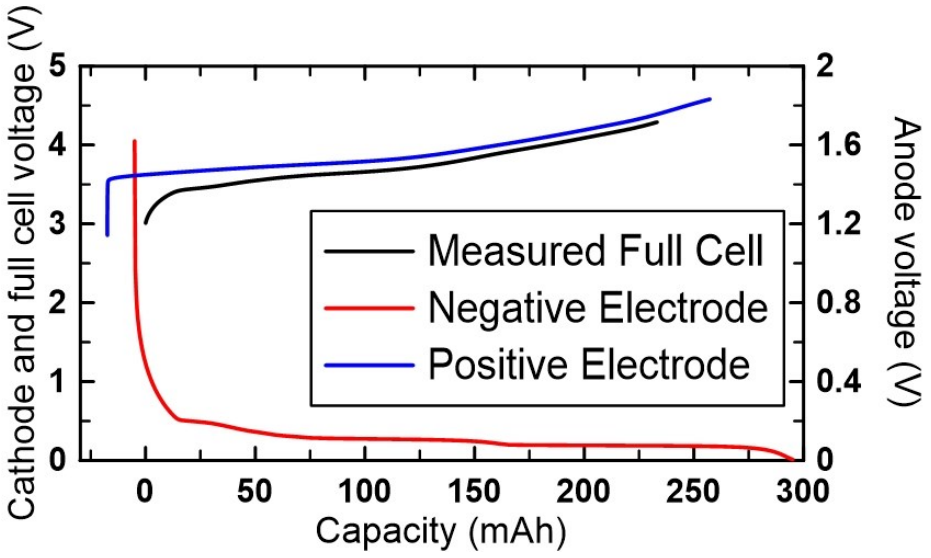

Figure 1.2 - Calculated potential vs. capacity plots for full cell (black), positive electrode (blue) and negative electrode (red) vs. Li/Li^+.[8]

experiences an increase in potential, up to 4.3 V vs. Li/Li^+ (blue line). The difference between these potentials determines the potential of the full Li-ion cell (black line).

During discharge, Li-ions will leave the graphite electrode travel through the electrolyte and intercalate back into the positive electrode as shown in Figure 1.1b. The flow of Li^+ ions prompts the flow of electrons from the negative electrode to the positive electrode and results in current generation along the external circuit. In response, the potential of the positive electrode decreases and the potential of the negative electrode increases until the lower discharge potential is reached (Figure 1.2).

Figure 1.3 shows a schematic of a wound cell and its components that will be discussed below. As shown, the negative and positive electrodes, which are separated by a separator, are wound together as a 'jelly roll' in a case (either a can for a cylindrical cell or a pouch bag for a pouch cell). Figure 1.3 shows a profile view of the jelly roll with the outer layers of electrodes unwound. The electrodes are both connected to separate tabs at the end of the wound cell for charging and discharging.

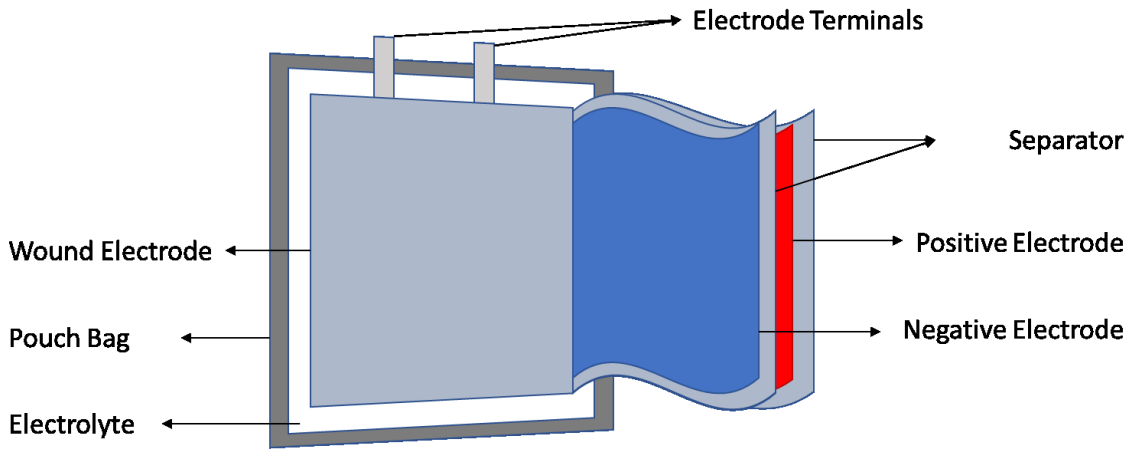

Figure 1.3 - Simplified diagram of a wound pouch cell.

Negative electrode

Li-ion cell negative electrodes are comprised of mainly graphite and small amounts of binder and conductive additive. Graphite is a layered material in which Li-ions can intercalate and the binder and conductive additive ensure that the graphite particles are adhered to and are electrically connected to the copper current collector.[6] The negative electrode is indicated in Figure 1.3.

Silicon has also been studied as a potential anode material due to its larger theoretical specific capacity (3579 mAh g^{-1} compared to 372 mAh g^{-1} for graphite) however it experiences extreme volume expansion upon alloying with lithium (up to 300%) and, consequently, possible loss of electrical connection during contraction when lithium is removed.[6] Nevertheless, Si and Si-containing materials are being incorporated at up to 10 or 20% by weight along with graphite in some high energy density Li-ion cells.

Positive electrode

Positive electrodes typically consist of a lithium transition metal dioxide ($LiMO_2$), a binder and conductive additive. The $LiMO_2$ (M = transition metal(s)) usually takes a layered structure also allowing for Li-ion insertion, although spinel or olivine structures are also found in some commercial Li-ion cells. The binder and conductive additive also ensure good connection to the aluminum current collector and electrical connectivity.[6] The positive electrode is indicated in Figure 1.3.

The transition metals used have been studied extensively over the course of Li-ion battery development. Cobalt was found to give large capacity, high stability and safety,[6] in $LiCoO_2$

(LCO) however, the material costs have almost quadrupled in the past two years in addition to significant social costs.[9] Many Li-ion positive electrode materials now substitute a mixture of transition metals (such as Ni, Mn and Co) to balance performance with cost.[5] These mixtures are designated by their molar percent, for example, $Li(Ni_{0.5}Mn_{0.3}Co_{0.2})O_2$ (NMC532) contains 50% Ni, 30% Mn and 20% Co.

Electrolyte

As mentioned above, the electrolyte (indicated in Figure 1.3) facilitates the exchange of Li-ions between the negative and the positive electrode. A typical electrolyte mixture must be ionically conductive, electrically insulating and must limit parasitic reactions between the electrolyte and the charged electrode materials. Using a good electrolyte is a cost-effective way to improve cell performance and lifetime.[10]

The ionic conductivity of an electrolyte originates from the dissolved salt. The most common salt in Li-ion cells is lithium hexafluorophosphate ($LiPF_6$), which is highly soluble, imparts high ionic conductivity and is available at low cost. However, $LiPF_6$ can decompose at elevated temperatures and it can also react with trace amounts of water to form unwanted products like HF.[6,10]

A mixture of carbonates is typically used as the solvent. Such a mixture can have a dielectric constant high enough to dissolve and dissociate the salt, an electrochemical stability window larger than the electrode operating potentials and a low viscosity to maximize ionic conductivity and Li-ion diffusion. Suitable electrolytes are liquid over the expected operating temperature range of the cell. The carbonates most commonly used are

ethylene carbonate (EC), ethyl methyl carbonate (EMC), dimethyl carbonate (DMC) or diethyl carbonate (DEC).[10]

A more detailed description of electrolytes for Li-ion cells and observed unwanted reactions with charged electrode material surfaces is discussed in Chapter 2.

Solid electrolyte interphase (SEI)

EC or electrolyte additives are used for their ability to preferentially reduce at the negative electrode to form a stable layer at the interphase between the electrode and electrolyte. To be more specific, they react with Li^+ and e^- to form Li-containing products as well as other products. This layer of reaction products is called the solid electrolyte interphase (SEI) and is arguably the most important component of Li-ions cells designed for extended lifetime and good capacity retention.[6] It is desirable that this layer be stable with time and temperature, have a low resistance and to prevent, or at least dramatically hinder, unwanted reactions between the electrode and the electrolyte.[10] This layer is not shown in Figure 1.3, but is estimated to form a layer ~25 Å to ~100 Å thick on the negative and positive electrodes.[10]

Separator

Li-ion electrodes are often stacked or wound together in the cell as shown in Figure 1.3. To prevent contact and potential short circuits between charged electrodes, a microporous separator, usually made of polypropylene and/or polyethylene provides a barrier for

electrical contact while still allowing electrolyte to permeate. The layer also provides safety from overheating by the polyethylene layer, which at 135°C will melt, closing the micropores, hence blocking ion transport.[6]

Methods to improve Li-ion technology

Current strategies used to improve Li-ion cell energy density, lifetime, cost and safety include modifying or changing the electrode materials and changing the electrolyte with special attention to the additives. Through salt, solvent and additive choice, it is possible to take less expensive and moderately decent electrodes and increase the upper cutoff voltage to increase energy density or extend cell lifetime, thereby decreasing the effective cost.[10]

The work presented in this thesis aims to identify the electrolyte degradation reactions that occur in aged cells and to examine how increasing the upper cutoff potential affects these reactions. Findings will help guide future electrolyte designs to extend Li-ion lifetime and increase energy density.

Outline of thesis

Chapter 2 discusses current electrolytes and known reactions that occur in short-term testing.

Chapter 3 discusses the electrolyte analysis methods developed and applied for the studies of aged cells in this work.

Chapter 4 discusses results from NMC532 cells cycled at various upper cutoff voltages. This work was submitted to the Journal of the Electrochemical Society for publication on June 28, 2018.

Chapter 5 discusses results from NMC532 cells cycled at various upper cutoff potentials and containing different electrolytes.

Chapter 6 summarizes findings from Chapter 4 and Chapter 5 and introduces future work underway and planned.

2. CHAPTER 2 – ELECTROLYTE REACTIONS IN LI-ION CELLS

Lithium-ion transport is critical to the operation of Li-ion cells. In the electrolyte, the salt concentration, solvent choice and additive mixture are carefully designed to maximize cell performance. Li-ions must transport between the negative electrode and the positive electrode easily, as measured by conductivity and Li-ion diffusivity.[10] The salt choice influences cost, conductivity, Li-ion diffusivity and moisture sensitivity as well as electrochemical and thermal stability. The solvent choice is important to allow for adequate conductivity as well as stability within the electrochemical potential windows of both the positive and negative electrodes. Additives can be chosen to preferentially reduce at the negative electrode to form the protective negative electrode SEI to extend lifetime. The electrolyte must be electronically insulating to prevent direct self-discharge.[10] Preferably these components would be available at low cost, be safe for the user, the manufacturing process and the environment.[10] Lastly when the salt, solvent and additive(s) are combined, they would ideally remain inert toward each other.[10] A well-designed electrolyte system can expand the operating potentials of a cell to increase the energy density of the cell.[10]

Current electrolyte systems

Understanding the development of electrolytes currently used in Li-ion cells exemplifies the physical, electrical and thermal requirements needed for an effective electrolyte system.

Current common systems use $LiPF_6$ in an EC and EMC solvent blend. Additives can be included to improve SEI, safety and cycling properties.[10]

Salts considered for Li-ion cells should have good stability in the solvent solution and should transport Li-ions with minimal resistance. The salt should be electrochemically stable within the operating potentials and thermally stable within the operating temperatures. Ideally, the salt would be low cost, non-toxic and non-reactive towards other cell components.[10]

The most common salt used in non-aqueous Li-ions cells is $LiPF_6$. $LiPF_6$ has been used in Li-ion technology since the 1990s[10] and has been the salt of choice for a combination of properties. Some anions of salts studied were found to be too strong of a Lewis acid (such as AlX_4^-, X = halides) or Lewis base (such as Br^- or I^-).[10] Other salts that have been studied and that had promising cycling performance include lithium bis(trifluoromethanesulfonyl)imide (LiTFSI) and $LiAsF_6$. These were found to be stable,[11,12] however, LiTFSI did not prevent corrosion of the aluminum current collector, causing aluminum dissolution and solid products which increase cell impedance[13] and potentially causing the electrode material to separate from the current collector. $LiAsF_6$ had good conductivity and was not reactive with the current collector but could be very toxic in the As^{3+} and As^0 oxidation state.[10,14] While $LiPF_6$ does not have the best conductivity, dissolution, thermal stability nor electrochemically stability, it has an acceptable blend of these characteristics.[15] $LiPF_6$ is electrochemically stable up to 4.4 V vs. Li/Li^+ on glassy carbon substrates[10,14] and is less reactive toward the aluminum current collector than LiTFSI.[10,16] $LiPF_6$ is thermally stable at room temperature, however its

decomposition products, LiF and PF_5, become more favored at elevated temperatures and are hence increasingly available to react with solvent.[10,17]

The reactivity of $LiPF_6$ toward water can be problematic as a decomposition product, HF, is acidic and can create problems in Li-ion cells.[16,18] Therefore, electrolytes containing $LiPF_6$ are normally handled under extremely dry conditions, although there have been reports that water added intentionally to Li-ion cells can actually improve their behavior.[19,20] (Potentially from the basic environment created which limits PF_5 production as will be discussed below.) $LiPF_6$ manufacturers are able to produce the salt with high purity and low amounts of water content.[18,21,22]

The salt concentration of an electrolyte is normally chosen to maximize ionic conductivity and Li^+ ion diffusivity. The conductivity and diffusivity are influenced by both the dielectric constant and viscosity of the electrolyte and the diffusivity is also influenced by the Li^+ ion transference number. The dielectric constant, or relative permittivity, quantifies the reduction in force between charged particles in a medium compared to a vacuum. This effectively measures the ability of a solvent to dissolve ionic species. The viscosity measures how easily a fluid flows or how easily objects can flow through a fluid. An electrolyte with a high dielectric constant combined with a low viscosity typically has high conductivity.

As the concentration of salt in solution increases, the ionic conductivity increases until a maximum value. The conductivity then decreases because further increased salt content dramatically increases solution viscosity which hinders ionic motion.[23,24] At higher concentrations ion-pairing amongst the ions can occur which can further decrease

conductivity. However, Logan et al. have shown that in the electrolyte systems considered in this thesis the concentrations are low enough that ion pairing is not occurring.[24,25]

The electrolyte conductivity and viscosity are temperature dependent and can be tailored by changing solvents and salt concentration for specific applications and operating temperature ranges. Typically, a temperature increase causes the viscosity to decrease, allowing for a higher salt concentration and higher conductivity to be achieved as shown in Figure 2.1.[10,26]

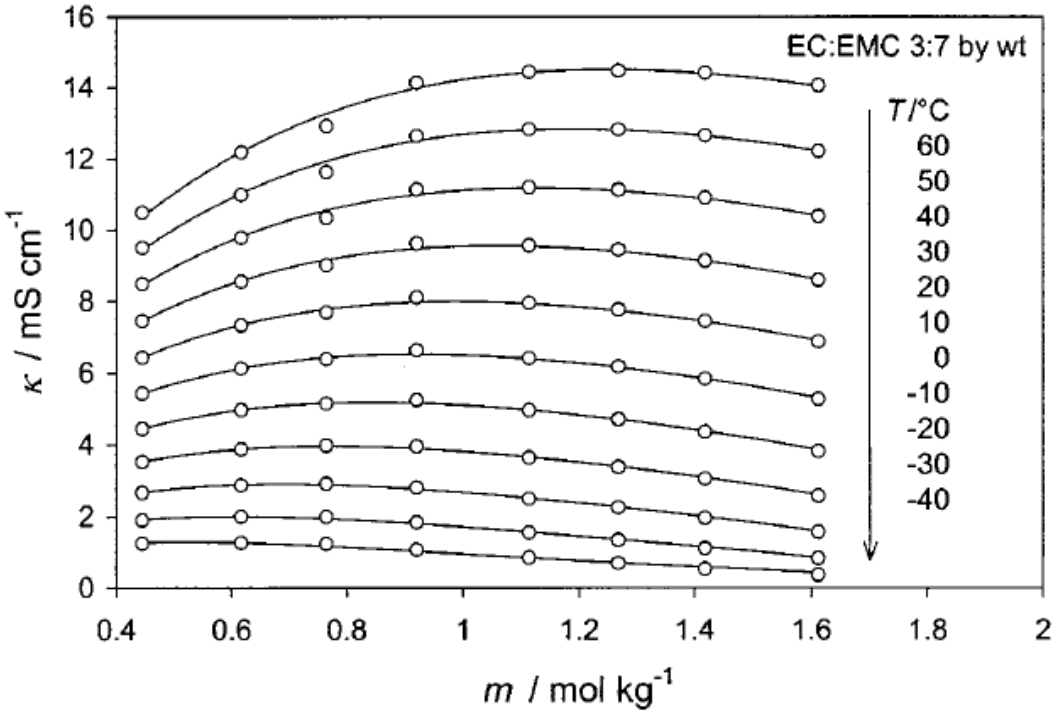

Figure 2.1 - Figure from a 2001 publication by Ding et al.[26] shows the conductivity (k) vs. molal concentration (m) of $LiPF_6$ in EC:EMC (3:7) at various temperatures (T). Reproduced with permission from *J. Electrochem. Soc.*, **148**, A1204 (2001). Copyright 2001, The Electrochemical Society.

Solvents currently used in Li-ion cells are typically a mixture of cyclic and linear carbonates. Linear carbonates generally have a low viscosity but a low dielectric constant. A typical linear carbonate is EMC which was chosen for its electrochemical stability window,[27] low viscosity and low melting point. Pure linear carbonates will reduce on the negative electrode at ~0.8 V vs. Li/Li^+.[28] Figure 2.2 shows the differential capacity (dQ/dV) peak corresponding to the reduction of EMC when the full cell is at 3.2 V, or the negative electrode is at ~0.4 V vs. Li/Li^+. However, linear carbonates do not produce a sufficiently stable SEI.[28] EC was found by Fong et al. to passivate the graphite anode effectively by developing a suitable SEI.[29] EC also has a large dielectric constant and is capable of dissolving $LiPF_6$ to at least 4 M. However, EC has a melting point of ~36°C so it is necessary to use an additional solvent such as a linear carbonate to depress the melting point. Such a solvent mixture retains the positive characteristics of EC and linear carbonates[10] while remaining a liquid over a wide temperature range.

Additives are also currently used to improve SEI stability and to prevent/hinder unwanted parasitic reactions in cells.[28,30-33] Additives are included in electrolyte in small quantities to minimize changes to the bulk properties of the electrolyte but gain the advantages in lifetime, stability, safety, etc. and minimize capacity loss.[10] Additives that have been studied previously and found to be effective include fluoroethylene carbonate (FEC), vinylene carbonate (VC), propene sultone (PES), and ethylene sulfate (1,3,2-dioxathiolane 2,2-dioxide, also abbreviated as DTD). In this thesis the additive system includes FEC and DTD.

.

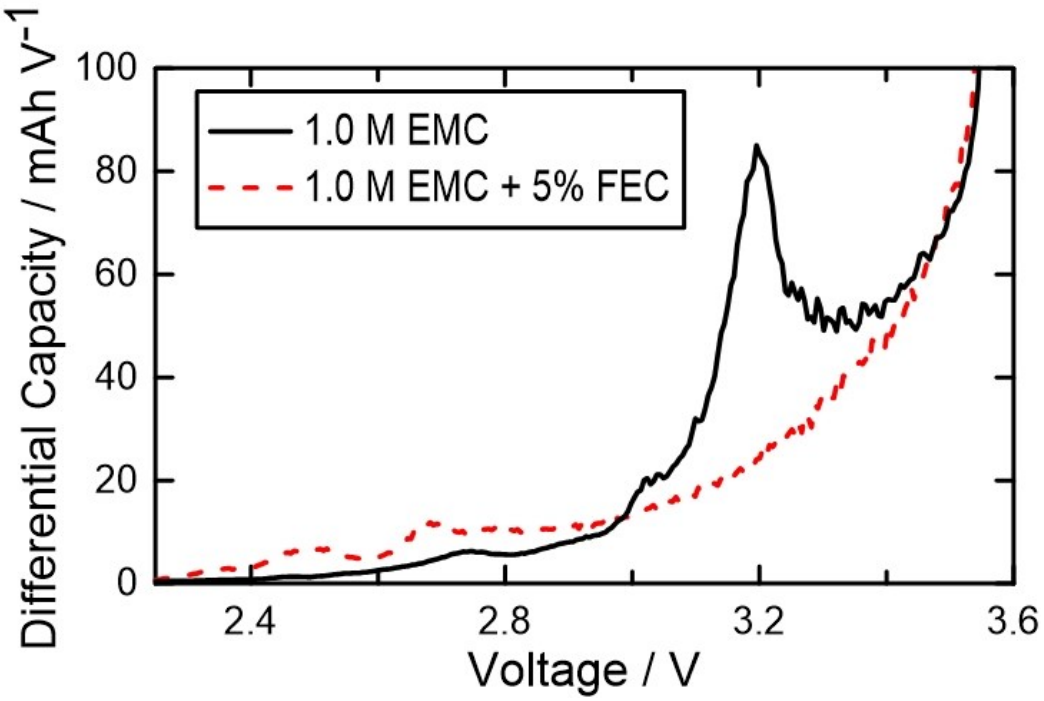

Figure 2.2 – Reproduced from Ma et al.[28] The differential capacity is shown as voltage increases for cells with 5% FEC and without FEC. The cell with no FEC (black) shows an EMC reduction peak around 3.2 V vs. graphite. The cell with FEC (red) reduce at a lower voltage of about 2.5 V vs. graphite. Reproduced with permission from *J. Electrochem. Soc.*, **164**, A5010 (2017). Copyright 2017, The Electrochemical Society.

Ideally an electrolyte used in a lithium-ion cell would not change for the lifetime of the cell. However, these electrolytes are subjected to physical changes and electrochemical and chemical decomposition reactions over the course of cell charge-discharge cycling which can result in changes to electrolyte composition. Very little is known about the changes that occur to the electrolyte during cell cycling or storage and their potential effects on cell lifetime.[34]

Long-term electrolyte solution changes could originate from reduction, oxidation or decomposition of the electrolyte, subsequent reactions of these reaction products and

changes to the surfaces of the electrode materials. Reactions that are kinetically hindered could occur over longer time frames such as months or years.[31,35,36] Previous studies have identified some of the oxidation and reduction products, decomposition products as well as products of some subsequent reactions that occur in the short-term at elevated temperatures or on poorly passivated electrodes. In the next sections, previous findings of studies on electrolyte reactions are reviewed. Subsequent reactions between reaction products are also discussed. This information is included to help understand some of the long-term changes observed in Li-ion electrolytes in aged cells.

Electrolyte reduction

Electrolyte will reduce at the negative electrode during the first charge of a Li-ion cell as the negative electrode reaches lower voltages vs. Li/Li^+.[28] This is shown in Figure 2.2, where peaks in dV/dQ vs. V occur and the corresponding voltage of the negative and positive electrodes is given in Figure 1.2. A well-designed electrolyte may contain a specific amount of sacrificial additive that can reduce at a higher voltage (vs. Li/Li^+) to modify the SEI formed and extend lifetime. Next, the reduction mechanisms of the bulk electrolyte (including EC, linear carbonates and additives) will be discussed.

The reduction of EC is expected to either occur via one or two electrons[31,33] as shown in Figure 2.3, routes (a.) and (b.). These reduction reactions typically create a radical carbonate anion intermediate by the first reduction steps for EC.[10] The radical species will then combine with another formed radical species to terminate the reaction. The radical species shown in these reduction reactions for EC, as well as the reduction reactions for

linear carbonates, can also combine to form many additional species not shown in these reaction examples.

The one electron reduction is outlined in route (a.) where the radical carbonate anion combines with the carbonate of a second radical carbonate anion to form an ethylene dicarbonate anion. The products of this reaction include lithium ethylene dicarbonate (LEDC), a solid contributing to the SEI, and ethylene gas.[37] LEDC is effective for passivating the negative electrode.[10,37] The stability of LEDC is expected to originate from the coordinated network of organic carbonate and lithium ions.[31,33,37]

Via the same radical carbonate anion intermediate as above, an additional gained electron and lithium ion would form Li_2CO_3 solid in the SEI and ethylene gas as shown in route (b.). In an alternative reduction mechanism shown in route (c.) where the proposed acyl radical intermediate occurs on the central carbon. This would then combine with an additional electron and Li^+ ion to form CO gas and lithium 1,2-ethanediolate.[38] Ethylene was found to be the main reduction product of EC (four times larger than the CO production) which indicates the reduction reaction favors route (a.).[31] In addition to LEDC and Li_2CO_3 that form during SEI formation, it has also been shown that EC can reduce to form lithium alkoxides, LiF (when combined with $LiPF_6$), $LiOCO_2R$, and polycarbonates on the negative electrode.[31,37,39]

Proposed linear carbonate reduction reactions are shown in Figure 2.3, routes (d.) and (e.). In route (d.), the linear carbonate combines with one electron to form an alkyl carbonate and Li-alkoxide.[33] However, it has also been shown that linear carbonates can also follow a two electron reduction pathway.[40] Linear carbonates can reduce to form CO and Li-alkoxides via a carbon radical intermediate route (e.).[41] Additionally, it is possible that the

carbon radical intermediate can react with other radical hydrogens or alkyl groups to form esters.[41,42]

Additives used can also reduce at the anode. Some claim that improved SEI and cycle life can be attributed to preferential additive reduction products on the anode and the lower impedance that can result.[31,43] The products forming a solid contributing to the SEI are no longer in solution and any gas not removed in the formation gas removal step described in Chapter 3 can partially dissolve in the electrolyte according to Henry's law. The liquid products formed in the reduction reactions discussed above can continue to react in the cell. Particularly reactive are the lithium alkoxides formed from the reduction of linear carbonate as shown in Figure 2.3, routes (d.) and (e.).

Lithium alkoxides are nucleophiles able to attack the carbon of the carbonate.[41,44,45] The alkoxide can perform an ester exchange reaction known as transesterification on both linear and cyclic carbonates via the more positively charged central carbon of carbonates and stabilized intermediate containing delocalized charge from oxygen atoms.[40] An additional source of lithium alkoxides originates from the nucleophilic reaction of lithium 1,2-ethanediolate (produced via route (c.)) and a linear carbonate to form EC and two additional lithium alkoxides.[40,41] Overall, this would cause EC to be reformed from the original reduction reaction as well as CO gas and two lithium alkoxides to be formed.

Products of electrolyte reactions with lithium alkoxides include substituted alkyl groups as well as the dimerization of EC to form alkyl-dicarbonates.[42] For an electrolyte system initially containing EC and EMC, the transesterification products are expected to be DMC and DEC and the dimerization products are expected to be dimethyly-2,5-dioxahexane

Reduction of EC	Subsequent Reaction	Route
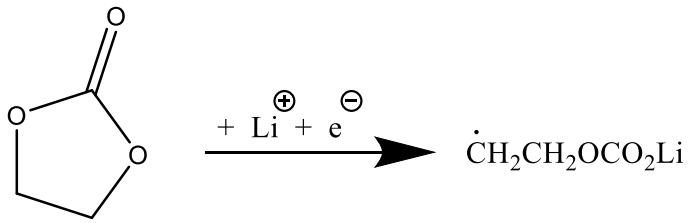		a.[33,37]
		b.[33]
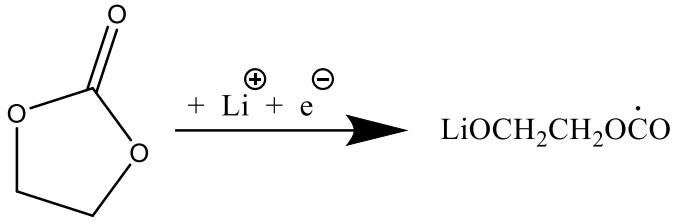		c.[33]
Reduction of Linear Carbonate	**Subsequent Reaction**	
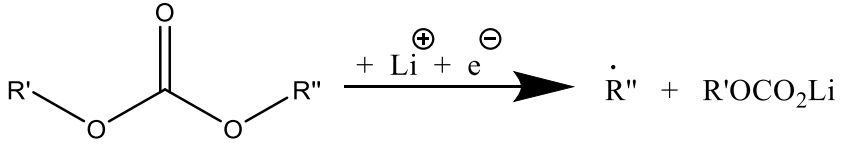		d.[40]
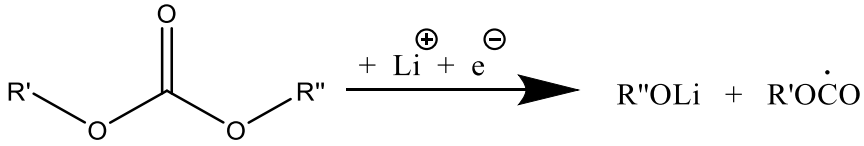		e.[40]

Figure 2.3 - Reduction reactions of linear carbonates (routes a., b. and c.) and cyclic carbonate, EC (routes d. and e.).

carboxylate (DMOHC), diethyl-2,5-dioxahexane carboxylate (DEOHC) and ethylmethyl-2,5-dioxahexane carboxylate (EMOHC). These reactions are further illustrated in Chapter 4.

In 1997, Takeuchi et al. and Yoshida et al. found that transesterification only occurred at graphite electrodes at low potential and not on the uncharged electrode.[41,44] Yoshida et al. proposed that the lithium alkoxide products from the reduction of EC and linear carbonates could facilitate transesterification.[41] In 2005, Sasaki et al. used half cells to show that the transesterification reaction was dependent on the presence of Li-alkoxides by exposing electrolyte mixtures to added Li-alkoxide and monitoring the products.[40] They found that no transesterification or dimerization occurred without the added alkoxide. It was also shown that the reaction occurred even without the presence of $LiPF_6$, however it did proceed faster with the addition of salt which was attributed to the Lewis acidity of the decomposed PF_6^- (PF_5) enhancing the positive charge densities on the carbonate.[40] As suggested from earlier findings that the ester exchange reactions were reversible,[44] Sasaki et al. also found that the dimerization products could decompose to EC and linear carbonate in the presence of alkoxides.[40] Similarly, the formation of DMC and DEC from EMC will proceed until equilibrium is reached.

The extent of transesterification and dimerization in cells is affected by the passivation of the anode via SEI formation, the charge and discharge current as well as the operating potential of the cell.[44,46] The alkyl dicarbonates formed from the dimerization reaction are generally unwanted as these compounds are more viscous and would therefore cause a decrease in electrolyte conductivity.[40]

Minimizing Li-alkoxide formation

Additives for Li-ion cells have been shown to minimize lithium alkoxide formation and their subsequent reactions,[28,31] however, the mechanism by which this is achieved is still debated. Most additives are thought to form a more stable SEI layer at a higher potential (vs. Li/Li^+) than electrolyte solvents on the negative electrode which prevents additional solvent from reducing at the surface.[28] Other additives are thought to scavenge lithium alkoxides from solution.[31,47]

In 2017, Ma et al. used the differential capacity in response to voltage to show that the additives, such as VC, FEC and methylene ethylene carbonate (MEC) will characteristically reduce at higher potentials (vs. Li/Li^+) than the bulk solvent[28] and effectively passivate the negative electrode. This will prevent the bulk solution from forming Li-alkoxides and no transesterification was measured in the electrolyte after cell formation.[30,31]

Petibon et al. also showed that excess FEC (up to 10%) can preferentially react with lithium alkoxides in solution before linear carbonates or cyclic carbonates (shown in Equation 2.1).[47]

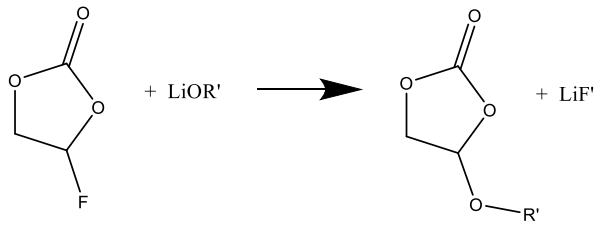

(2.1)

In their study, it was found the onset of transesterification and drastic capacity fade did not occur until all FEC was consumed by Li-alkoxides.[47] The higher reactivity of FEC with

Li-alkoxide compared to EC was attributed to the presence of the electron-withdrawing fluorine atom on the carbon ring.[47]

Strehle et al. also studied Li-alkoxide generation on graphite electrodes with VC as an additive. Using online-electrochemical mass spectrometry (OE-MS), they measured the gases produced by the electrochemical cell in real time.[31] The electrolyte used was 1.1 m $LiPF_6$ in EC:EMC (3:7) with and without VC added in various fractions. Carbon monoxide production was monitored to quantify Li-alkoxide formation from the reduction of EMC. It is important to note that the reduction of EC via route (c.) in Figure 2.3 also produces CO. Ethylene production from EC (as shown in Figure 2.3, routes (c.) and (d.)) was monitored to measure the reduction of EC. The reduction of VC was monitored by CO_2 production.[31] VC had been shown to reduce to produce CO_2 and an alkoxide radical which can react with an additional VC molecule to form a stable oiligomer or polymer of VC.[43]

The gas monitoring in this study showed that the addition of VC caused an initial increase in CO_2 production, suppressed C_2H_4 production, but still produced CO from the formation of Li-alkoxides. Pure CO_2 was then used as an additive to the electrolyte without VC and showed that CO_2 consumption lead to a decrease in transesterification products. Previously CO_2 had been used to improve the SEI layer at the anode.[33,48] They therefore attributed the improved performance in the presence of VC to the formation of CO_2 and its scavenging of lithium alkoxides. Similarly, Zhang proposed that CO_2 could react with a lithium alkoxide to form insoluble $LiOCO_2R'$.[33]

This study by Strehle et al. proposes an interesting mechanism for the effectiveness of VC, yet some important considerations such as quantification and experimental set up remain. For example, in Strehle et al.'s Figure 4, the amount of transesterification is completely

suppressed with the addition of 2 % VC while the addition of CO_2 only reduces the transesterification by 2/3.[31] Strehle et al. also attributed CO production to the reduction of linear carbonate, however in another study which characterized the gas produced from cells containing increasing amounts of VC (from 0 % to 6 %), the volume of CO gas produced increased with VC content.[49] Therefore, it could be that some of the CO produced in the study by Strehle et al. originates from VC rather than the reduction of the solvent.

Finally, as will be discussed below, recent research has discovered the importance of chemical dialog between the negative and positive electrodes. Therefore, many of the electrolyte-electrode reaction mechanisms are potentially missing when Strehle et al. only consider the effect of an additive on one electrode.

Decomposition of $LiPF_6$

While $LiPF_6$ has good stability compared to the other salts discussed above, at elevated temperatures and in altered chemical environments the stability decreases. In such situations, $LiPF_6$ can decompose to form PF_5 and LiF according to Equation 2.2.[42,50]

$$\mathrm{LiPF_{6\,(sol)}} \leftrightarrow \mathrm{LiF_{(s)}} + \mathrm{PF_{5\,(sol)}} \qquad (2.2)$$

Especially at elevated temperatures (higher than 60°C), $LiPF_6$ can act as a major catalyst for electrolyte, electrode, SEI and surface layer decomposition.[10,17] The product PF_5 is a strong Lewis acid, capable of accepting an electron pair.[51]

In the presence of trace water, $LiPF_6$ will also decompose (Equation 2.3) .

$$\mathrm{2\,H_2O_{(sol)}} + \mathrm{LiPF_{6\,(sol)}} \leftrightarrow \mathrm{LiPO_2F_{2\,(sol)}} + \mathrm{4\,HF_{(sol)}} \qquad (2.3)$$

As discussed in "current electrolyte systems" section, the implementation of $LiPF_6$ in Li-ion cells was initially limited by the purity of salt available from manufacturers. Excess water in salt received from a manufacturer or water contamination of a cell can result in unwanted $LiPF_6$ and PF_5 reactions (Equation 2.3 and Equation 2.4) .

$$PF_{5(sol)} + H_2O_{(l)} \leftrightarrow POF_{3(sol)} + 2\,HF_{(sol)} \quad (2.4)$$

Products of these reactions include HF, a strong acid, POF_3 and $LiPO_2F_2$.[18,22,36,52,53]

PF_5, acting as a Lewis acid, can facilitate the acid catalyzed ring opening of EC.[10,17,40] The reactivity of PF_5 with EC has been shown to be larger than with the linear carbonates.[50] The opened ring of EC can then undergo multiple reactions. The first is polymerization with additional EC molecules to form poly(ethylene oxide)-like (PEO) polymers and CO_2.[50] As CO_2 is a product of the polymerization reaction, as it forms, the reaction rate decreases.[50] Any added CO_2 will also slow the reaction while any reactions that consume CO_2 will allow polymerization to proceed. This may be another Li-ion cell mechanism which benefits from excess CO_2 as it may help to slow EC polymerization. Otherwise the formed polymer layers would increase impedance and cause power fade.[50]

Once the EC ring has been opened, it can also react with a linear carbonate to form the alkyl dicarbonates DMOHC, DEOHC and EMOHC.[50] To determine the reactivity between PF_5 and some electrolytes, Sloop et al. exposed pure EC:DMC (not exposed to charged electrodes) to freshly formed PF_5 gas and found that DMOHC was formed.[17] When EC:EMC was exposed to PF_5, transesterification products DMC and DEC as well as dimerization products DMOCH, DEOHC, and EMOHC were formed.[50]

Sasaki et al. also studied DEOHC formation in the presence of Li-alkoxides both with $LiPF_6$ and without $LiPF_6$.[40] The results showed that DEOHC production was accelerated in the presence of $LiPF_6$. The authors suggested that PF_5 (as a Lewis acid) plays a catalytic role in DEOHC production rather than as an active species by enhancing the positive charge densities on the carbon atoms of carbonate groups. Therefore, accelerating the rate of the nucleophilic attack of the alkoxides anion.[40] Additional reaction products of PF_5 and linear carbonates include RF, ROR, alkenes and CO_2.[10]

Salt loss in solution

Many of the reactions discussed in this chapter also have the capability of removing lithium salt from solution via precipitation reactions. While some capacity loss in Li-ion cells has been attributed to damage to electrodes which causes lithium to be unavailable for intercalation or deintercalation processes,[10] studies of electrolytes from older cells have shown a decrease in salt concentration.[54] To maintain the charge balance in the electrolyte, any Li^+ removed from solution must coincide with the removal of an anion from solution or the generation of a proton. This is potentially from reactions in this chapter that produce insoluble Li-containing compounds such as LiF (insoluble) and $LiPO_2F_2$ (~ 1% soluble).[55,56]

Cross-talk – exchange of species between electrodes

Recent studies[52,57,58] have considered the individual reactions that occur when the electrolyte is exposed to only a lithiated negative electrode, a delithiated positive electrode

or a full cell. These studies have identified potential negative/positive interactions that are pivotal to cell performance. In general, it was found that in systems with a missing electrode, parasitic reactions and impedance are accelerated.

In 2016, Xiong et al. used pouch bags to separate lithiated graphite negative electrodes and delithiated positive electrodes to isolate reactions between charged electrodes and the electrolyte.[57,58] In this summary, the positive (delithiated) and negative electrode (lithiated graphite) will be referred to as positive and negative electrodes even when separated from the full electrode configuration for ease of comparison. The gases formed during storage of these individual electrodes were measured using a GC coupled with a thermal conductivity detector (TCD) and compared with gases from standard pouch cells under the same storage conditions. Findings included limited gas production in pouch bags containing only the lithiated graphite and in the full pouch cell while the pouch bag containing only the delithiated positive electrode had the largest volumes of gas formed.[58]

Most of the gas produced in the pouch bag containing the positive electrode was CO_2 while the gas produced in the the full pouch cells contained significantly less CO_2 (over half the CO_2 produced by full cells). This indicates that the presence of the anode consumes the CO_2 produced by the positive electrode. Most of the gas produced in full pouch cells was H_2. Some CO was produced in positive pouch bags and full pouch cells, but no observable difference or trend was determined. Little to no methane production occurred in positive pouch bags.[58]

Positive electrode pouch bags containing the additive PES where the electrode had been charged to 4.4 V had over four-times the gas production than pouch bags where the positive

electrode had been charged to 4.2 V in the 500-hour observation period, indicating that gas generation is dependent on upper cutoff potential.[58]

The total charge transfer resistance (measured by impedance) for the 4.4 V positive electrodes in pouch bags increased over ten times larger than positive electrodes from the full pouch cell. The authors suggest that oxidized products formed at remain at positive electrode in pouch bags and increase impedance, while these oxidized products are removed by the negative electrode in full cells.[58]

In one study, Kim et al. monitored the impedance, decomposition of $LiPF_6$ and production of alkyl dicarbonates of electrodes stored in 1.0 M $LiPF_6$ in EC:DEC (1:2) for two weeks.[52] The findings included slightly increased impedance in positive electrodes, suggesting that the presence of the negative electrode prevents major resistive products from accumulating onto the positive electrode.[52,58] The extent of $LiPF_6$ decomposition was found to be larger in electrolytes containing only the delithiated positive electrode. The authors attributed this to species created by the negative electrode creating a more basic environment which would suppress any PF_5 Lewis acid formed from PF_6^- decomposition.[36,52,53]

For these storage experiments it was found that the negative electrode was the main source for EMOHC and DEOHC formation as electrolytes with only the negative electrode present produced these species while systems with only the positive electrode produced very little.[52] The full pouch cell produced EMOHC concentrations similar (within 2%) to the concentrations produced by positive electrode-free systems. The DEOHC concentrations measured in the positive electrode-free systems were much higher (over 150% for NMC cells and over 500% for LCO cells) than those measured in the full cells indicating the presence of the positive electrode must minimize the DEOHC formation in

full cell systems.[52] Interestingly, DMOHC was only formed in the full cells. While a small amount was measured in the electrolyte containing only the positive electrode, no DMOHC was measured in the stored electrolyte containing the negative electrode, suggesting that DMOHC generation requires the presence of both electrodes.[52]

CO_2 has also been shown to have reactivity at the positive and negative electrodes. Ikeda et al. showed how CO_2 could reduce at the anode via electron transport through the SEI to form oxalate, formate, carbonate and CO.[59,60] Oxalate and formate can travel to cathode to be re-oxidized and generate CO_2. Sloop et al. also found that a cell (containing 1.0 M $LiPF_6$ in EC:(EMC/DMC)) saturated with CO_2 slowed the polymerization of EC but that the anode could reduce CO_2 to oxalate, carbonate (CO_3^-) and CO. The carbonate remained at the negative electrode while the oxalate could be oxidized at the positive electrode to reform CO_2.[50] This would result in a reversible self-discharge as there is no permanent loss of charge while the formation of CO and carbonate are irreversible (causes permanent capacity loss) and also increases the amount of products building up on the SEI.[50]

The self-discharge effect of CO_2 and the oxalate reduction product was investigated by Ellis et al. in 2017. The study compared the self-discharge rates of cells with and without CO_2. No significant difference was observable, suggesting CO_2/oxalate shuttle does not occur.[61]

Other negative/positive electrode interactions are hypothesized to occur in Li-ion cells[32,52,62,63] such as the production of acidic species at the positive which migrate to the negative and decompose the SEI resulting in irreversible capacity loss.[52,63] In contrast, some studies have shown a product from the positive electrode can form a passivating film

on the negative,[62] while others have seen oxidation products from the positive can migrate to the negative to form a solid.[32]

Electrode and SEI dissolution

Previous studies have reported the propensity of Mn to dissolve from the positive electrode. While there has been some study of transition metal dissolution for positive electrodes containing Ni and Co, their dissolution is reported to be less severe than Mn dissolution.[10] Gu et al. found that Mn dissolution was especially prevalent when the positive electrode underwent conversion from layered to spinel. [64,65] Additionally, it has been found that cells cycled to higher positive electrode potentials, at higher temperatures, in more acidic electrolyte environments and that had higher positive electrode surface areas showed increased transition metal dissolution.[10,66,67] The dissolution of Mn and then transport through the electrolyte is hypothesized to be facilitated by an acetylacetonate or an oxalate anion,[67] however it is difficult to characterize this species due to its low concentration.[68]

The deposition of Mn at the negative electrode causes an increase in negative electrode impedance,[67] however, the method to which Mn is incorporated into the SEI layer is still debated. It was thought that Mn would reduce at the negative electrode, however this process could be kinetically hindered by the thickness of the SEI and the transport of Mn^{2+} through the SEI.[68] Instead, some have suggested that a small amount of Mn^{2+} reduces to Mn^0 while the remainder exists as Mn^{2+} in theSEI.[66,67] Manganese(II) could exist in the SEI via substitution of Li^+ from compounds, such as LiF and Li_2CO_3, from which Li^+ is immobile, forming MnF_2 and $MnCO_3$, these are likely less readily formed than the substitution of Li^+ from compounds such as lithium alkyl carbonate.[68] Conflicting data on

the presence of Mn^0, MnF_2 and $MnCO_3$ in the SEI indicate that more characterization of the negative electrode is necessary.[66-68]

Upon exposure to high temperature, Richard et al have shown that for a cell containing a carbon electrode and 1.0 M $LiPF_6$ in EC:DEC (3:7), the SEI of the carbon negative electrode decomposes from LEDC into Li_2CO_3 over time.[10,55] This reaction may be kinetically hindered but may take place slowly as Li-ion cells age as it has been found that lithium alkyl carbonates convert into Li_2CO_3 over long periods of time.[10,55] Richard et al. also found a large amount of LiF in the SEI layer.

Genieser et al found that at elevated temperatures (above 80°C) the morphology and chemical composition of the negative electrode SEI changes throughout cycling.[34,56] In another experiment at high temperature (70°C), Andersson et al. concluded that damage occurred to the graphite negative electrodes' SEIs during extended storage from evidence that the electrolyte (1.0 M $LiPF_6$ in EC:DMC (2:1 v/v)) reduction peak reappeared during the first cycle after storage.[69] In the same study, the LiF content of the SEI at the negative electrode was found to increase at elevated temperatures. The authors attribute the Li^+ to originate from the electrolyte salt. Others have shown that the positive electrode also experiences decomposition and rebuilding of surface layers at elevated temperatures which can cause capacity fade and loss of power.[70,71]

Findings from the studies discussed in this section where electrodes are separated from each other are valuable in determining the dialog that occurs during full cell charge and discharge. The consumption of CO_2 gas by the negative electrode is potentially a cause of Li^+ loss from electrodes and SEI growth. $LiPF_6$ decomposition was shown to occur primarily at the positive electrode and the formation of dimerization products was shown

to occur at the negative electrode. These findings help contextualize the results from Chapter 4 and Chapter 5.

Summary

The discussion of electrolyte reactions in this chapter is included to provide context for the work presented in this thesis. Important considerations include the mechanisms of transesterification and dimerization involving Li-alkoxide formation and ring opening of EC respectively, the "cross-talk" between electrodes, and the potential reformation of SEI layers over time.

3. CHAPTER 3 – EXPERIMENTAL METHODS

Li-ion cells can have many geometric configurations such as wound, cylindrical or stacked. Wound pouch cells provided without electrolyte that were mass produced by a major manufacturer were used in this work. These machine-made cells are very uniform and can be filled easily with various electrolyte compositions, therefore isolating the effects of electrolyte and additives. Li-ion cells are described by their size. For example, the cells studied in this thesis are referred to as 402035-size cells as they are 40 mm long, 20 mm wide and 3.5 mm thick.[6]

Cell specifications

Cells studied in Chapters 4 and Chapter 5 consisted of sealed, dried (no electrolyte), machine-produced 402035-size (240 mAh) pouch cells that were purchased from LiFun Technologies (Xinma Industry Zone, Golden Dragon Road, Tianyuan District, Zhuzhou City, Hunan Provence, PRC, 412000). The positive electrodes in cells studied in Chapter 4 and Chapter 5 used single crystal NMC532 positive electrode material[72] with 94% NMC532, 4% conducting diluents (2% Super S carbon black and 2% KS-6 graphite, both from Imerys) and 2% polyvinylidine fluoride (PVDF) binder (source unknown, supplied by LiFUN). The negative electrode consisted of 96% artificial graphite (15-30 μm particle size, grage AML-400 from Kaijin (China)), 2% carbon black (Super S Carbon Black) and 2% sodium carboxymethylcellulose (NaCMC)/styrene butadiene rubber (SBR) binder

(source unknown, supplied by LiFUN). The positive electrode loading was 21.3 mg cm^{-2} and the density after compression was 3.5 g cm^{-3}. The negative electrode loading was selected so that the cells could be charged to 4.5 V without lithium plating. The negative electrode coating density was 1.55 g cm^{-3} after compression.

Cell filling

Once in the Ar-filled glovebox, cells were filled with ~1.0 g of prepared electrolyte and vacuum sealed at 170°C under -90 kPa gauge pressure with a vacuum heat sealer (Model MSK-115A from MTI Corporation). Cells were weighed before and after sealing to ensure no significant solvent loss.

Electrolytes

All electrolytes were prepared with 1.1 m $LiPF_6$ salt (BASF, 99.94%, water content < 14 ppm). The solvent studied in Chapter 4 was 3:7 weight ratio (3:7) ethylene carbonate (EC) : ethyl methyl carbonate (EMC) (BASF, USA, EC purity: 99.95%, EMC purity: 99.99%, water content < 10 ppm) with additives: 2% weight fluoroethylene carbonate (FEC) (BASF, 99.94%, water content < 100 ppm) and 1% 1,3,2-dioxathiolane-2,2-dioxide (DTD) (Suzhou Yacoo Chemical Reagent Co., >98%). The solvents used in Chapter 5 were either 3:7 weight ratio (3:7) ethylene carbonate (EC) : dimethyl carbonate (DMC) (BASF, USA, EC purity: 99.95%, DMC purity: 99.95%, water content < 20 ppm) or 80% EC:DMC (3:7) and 20% methyl acetate (MA) (BASF, USA, purity: 99.99%). Both electrolyte mixtures used 2% weight FEC and 1% DTD as additives.

Cell formation

Sealed cells were first held at 1.5 V for 24 hours to help ensure full wetting of the electrodes and then transferred to a 40.0 ± 0.1 °C temperature-controlled box to undergo formation on a Maccor 4000 series charger at C/20 (11 mA) to 3.5 V, held at 3.5 V for 1 hour and removed to degas SEI formation products in the same glove box and with the same sealing conditions as above. Degassed cells then continued first formation on the Maccor to their designated upper cutoff potential then discharged to 3.8 V. A schematic of a cell formation protocol is shown in Figure 3.1.

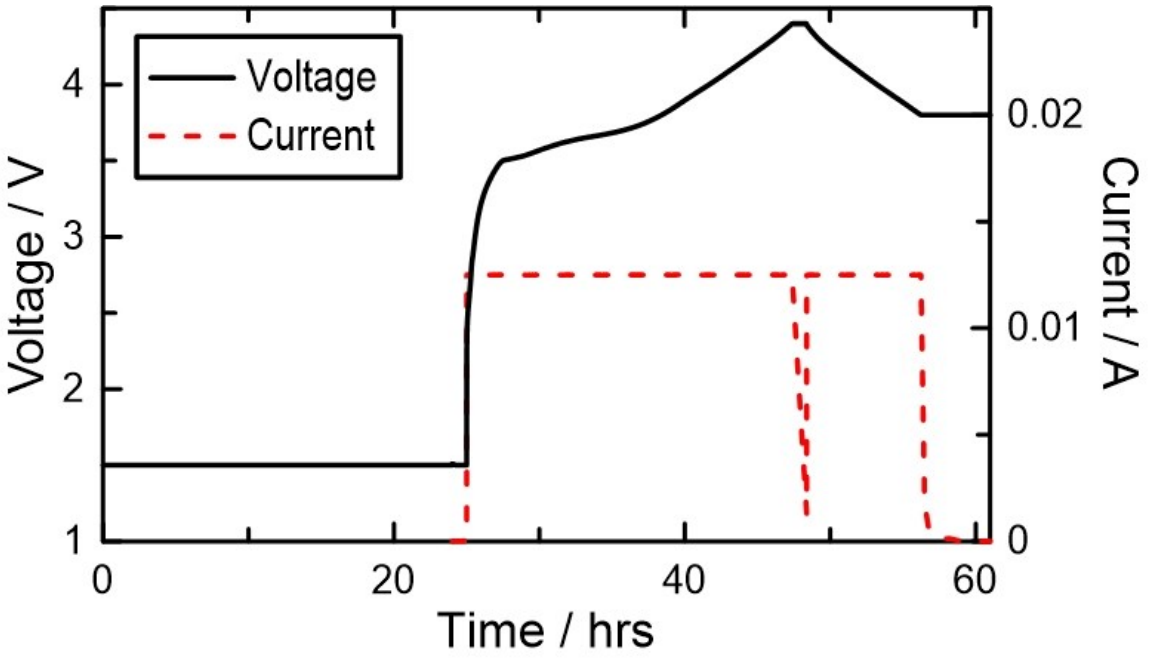

Figure 3.1 - Typical cell formation protocol voltage (black) and charge current (red)

As discussed in Chapter 1, the first charge cycle is important for SEI formation. Figure 3.2 shows the differential capacity (dQ/dV) vs. voltage (V) measured for a part of the first formation charge and discharge. An increase in differential capacity originates from

the electrolyte gaining an electron and Li^+ ion at the negative electrode to form the SEI. The peak in dQ/dV will occur at the reduction potential of the specific species.[28] For example, it has been shown by Burns et al. that the common electrolyte component, EC, will reduce at the negative electrode at ~2.9 V during the first charge of a full cell (~0.4 V vs. Li/Li^+).[73] Figure 3.2 shows the peak in differential capacity for EC reduction (red) at this voltage. The reduction produces a passivating film on the negative electrode, ideally preventing any further reduction of electrolyte in subsequent cycles.

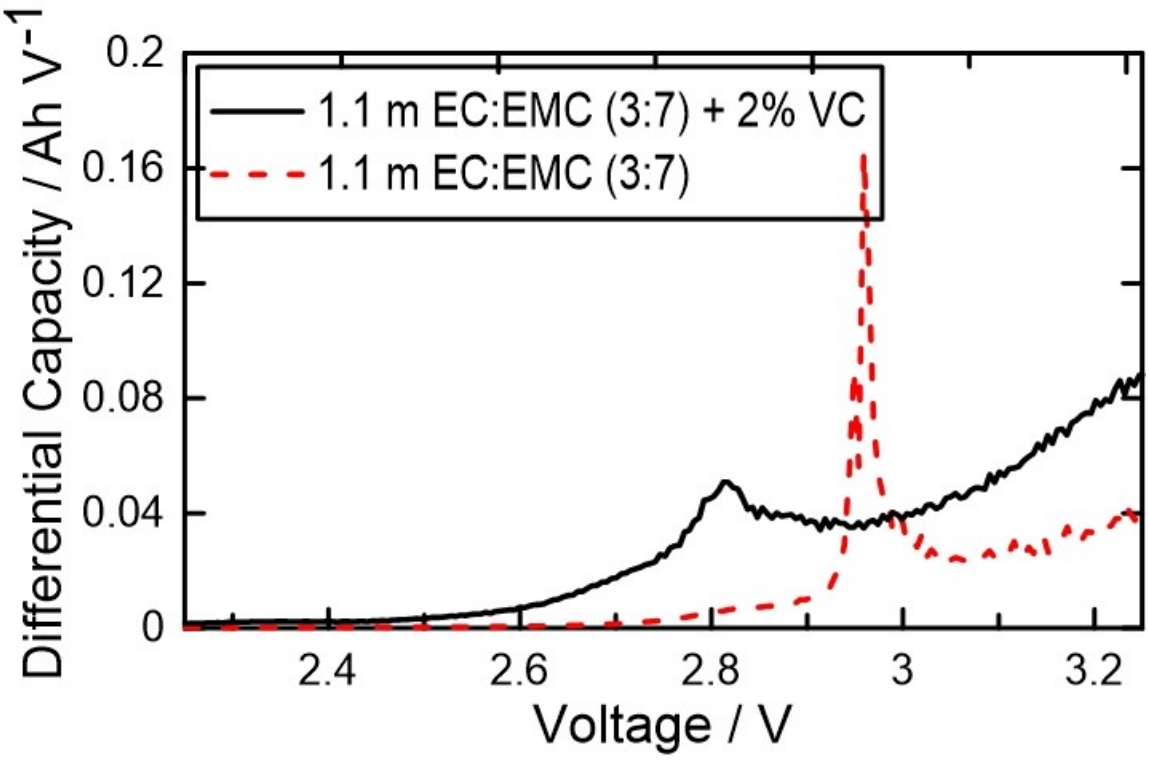

Figure 3.2 - The differential capacity is shown as voltage increases for two cells. The cell with no additives (red) shows an EC reduction peak around 3.0 V. The cell with 2% VC (black) reduces at a lower voltage of about 2.8 V.

Use of additives can change the composition of the SEI so it is more passivating.[28,73] Additives such as VC and FEC will preferentially reduce at higher potentials (vs. Li/Li^+)

on the negative electrode than EC or linear carbonate and create effective, long lasting protection from further electrolyte reduction. The amount of additive used is carefully chosen to keep the impedance low. Figure 3.2 also shows the differential capacity measured in a full cell during the first charge for an electrolyte containing an additive. The preferential reduction can be seen in Figure 3.2, as the electrolyte containing 2% VC (in black) will reduce at an earlier full cell potential. There is also no EC reduction peak observed in this cell, indicating the initial amount of VC was successful in passivating the negative electrode.

Cell cycling

Cycling equipment is essential for studying cell performance. A typical charger system can apply a potential or current and monitor the cell current or potential, respectively, throughout many charge and discharge cycles to mimic charging and discharging conditions in everyday use. These are connected to cells via two wires to apply the potential (or current, depending on the protocol) and two wires to measure the current (or potential). From these systems, it is possible to record the voltage, current, charge capacity, discharge capacity and time for a given cell.

Cells used in Chapter 4 were placed in a 55.0 ± 0.1 °C temperature-controlled box for the duration of testing and cycled using a Newware (Shenzhen, China) charging system at C/3 (80 mA) rate between 2.8 V and the designated upper cutoff voltage. Constant current – constant voltage (CCCV) mode was used to charge cells until the current was less than

C/20 (11 mA). After every 50 cycles, a C/10 (22 mA) charge and discharge cycle was performed. Figure 3.3 shows an example charge and discharge protocol.

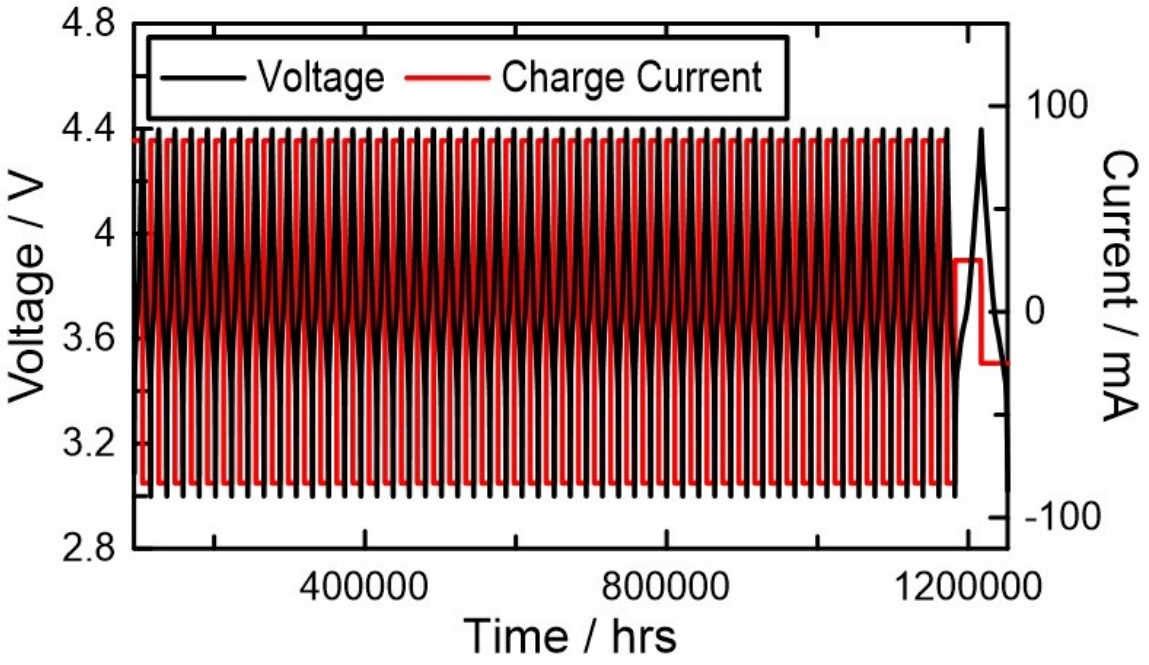

Figure 3.3 – Charging protocol showing voltage (black) and current (red) vs. time. The protocol consists of 50 charge and discharge cycles at C/3 (80 mA) followed by one charge and discharge cycle at C/10 (22 mA). This sequence is repeated until end of testing.

Cells studied in Chapter 5 were placed in a 55.0 ± 0.1 °C temperature-controlled box for the duration of testing and cycling using a Moli charging system (Canada). The cells were charged and discharged at C/3 (80 mA) between 2.9 V and the designated upper cutoff voltage. After 50 cycles, a C/20 (11 mA) charge and discharge cycle was performed to check absolute capacity loss and impedance growth. Figure 3.3 shows a similar charge and discharge protocol

Many cell diagnostics can be extracted from cells' charge and discharge data. The charge (Q_c) and discharge (Q_d) capacities can be recorded vs. charge-discharge cycle number. The potential throughout charge and discharge cycling is also recorded. The average charge potential and average discharge potential can be used to calculate ΔV, the difference between these two potentials. As cells age, ΔV can increase due to impedance growth in the cell. This is shown in Figure 3.4, where the charge and discharge voltages are plotted vs. capacity for a fresh cell and an aged cell (with 700 cycles). The aged cell, with a ΔV of 0.082 V compared to the original ΔV of 0.057 V, exhibits increased polarization and therefore increased overall impedance. The overall resistance in a cell can include the resistance from multiple components such as electrical connections, electrolyte, electrodes and the SEI layers on both electrodes. The polarization can be used to estimate SEI resistance growth as the resistance due to electrical connections, electrodes and electrolyte is expected to remain relatively constant.[74]

Gas measurements

The volume of gas produced during formation and during cycling was measured using Archimedes' principle.[75] Cells were hung below an analytical balance (Shimadzu, AUW00D) and suspended in room temperature de-ionized water (18.2 MΩ-cm, Thermo Scientific Barnstead Nanopure Water Purification System) and weighed. Because the mass of the sealed cells remains constant, the difference in weight of the submerged cells before and after testing is proportional to the amount of gas produced.

Treatment of error

Errors throughout this work were determined by calculating the standard deviation (*s*) between the individual instrument readings, *x*, the average instrument reading, $\bar{x}$, and the sample size, n, according to the Equation 3.1.[76]

$$s = \sqrt{\frac{(x_1 - \bar{x})^2 + (x_2 - \bar{x})^2 + \ldots (x_n - \bar{x})^2}{\mathrm{n} - 1}} \tag{3.1}$$

The standard deviation was then used to determine the confidence interval to determine the statistical significance of the data to each other and/or to the expected concentrations/initial values. This was done according to Equation 3.2, where *y* is the confidence interval and z_t is the Student's T value based on the 95% confidence level.[76]

$$y = z_t \frac{s}{\sqrt{\mathrm{n}}} \tag{3.2}$$

The Student's T values at 95% confidence for n=2, 3 and 4 are 12.706, 4.303 and 3.182, respectively. The errors calculated in this chapter are based on multiple cells/electrolyte samples made to validate these methods. The sample size is indicated for each test. In Chapter 4 and Chapter 5, either one or two cells were available that experienced the same cycling and electrolyte conditions, therefore, the errors calculated represent standard deviation in the instrument and calibration.

Previous extraction method

An existing method for liquid-liquid electrolyte extraction is shown schematically in Figure 3.5a. The method includes removing a discharged (2.0 V) jelly roll from the pouch and adding it to a polytetrafluoroethylene (PTFE) vial containing dichloromethane

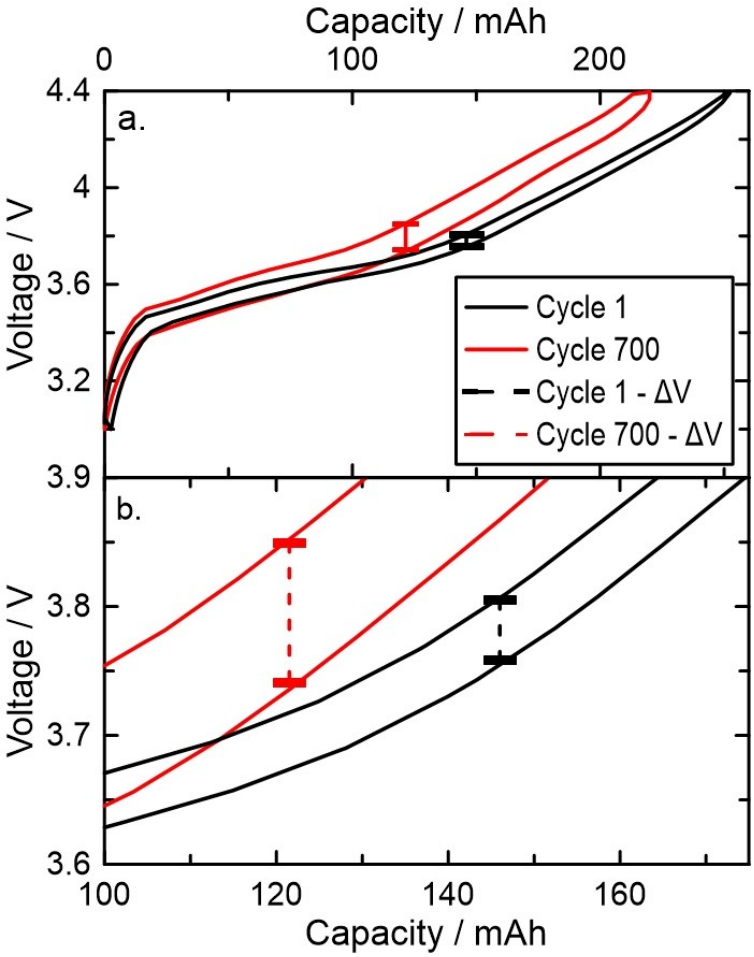

Figure 3.4 – a) Voltage plotted vs. capacity of cell for charge and discharge cycle 1 (black) and charge and discharge cycle 700 (red). The difference in average voltage, used for ΔV calculation, is shown by the dotted line. b) zoomed-in view of (a.), emphasizing the change in average charge and discharge voltage which occurred during cycling.

(CH_2Cl_2) solvent (Optima, Fisher Chemical, US, >99.9 %) for electrolyte extraction. The PTFE vial was then machine-shaken in two directions for a total of 30 minutes. Some of the extract is removed and filtered with a syringe filter containing a PTFE membrane with a 0.45 μm pore size into a second PTFE vial containing additional CH_2Cl_2 and deionized-water for $LiPF_6$ and HF extraction.[30] The new solution was then shaken for another 5 minutes, centrifuged for 20 minutes at 2200 RPM (centripetal acceleration = 800g) to separate the organic and inorganic layers, then the bottom, organic layer was removed for gas chromatography-mass spectrometry (GC-MS) analysis. This method extracts most the electrolyte in a wound cell but exposes the SEI to potentially damaging solvents, rendering the remainder of the cell unavailable for additional study.

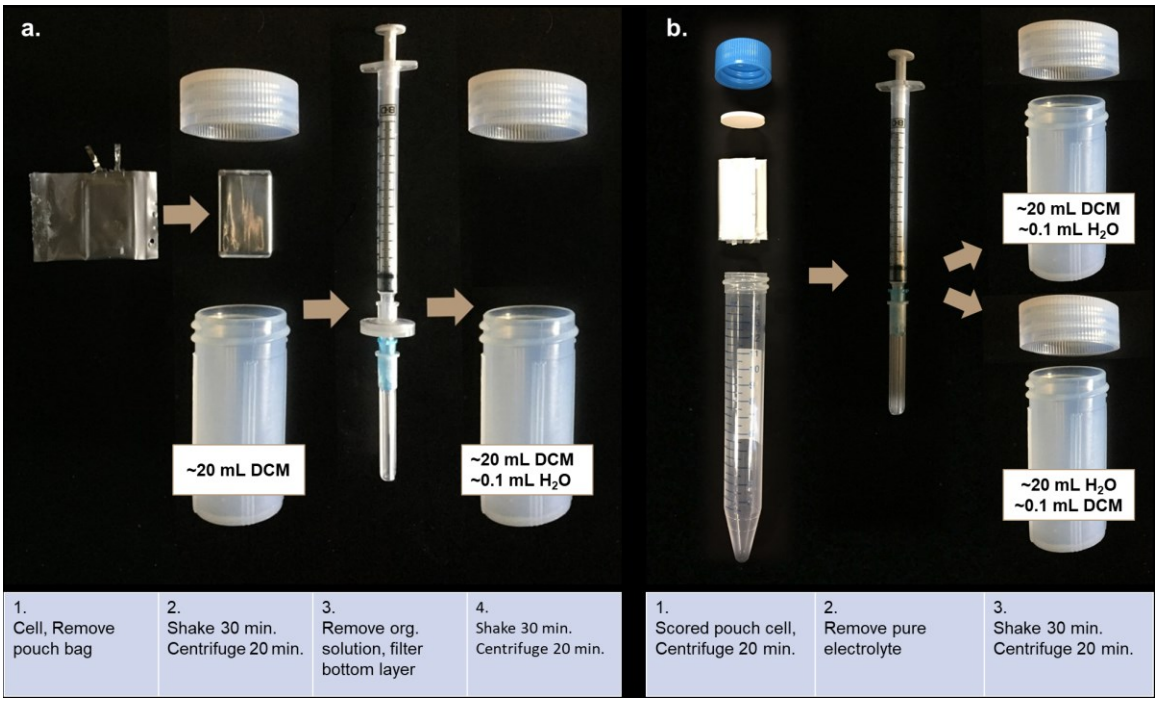

Figure 3.5 - a) Schematic of the previous liquid-liquid extraction method.[30] b) Schematic of the modified extraction method which uses a centrifuge to extract electrolyte from cells.

Modified extraction method using a centrifuge

Figure 3.5b shows a schematic of the centrifuge method. For this method, the pouch bag of discharged cell (2.0 V) was cleaned of any markings and scored on either end of the jelly roll. Previous centrifuge techniques have removed the separator to extract electrolyte,[77] however here, the entire cell was placed in a 15 mL polypropylene (PP) vial. The cap was fitted with a 9 mm PTFE/silicon seal to prevent solvent evaporation. The tube was then centrifuged at 2200 RPM (800g acceleration) at 30°C for 20 minutes. The sealed vials were weighed before and after centrifuging to ensure no significant solvent loss. Of the original 0.9 to 1.0 g of electrolyte added during cell filling, approximately 0.1 g to 0.2 g of electrolyte was recovered from this process. The pure electrolyte was then removed from the PP vial with a 1 mL syringe and diluted for GC-MS and inductively coupled plasma-mass spectrometry (ICP-MS) analyses. Electrodes were unwound from the jelly roll and allowed to dry in a fume hood overnight. This process will evaporate volatile components of the residual electrolyte such as EMC and DMC. Ethylene carbonate, $LiPF_6$ and other non-volatile components (manganese compunds) will remain in the pores of the electrode. A representative segment of the anode was then used for μ-XRF analysis.

The liquid-liquid extraction and centrifuge methods are compared in Figure 3.6. Here, cells (n=2) with three different electrolyte systems were processed with both methods. Figure 3.6a shows 2% VC and 98% EMC, Figure 3.6b shows 20% EC, 50% EMC and 30 % DEC, and Figure 3.6c shows 30% EC and 70% EMC. Results, reported in panels a, b and c, show no significant difference between samples prepared through liquid-liquid extraction or centrifuge extraction at 95% confidence intervals.

Is the electrolyte centrifuged from a cell representative of the electrolyte within the core of the jelly roll?

A possible concern is that the electrolyte centrifuged from a cell may be dominated by electrolyte from the periphery of the jelly roll and not from the core of the jelly roll. This is because there is normally a small excess of electrolyte added to cells. Experiments were

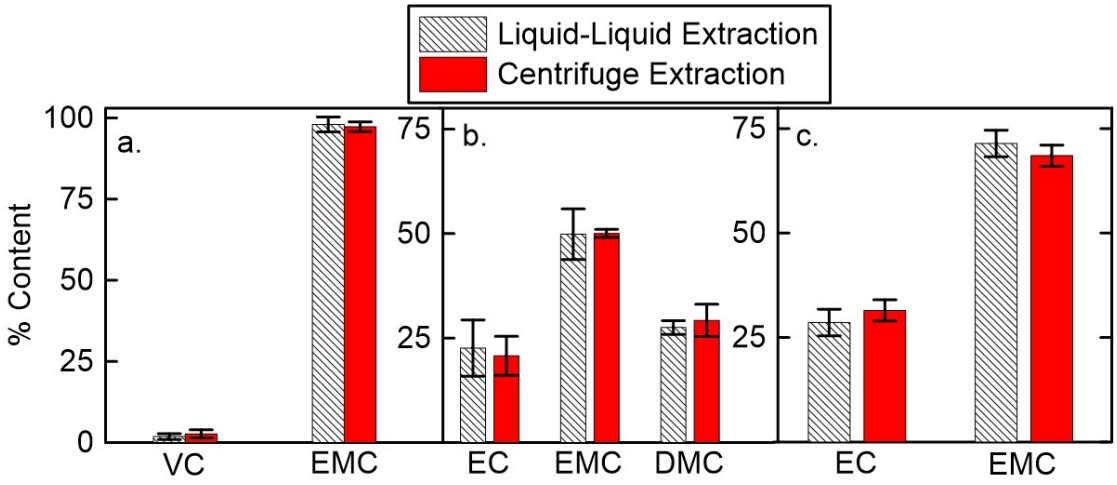

Figure 3.6 - Comparing known electrolyte mixtures measured using liquid-liquid extraction and centrifuge extraction methods a) 2% VC and 98% EMC. B) 20% EC, 50% EMC and 30% DMC. c) 30% EC and 70 % EMC.

designed to probe the time needed for the electrolyte to be homogeneous between the periphery and core of a jelly roll within a pouch cell.

First, fresh, dry cells were filled with 0.8 mL of 1.1 m $LiPF_6$ in EC:DEC (3:7), sealed and wet for 24 hours at 1.5 V to allow for electrolyte permeation into electrode (Figure 3.7a). The cells were cut just below the heat seal in an Ar-filled glovebox and filled with an additional 0.7 mL of DMC (Figure 3.7b). The cells were then sealed again and later opened

for GC-MS and ICP-MS analysis at various times (n=2) after the second filling (1 hour, 1 day, 8 days and 21 days). The organic mass ratios and Li concentration were compared to the expected homogeneous compositions to determine the time required for jelly roll electrolyte system to become homogenous (Figure 3.7c and Figure 3.7d). Results (Figure 3.8) showed that the expected homogeneous EC and DEC content were 90 ± 10 % recovered after 1 day (Figure 3.8a and Figure 3.8b, respectively) and DMC was 107 ± 7 % recovered after 1 day (Figure 3.8c). The data shows no statistically significant difference between mass ratios of organic species measured after one day and the expected mass ratios. After 8 days, the mass ratios matched the expected ratios for a homogeneous electrolyte suggesting full mixing after 8 days.

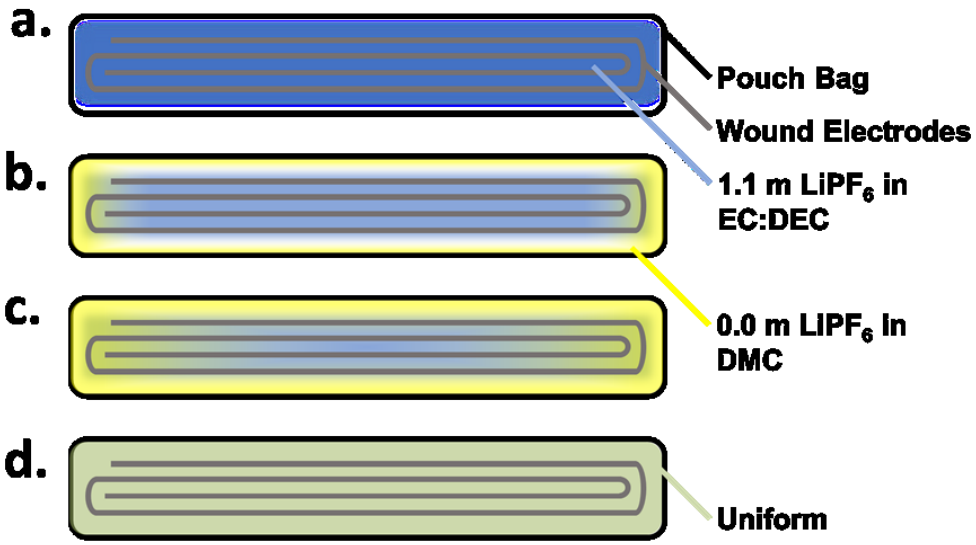

Figure 3.7 - Schematic view of the pouch cell during the electrolyte mixing study. a) pouch bag wet with 1.1 m $LiPF_6$ in EC:DEC (3:7 weight %). b) DMC added to the pouch cell. c) solutions begin mixing. d) time later when electrolyte achieves uniform composition.

ICP-MS analysis for Li measurement showed that after 8 days 90 ± 10 % of the expected lithium was recovered (Figure 3.8d). The data shows no statistically significant difference

between measured and expected lithium concentration at 95% confidence intervals after 8 days. After 21 days the expected and measured lithium contents agreed exactly. Thus, whatever electrolyte extracted using a centrifuge from a cell tested for 21 days or more will be representative of the liquid electrolyte in the core of the jelly roll.

The charge-discharge cycle test times of the cells considered in Chapter 4 and Chapter 5 (about 200 days) were much longer than the time needed for the electrolyte to homogenized between core and periphery. Thus, the electrolyte centrifuge method extracts representative of that in the core of the jelly roll.

GCMS sample preparation

One drop of a pure electrolyte sample was diluted into clean PTFE vials containing ~20 mL of a CH_2Cl_2 organic phase and ~0.1 mL de-ionized aqueous phase to ensure complete extraction of salts. The samples were then shaken for a total of 30 minutes in two directions and centrifuged for 20 minutes at 15 ± 1 °C and 2200 RPM (800g acceleration) to ensure adequate extraction and separation of phases, respectively. The bottom, organic layer was then sampled using a transfer pipette for analysis. The aqueous layer was small enough that it does not cover the entire surface and the pipette is inserted to avoid the aqueous layer. To be sure that only the organic layer was used, only the bottom portion of pipetted liquid was delivered to sample vial.

For cells containing MA (discussed in Chapter 5), it was necessary to develop a new detection method for the GC-MS. Using the existing GC column, it was not possible to detect MA amongst the large CH_2Cl_2 solvent peak as they had similar retention times.

Instead, a second solvent, toluene (ACS Grade, Fisher Chemical, US, >99.5%), was chosen for its miscibility with electrolyte components, immiscibility with water and expected higher retention time than MA. The extraction procedure was like the CH_2Cl_2 extraction:

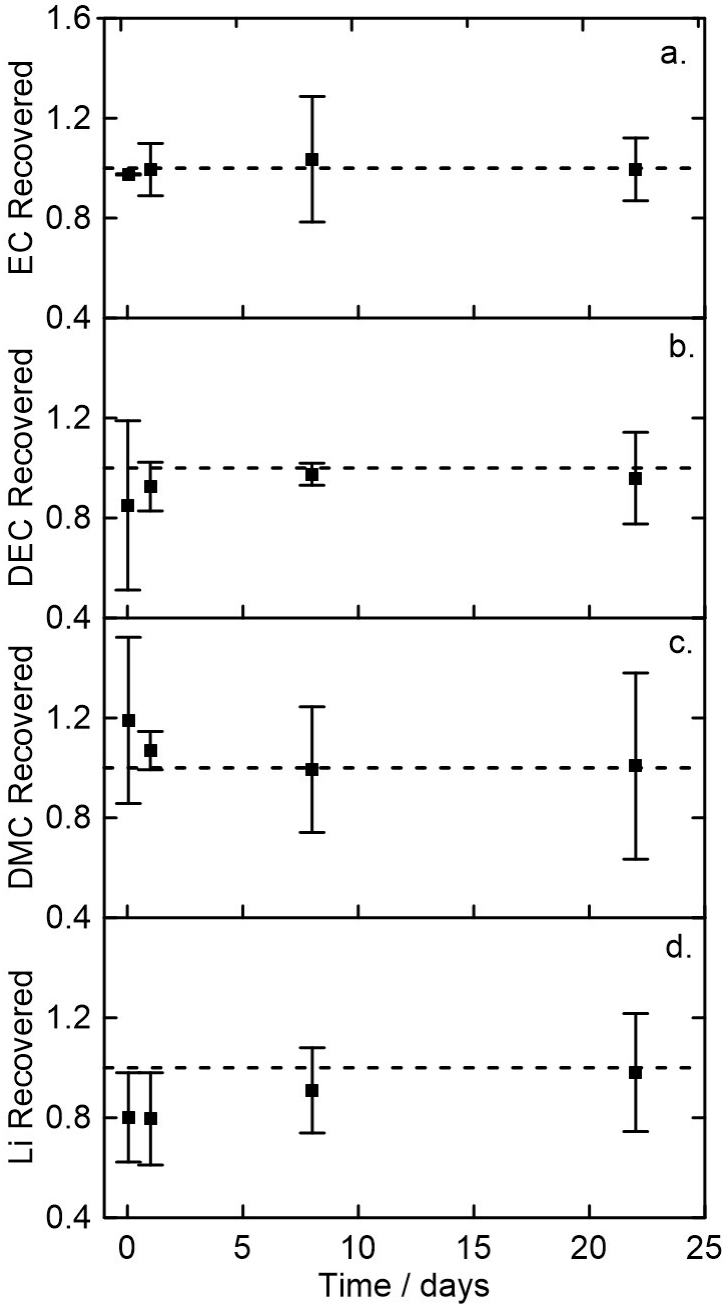

Figure 3.8 - GC-MS and ICP-MS results for the electrolyte mixing study. a) mass fraction of EC recovered compared to that expected based on homogeneous mixing (dashed line). b) mass fraction of DEC recovered compared to expected (dashed line). c) mass fraction

of DMC recovered compared to expected (dashed line). d) Fraction of Li^+ molal concentration recovered compared to expected concentration (dashed line).

One drop of a pure electrolyte sample was diluted into clean PTFE vials containing ~20 mL of a toluene organic phase and ~0.1 mL de-ionized aqueous phase to ensure complete extraction of salts. The samples were then shaken for a total of 30 minutes in two directions and centrifuged for 20 minutes at 15 ± 1°C and 2200 RPM (800g acceleration) to ensure adequate extraction and separation of phases, respectively. The top, organic layer was then sampled using a transfer pipette for analysis.

Without changing the column, the toluene method can measure MA, EMC and DMC as well as other electrolyte components, however, sections of the toluene solvent peak can overlap with DEC peaks. Because of this, the toluene method is used in parallel with the CH_2Cl_2 extraction method to measure MA as well as the other organic electrolyte components. For relative quantification, the measured concentration of MA is scaled with a common peak (either EMC or DMC) as these are expected to be most miscible with both toluene and CH_2Cl_2. To test the quality of the extraction method, sample measurement and quantification, known, freshly prepared electrolyte was processed. MA was measured within 1 % of the expected concentration.

Gas chromatography

A gas chromatograph is a common instrument used to separate components of a mixture or sample with boiling points below ~300°C (depending on experimental setup and column). Figure 3.9 shows a schematic of the gas chromatography and mass spectrometer system. During gas chromatography, the sample is injected through a septum into the inlet.

Carrier gas (the mobile phase) is continuously flushed through the port to enter the column (containing the stationary phase) with the sample gas.[78]

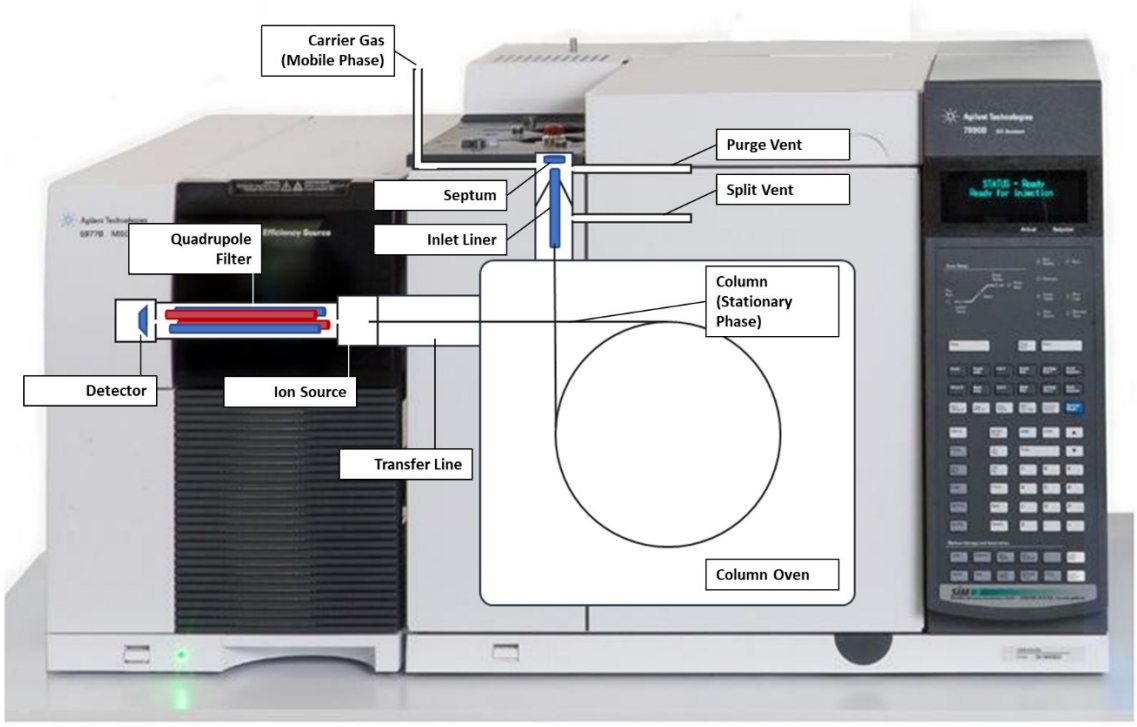

Figure 3.9 - Schematic of a GC-MS

The projected travel time through the column (t_M) and the delay due to stationary phase interactions (t_R') can be combined to estimate the retention time of a compound (t_R) as in Equation 3.3.

$$t_R = t_M + t'_R \tag{3.3}$$

The time required for components to travel through the column depends on the length of the column (L) and the average linear velocity of mobile phase ($\bar{u}$) as described in Equation 3.4.

$$t_M = \frac{L}{\bar{u}} \tag{3.4}$$

The interaction between compounds and stationary phase is determined by the retention factor (k), summarized by Equation 3. where K is the distribution constant of solute between stationary (c_s) and mobile phase (c_m) (Equation 3.) and β is the ratio between the volume of the mobile phase (V_m) and the volume of the stationary phase (V_s) (Equation 3.).[78]

$$k = \frac{K}{\beta} \tag{3.5}$$

$$K = \frac{c_s}{c_m} \tag{3.6}$$

$$\beta = \frac{V_m}{V_s} \tag{3.7}$$

The total retention time can then be summarized by Equation 3..

$$t_R = \frac{L}{\bar{u}}(1 + \frac{K}{\beta}) \tag{3.8}$$

The retention time is therefore proportional to length of column and inversely proportional to average linear velocity. The volume ratio, β, is determined by total column diameter (including the inner coating) and inner diameter (excluding the inner coating) while the distribution constant, K, is determined by the activity of a species with regards to the solid substrate. This can be determined by intermolecular interactions and temperature and will determine the degree of separation.[78,79]

Temperature profiles are often used to improve the separation of compounds with lower boiling points from compounds with higher boiling points. However, for compounds with

similar boiling points, it becomes important to select a column with adequate differences in intermolecular forces between stationary phase and mobile phase.[78,79]

Gas chromatographs, which can achieve sample separation, are often paired with a detector that allows the separated components to be identified and quantified.[78,80] For this study, a mass spectrometer was used in series with the chromatography column.

Mass spectrometry

Figure 3.9 shows a schematic of the mass spectrometer coupled to the chromatography column. As the separated compounds elute the column, they enter the transfer line then the electron ionization chamber. Here, electrons are used to generate ionic species which then enter the quadrupole analyzer to separate the ionic species according to mass to charge ratios (*m*/*z*). The species then reaches the detector for characterization and quantification.[81,82]

In the electron ionization chamber, electrons with 70 eV energy bombard the sample (molecule, M) to generate a radical cation according to Equation 3.. The radical cation contains an unpaired electron and therefore a net 1+ charge.

$$M + e^- \rightarrow M^{\bullet +} + 2\,e^- \qquad (3.9)$$

The electron ionization process can also split molecules to produce fragmented species. For example, molecule AB can ionize to from fragment A^+ as a cation, fragment $B^\bullet$ as a neutral radical species, as in Equation 3..[81]

$$AB + e^- \rightarrow A^+ + B^\bullet + 2\,e^- \qquad (3.10)$$

The species are then passed through the quadrupole analyzer. The quadrupole analyzer consists of four rods: two at a positive potential (red) and two at a negative potential (blue) in opposite corners, shown in Figure 3.9. While the neutral species will not interact with the field generated by the charged rods, any ionic species will interact in the electric field. The voltage applied to the rods consists of direct current and variable frequency or alternating current.

An ion's attraction to the charged rods will depend on the charge of the ion, the mass of the ion and the potential applied to the rods. Considering most species generated by electron ionization typically have a charge of 1+, the attraction and repulsion of the ions with various masses to the rods can be balanced with the alternating current applied. Depending on the voltage applied, a specific mass to charge ratio will pass through the quadrupole and the lower and higher mass to charge ratios will be filtered out of the path.[81,82]

A full mass to charge ratio scan begins with a low direct current and low amplitude alternating current. Both potentials increase throughout the scan, however, the alternating potential increases at a higher rate. By increasing the applied potentials, the mass to charge ratio of ions allowed through the quadrupole will increase.[82]

Finally, the filtered ions will reach the electron multiplying detector which uses the incoming ions to eject electrons. The electrons continue to expel more electrons at subsequent surfaces until the current of incoming electrons on a negative electrode surface are measured and converted to a voltage reading for quantification.

GC-MS sample measurement

An Agilent 7890 Gas Chromatograph coupled to an Agilent 5977B single-quadrupole mass spectrometer was used for organic analysis. The inlet was equipped with a split/spitless injector and a 30 m BR-5MS column with an inner diameter of 0.25 mm and coating thickness of 1 μm. The column was chosen for its relatively non-polar properties. The carrier gas was helium (99.999%) at a constant flow of 1.3 mL/min. Samples were injected into the inlet at 250°C and carried onto the column via carrier gas. To separate species with different boiling points, the oven was first held at 35°C for 8 minutes then increased in temperature at a rate of 40°C/min until the oven temperature reached 290°C. The final oven temperature was held for 5 minutes to ensure all compounds were evolved from column. The transfer line to the MS detector was held at 250°C. The mass spectrometer, containing an electron impact ionization module, had a 200°C ion source and electrons with sufficient energy to induce ionization (70 eV).[30,82] A minimum 5-point calibration curve with an r^2 value of > 0.998 was generated from standards prepared on analysis day with known concentrations. Each sample and standard were injected twice to ensure reproducibility. A full scan of the mass to charge ratio filter was performed on each injection. Data analysis used the appropriate mass to charge ratios to identify and quantify each peak at the appropriate retention time.

Inductively coupled plasma mass spectrometry

Figure 3.10 shows a diagram of an inductively coupled plasma mass spectrometry (ICP-MS) instrument. ICP-MS instruments are excellent for elemental analysis.[83,84] The

principles of ICP-MS are like that of the mass spectrometer described above, however, rather than forming ions through electron ionization, a plasma torch is used.[82]

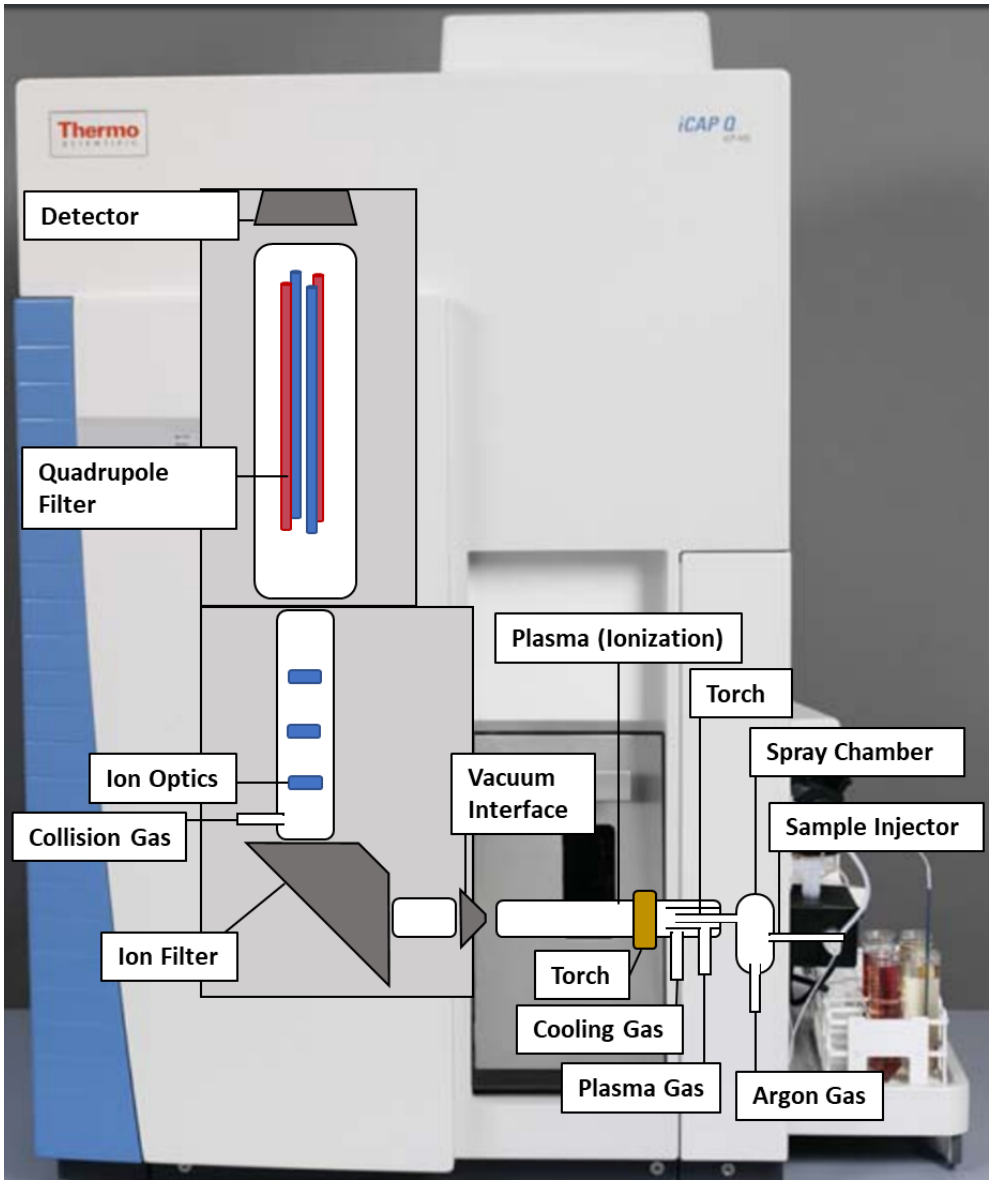

Figure 3.10 - Diagram of an ICP-MS instrument

During sample analysis, a sample is injected into the spray chamber along with argon gas which is used to vaporize the sample. The vapor then travels to the torch where the sample is ignited with plasma gas. The oxidation of the vaporized sample generates positively

charged ions. These ions go on to enter the first vacuum chamber to be separated from the non-ionized species. The principle separation occurs at the ion filter and is followed by additional separation in the ion optics chamber. Here, the aid of a collision gas helps separate ionized species from unwanted polyatomic ions. Ionized samples then can be sent through the quadrupole mass spectrometer, were they are filtered by the same principles describe above. The separation of elements occurs in the quadruple as the potential applied can be tuned for the elemental masses desired. Also like the GC-MS, the ICP-MS uses an electron multiplying detector which multiplies the electrons expelled by the collision at the detector interface to ultimately measure a signal voltage at the terminating anode.[85,86]

ICP-MS sample preparation and measurement

Figure 3.11 shows a schematic of the ICP sample preparation process. About 0.10 g of pure electrolyte was weighed into PTFE vials containing ~20.0 g of aqueous 2% HNO_3 (ACS Grade, Sigma Aldrich, US, 70%) and ~0.2 g of CH_2Cl_2 for organic separation. Vials were shaken for 20 minutes in one direction, 20 minutes in the perpendicular direction and centrifuged at 15 ± 1 °C and 2200 RPM (800g acceleration) for 20 minutes to adequately extract the Li^+ into the aqueous phase and separate the aqueous and organic layers. For the second dilution, approximately 0.11 g of the aqueous top layer was added to ~50.0 g of 2% HNO_3 and shaken for 5 minutes. Target concentrations for the ICP-MS instrument were between 0 and 100 $\mu g L^{-1}$ Li^+. Samples were then sealed in PP vials and stored in a refrigerator at 10 ± 2 °C until analysis.

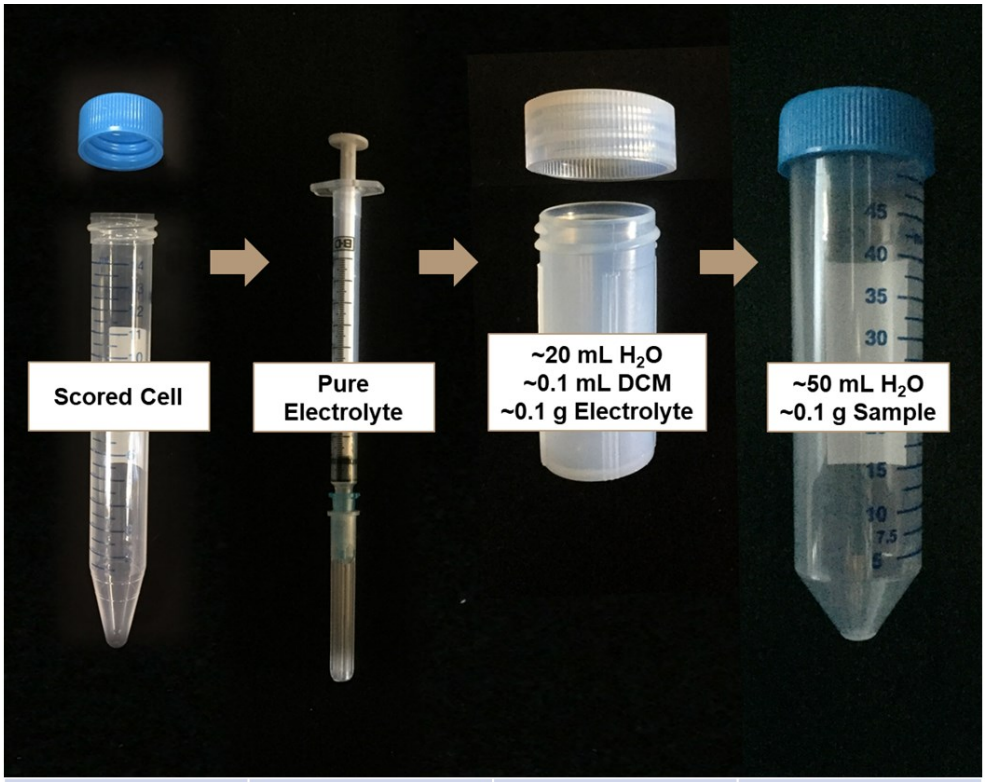

1.	2.	3.	4.
Centrifuge scored cell	Remove pure electrolyte	Shake 30 min. Centrifuge 20 min. Remove aq. layer	Dilute Sample < 100 ppb

Figure 3.11 - A schematic showing ICP sample preparation.

On the day of sample analysis, lithium standards were diluted from 1000 mg L^{-1} stock solution (ICP Standard, Ultra Scientific, US, 1000 ppm in 2% HNO_3) with 2% HNO_3, to produce a six-point calibration curve of 0, 20, 40, 60, 80 and 100 µg L^{-1} of Li^+ with an r^2 value greater than 0.9999. A freshly prepared 1.1 m $LiPF_6$ in EC:EMC (3:7) electrolyte with known concentration also underwent sample processing and ICP-MS analysis to ensure measured concentrations were accurate.

An iCAP Q ICP-MS (Thermo Fisher Scientific, MA, USA) paired with an ESI SC-4DXS autosampler (Elemental Scienctific , NE, USA) was used for sample analysis following the protocol developed by Smith et al.[87] All samples were run in Kinetic Energy Discrimination (KED) mode, using high purity helium (99.999%) as the collision gas. Online internal standard addition was performed to correct for any instrumental drift if necessary using 50 μg L^{-1} scandium and an SC FAST Valve (Elemental Scientific, NE, USA). A quality control check standard was analyzed every 20 samples. Samples were measured with 0.01 s dwell time and 25 sweeps. A minimum of 3 main runs with a maximum relative standard deviation of 5.0% were taken for each sample.

Robustness of ICP measurements

The ICP-MS method was tested periodically with electrolytes of known concentrations to ensure the robustness, reproducibility and stability of the method over time.[88] This test included four ICP-MS samples prepared on day 1 from an electrolyte of known salt and solvent concentration. These samples were then stored in a 10 ± 2 °C refrigerator in PP vials which were wrapped with Parafilm™. On day 6, an additional four samples were prepared from a new electrolyte of known salt and solvent concentration prepared the same day. Both sets of samples were measured by ICP-MS on day 6 and on day 7. The average fraction of Li^+ recovery for both electrolyte samples on both days are shown in Figure 3.12. Within a 95% confidence interval, there is no significant difference between the expected Li^+ concentration and the measured concentration on either day of measurement and after seven days of sample storage. Each of the four samples also have good agreement (within 5%).

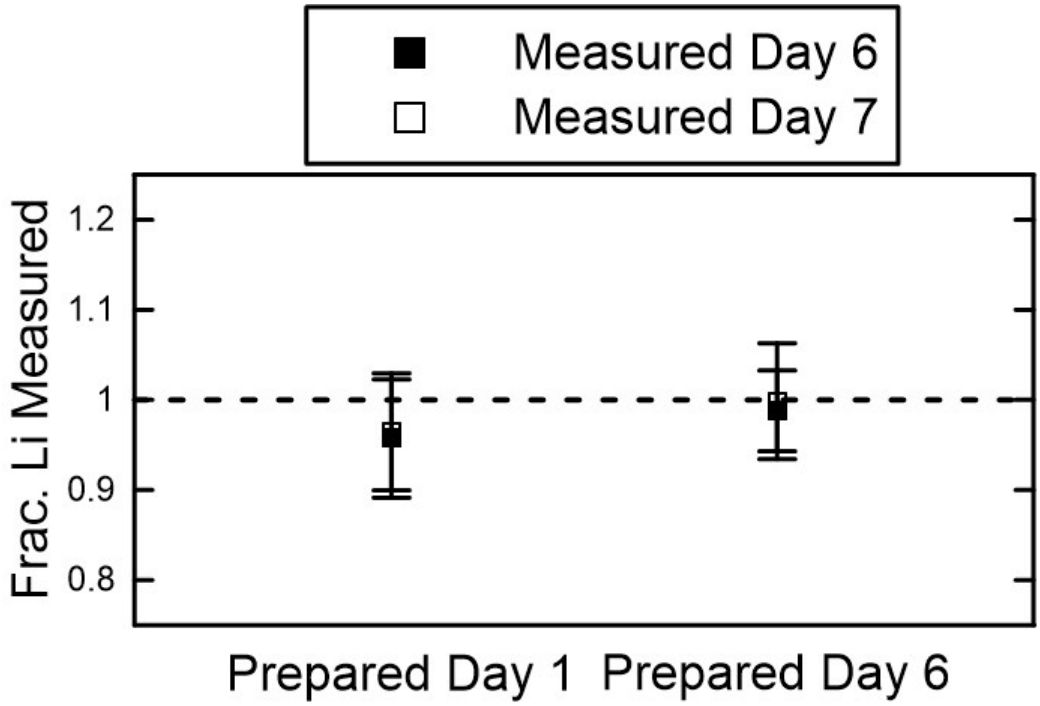

Figure 3.12 – Fraction of Li^+ molal concentration measured compared to expected concentration, measured on day 6 and day 7 of the electrolyte storage experiment

Mn calibration for X-ray fluorescence analysis

A Mn calibration curve was prepared using a Corona Vacuum Coaters (Vancouver, BC, Canada) model V-3T sputtering system. This method, developed by Dahn et al,[89] uses a mask opening over the target and a rotating substrate table to create gradients in the amount of deposited material on a substrate. The linear mask used in this work generates a linear mass per unit area increase vs. position on the substrate (Figure 3.13a). Pre-weighed aluminum foil discs were used to measure the mass per unit area deposited vs. position. (Figure 3.13b). Deposition increased from 0.0 μg cm^{-2} to about 30 μg cm^{-2} across the sputtering track. The scatter in the mass-position curve in Figure 3.13b is due to variations in the average amount of adhesive left on the back side of the foil discs. The average value was subtracted from the mass vs. position calibration.

During the same sputtering run, fresh graphite negative electrodes were mounted on the substrate table next to the aluminum foil weigh discs. The same "wedge" of Mn was deposited onto the graphite negative electrodes. Several of these Mn-coated electrodes were then used to record the Mn count per unit area vs. position on the electrode (Figure 3.13c) to be compared with the mass per unit area vs. position of the weigh discs (Figure 3.13b), thus allowing a calibration curve to be constructed.

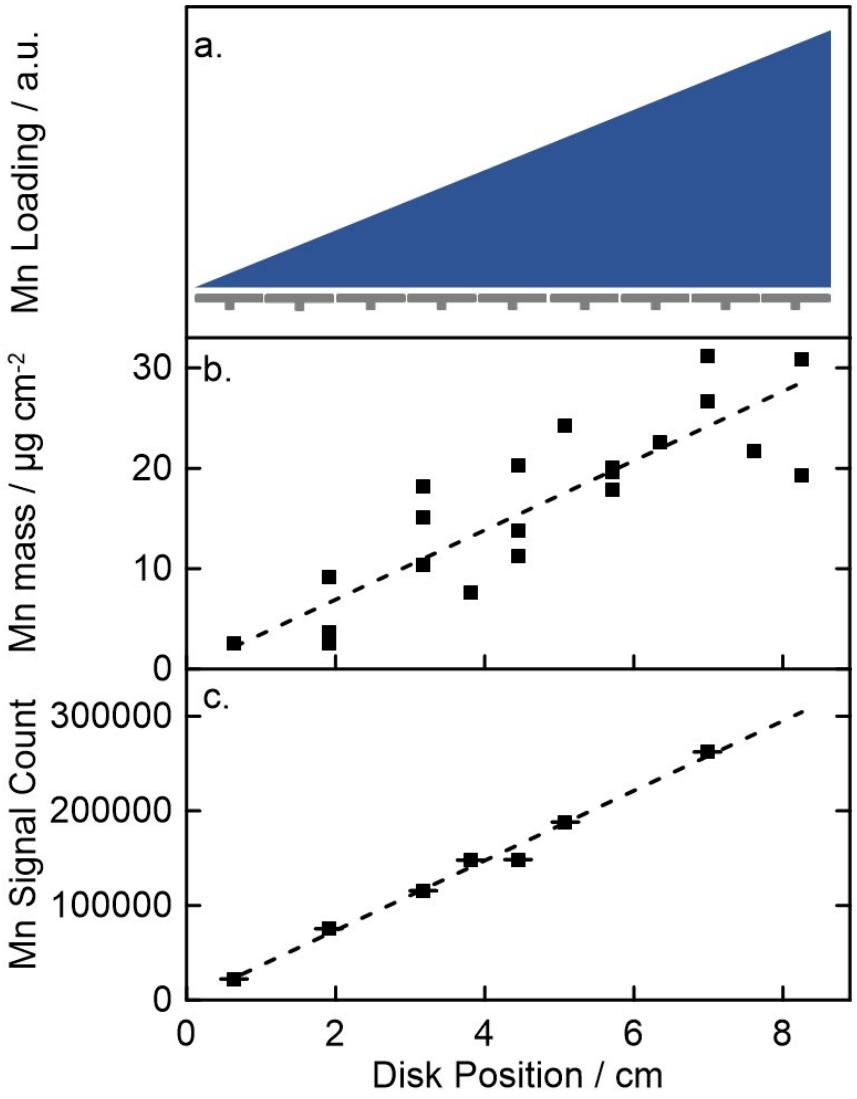

Figure 3.13 - a) schematic sputtering loading vs. position on the sputtering track. b) Mn loading (µg cm^{-2}) vs. position on the sputtering track. c) µ-XRF Mn signal count per cm^2 vs. position on the fresh negative electrode exposed to the Mn sputtering procedure.

Micro X-ray fluorescence

Micro X-Ray Fluorescence (μ-XRF) is used in this study to map Ni, Mn and Co deposition at the negative electrode.[84] μ-XRF uses the principles of X-Ray Fluorescence (XRF) but has the sampling precision to quantify signals in the x and y direction, generating a two-dimensional mapping of a sample.

XRF measurements use high energy radiation to characterize specific atoms. Figure 3.14 shows the electron absorption (Figure 3.14a.), electron ejection (Figure 3.14b.) and election relaxation (c.) processes. An X-ray with enough energy will eject an electron from a lower energy level (n=1, K shell) of an atom (Figure 3.14a and Figure 3.14b). During the relaxation phase, another electron from a higher energy level (n=2,3,4...) will drop to the lower level (n=1) to stabilize the electron configuration. This transition of an electron from a higher energy level to a lower energy level will release the energy difference via radiation, called fluorescence (Figure 3.14c). The fluorescent rays can then be measured via a photon detector where specific energies of radiation can be identified and quantified. For different atoms, the relaxation process will have a unique energy associated with this transition, for example the associated energy for Mn is 5.900 keV and Ni is 7.480 keV.[90]

The penetration depth of the μ-XRF is expected to exceed the thickness of the electrode coating. According to the Beer-Lambert law, Equation 3.11 measures the fraction of x-ray intensity (I/I_o) at sample thickness, *t,* and with linear attenuation coefficient, μ_l.[91]

$$\frac{I}{I_o} = e^{-\mu_l t} \tag{3.11}$$

The calculated x-ray linear attenuation coefficient for $Rh_{K\alpha}$, $Mn_{K\alpha}$, $Ni_{K\alpha}$ and $Co_{K\alpha}$ in carbon are 0.74, 1.48, 0.32, and 0.40 cm^{-1}, respectfully (based on expected mass ratios of each component). These were compared with a sample thickness of 80 μm and showed intensity factors above 0.98, indicating that all transition metals throughout the electrode would be detected by this method.

μ-XRF measurements

The Mn-coated fresh electrode was used to calibrate signal counts measured with a M4 Tornado Micro-X-Ray Fluorescence Instrument (Bruker, Madison, WI, USA). Figure 3.13c shows the Mn signal counts vs. position on the electrode. The samples were placed in a vacuum sealed chamber directly on a motion stage. The sample analysis and imaging

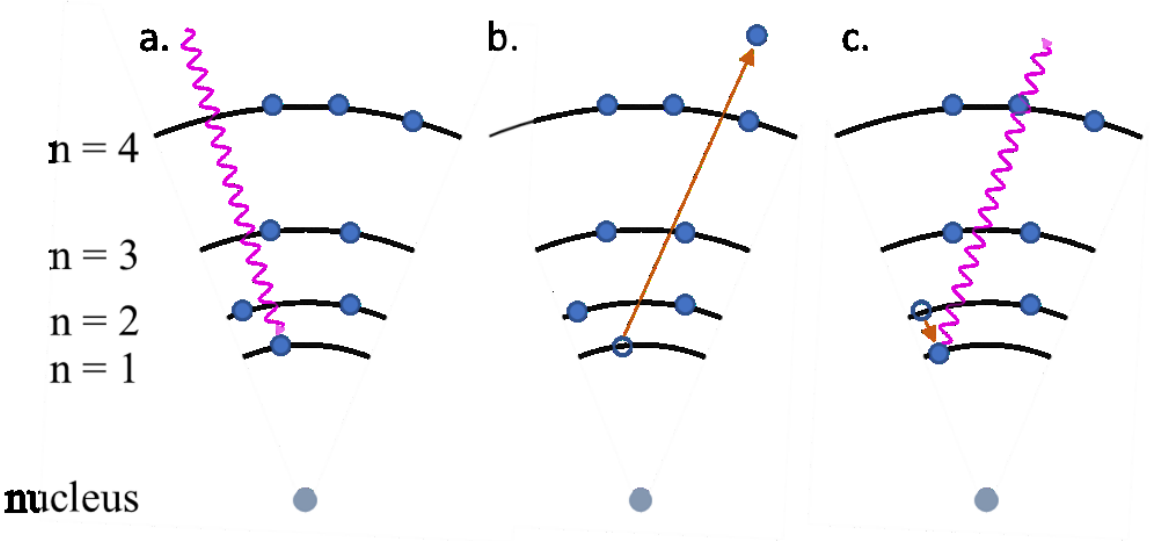

Figure 3.14 – a) an electron in the n = 1 orbital is shown absorbing X-ray radiation b) the electron is expelled from the n = 1 orbital. c). an electron from the n = 2 orbital drops to n = 1 orbital to take the favorable electron configuration and the net decrease of energy is released as fluorescent radiation.

were carried out with a Rh X-ray tube[92] using the 0-50 keV range and a tube current of 200 μA. Sample scanning was done at a rate of 4.00 mm sec^{-1} using a 40 μm spot size. Complete elemental analysis was performed at each position. The Mn signal count for the samples were then fitted using calibration data from Figure 3.13b and Figure 3.13c to determine the Mn mass per area on the electrodes. The average Mn loading over the sampled anode area was then calculated and is reported here. Error was calculated using a regression analysis of calibration curve at 95% confidence intervals. Ni and Co μ-XRF signals were also measured from the aged electrodes and were compared to the Mn μ-XRF signals.

A negative electrode from a dry pouch cell and from a freshly formed pouch cell were measured via μ-XRF to quantitatively show the magnitude of Mn deposition before electrolyte filling and after formation, before cycling. Figure 3.15a shows the Mn loading on the negative electrode of a dry cell (0.0 ± 0.0 μg cm^{-2}) and Figure 3.15b shows the Mn loading on the negative electrode of a freshly formed cell (0.52 ± 0.09 μg cm^{-2}). Figure 3.15 shows images of the Mn signal maps over the approximately 3 cm x 2 cm electrode studied. The negative electrode from a dry fresh pouch cell showed no Mn signal. Similar measurements on the copper foil current collector also showed no Mn signal.

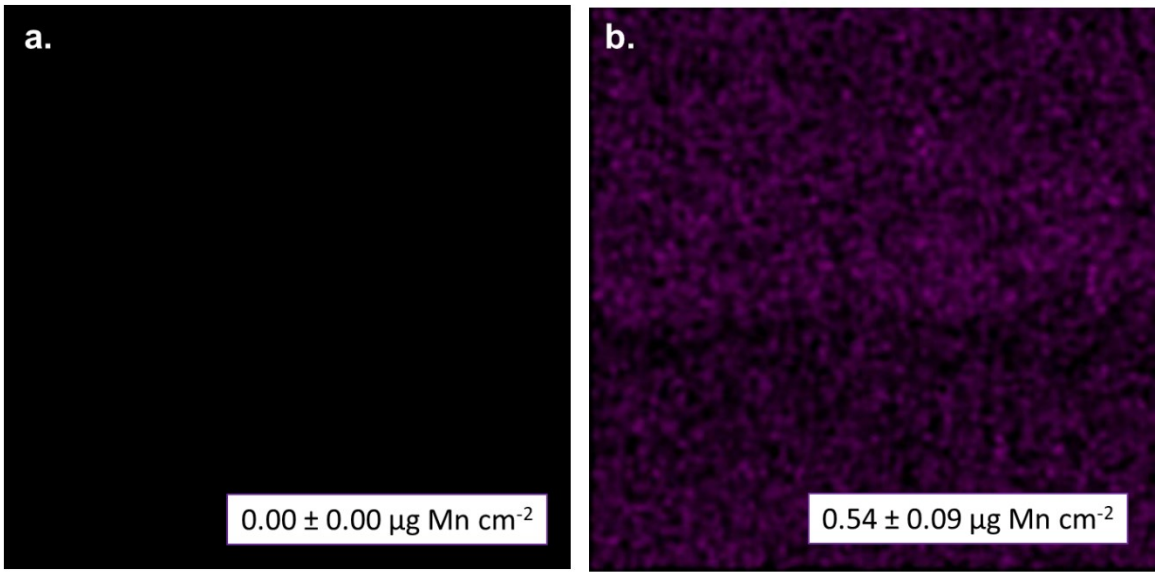

Figure 3.15 - a) Mn µ-XRF signal for negative electrode from dry pouch cell showing no Mn. b) Mn µ-XRF signal for negative electrode from a NMC532/graphite cell after formation showing Mn on the negative electrode. The images represent a portion of the electrode that was 3 cm x 2 cm.

Summary

The methods developed in this work, including the centrifuge extraction, organic analysis via GC-MS and salt analysis via ICP-MS, have made it possible for pure electrolyte to be removed from a pouch cell and for the semiqualitative composition of both the organic and salt components of the electrolyte to be determined. The method also allows the electrodes to be recovered for additional analysis. In this work, µ-XRF was used to evaluate the extent of transition metal dissolution on the negative electrodes.

4. CHAPTER 4 – CHARACTERIZATION OF ELECTROLYTE AND NEGATIVE ELECTRODES FROM NMC532 CELLS CYCLED AT VARIOUS UPPER CUTOFF POTENTIALS

This work was adapted from the article:

L.M. Thompson, W. Stone, A. Eldesoky, N.K. Smith, C.R.M McFarlane, J.S. Kim, M. B. Johnson, R. Petibon and J.R. Dahn

Quantifying changes to the electrolyte and negative electrode in aged NMC532/graphite lithium-ion cells (submitted to Journal of Electrochemical Society on June 28, 2018)

Will Stone prepared the pouch cells for this study and measured the volume of gas produced. Lauren Thompson developed the electrolyte extraction method, preparation and validation, the GC-MS modified method, preparation and validation and the ICP-MS method preparation and validation used in this study. The GC-MS instrumentation method was adapted from Remi Petibon and the ICP-MS instrumentation method was adapted from Nathan Smith and Jong Kim. Ahmed Eldesoky performed XRF analysis under supervision of Chris McFarlane. Lauren Thompson prepared all figures except Figure 4.3 and Figure 4.4 (prepared by Jeff Dahn). Jeff Dahn provided guidance throughout method design, validation and interpretation. Lauren Thompson prepared the manuscript which was edited and approved by the appropriate authors.

This chapter considers a matrix of cells cycled to various upper cutoff potentials. The results from the electrolyte analysis of these cells are presented in this chapter to evaluate the effect of increasing the energy density of these cells via increasing the upper cutoff potential. The electrolyte used has previously been shown to effectively passivate the negative electrode after formation and extend the cycle lifetime of the cell. The cells were opened after over 750 charge and discharge cycles to evaluate the long-term electrolyte degradation mechanisms occurring within the cell.

Cell and cycling specifications

The matrix of cells considered in this chapter includes NMC532 cells that were filled with 1.1 m $LiPF_6$ salt in EC:EMC (3:7) with 2% FEC and 1% DTD as additives. The cells were charged and discharged at 55°C for over 750 cycles to various upper cutoff potentials (4.0, 4.1, 4.2, 4.3 and 4.4 V) using a Neware charging device. A constant current – constant voltage mode was used to charge full cells at C/3 (80 mA) until the upper cutoff potential was reached. Then the voltage was fixed until the current was less than C/20 (11 mA). Every 50 cycles, a C/10 (22 mA) charge and discharge was performed. Cells available for electrolyte analysis included one cell cycled to 4.2 V, one cell cycled to 4.3 V, two cells cycled to 4.0, two cells cycled to 4.1 and two cells cycled to 4.4 V upper cutoff potentials.

Figure 4.1a shows the capacity vs. cycle count for the NMC532/graphite cells studied here. The upper cutoff potentials for the tested cells are given in the legend of Figure 4.1. As expected, the initial capacity increases with increased upper cutoff potential. Cells cycled at higher upper cutoff potentials (4.3 V and 4.4 V) had lost 30 mAh of capacity. All cells have lost on average 12.2 ± 0.2 % capacity after almost 750 cycles at 55ºC. Figure 4.1b

shows the difference in average charge and discharge voltage (ΔV) vs. cycle count. This polarization tracks impedance growth (mostly of the SEIwhich increases as upper cutoff potential increases. Cells cycled at 4.4 V have faster impedance growth than cells cycled at 4.0 V.

Results

Figure 4.2 shows post cycling analysis for the matrix of cells considered in this Chapter. Figure 4.2a shows gas production after cycling plotted for the five different upper cutoff potentials. There is a general trend of increased gas production as the upper cutoff potential increases, however, one cell at 4.0 V exhibited gas production comparable to the 4.4 V cells, therefore no definitive trend can be reported. The scale of gas production for these pouch cells remains small (< 0.4 mL) compared to the original volume of the cells (2.5 mL).

Figure 4.2b shows DMC and DEC solvent fractions compared to EMC plotted as the fraction of transesterification, defined here to be:

[Fraction DMC + Fraction DEC]/[Fraction DMC + Fraction DEC + Fraction EMC]

Figure 4.2b shows that transesterification increases as the upper cutoff potential increases from 0.0 % transesterification at 4.0 V to 11.8 ± 0.2 % at 4.4 V. DMC and DEC have been shown to be formed from the Li-alkoxide facilitated trans-esterification reaction for EMC.[28,30] In freshly formed cells the presence of these products indicates the existence of Li-alkoxides, likely formed from the reduction of EMC at an un-passivated negative electrode.[28,30,45] Li-alkoxide formation and subsequent reaction with linear carbonate are

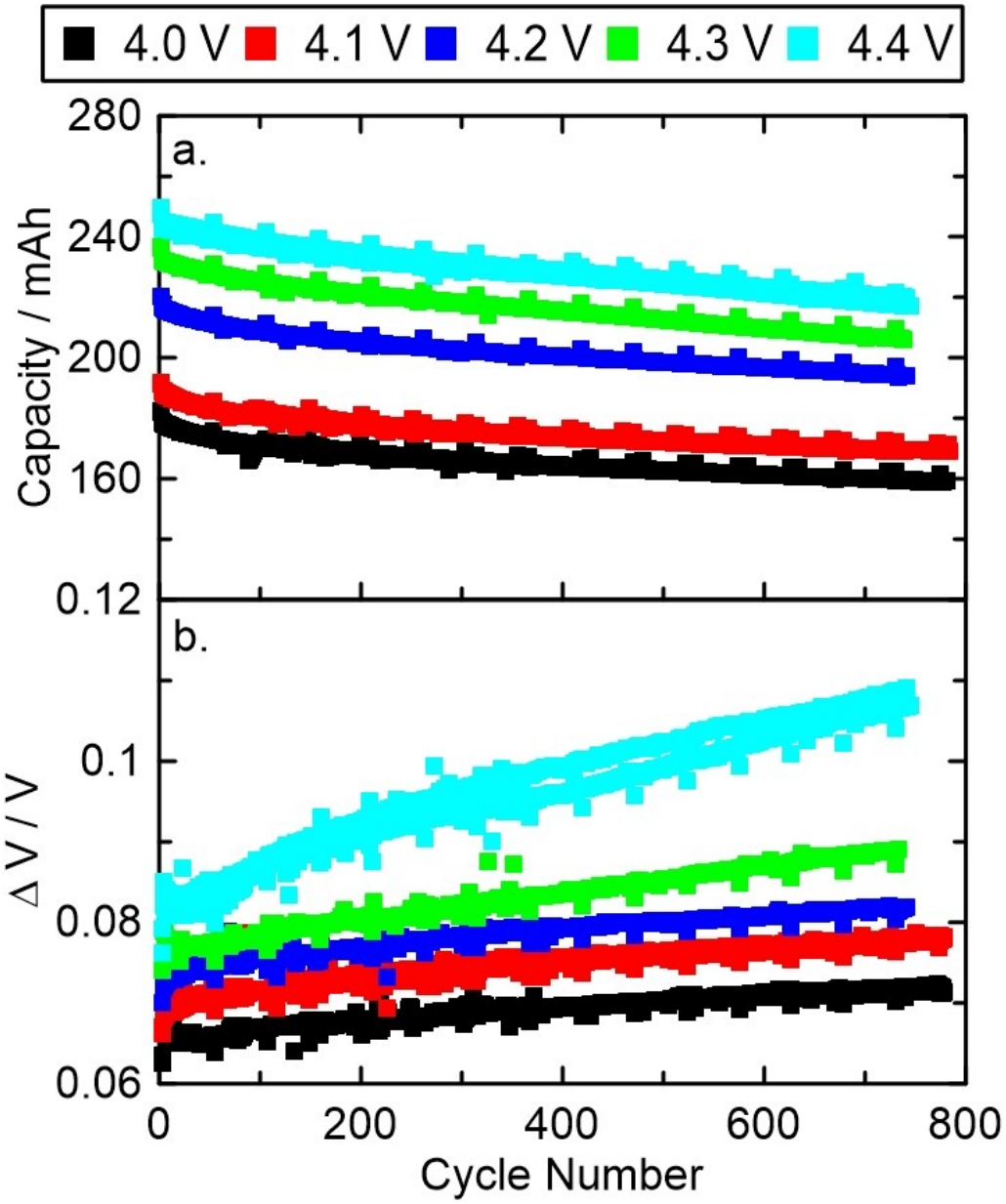

Figure 4.1 – a) Capacity (mAh) vs. cycle number for NMC532/graphite cells tested using currents of C/3 (CCCV) at 55ºC. The upper cutoff potential of the various cells is given in the legend. b) ΔV vs. cycle number for cells considered.

shown in Equation 4.1 and Equation 4.2, respectively. The presence of transesterification products later in life was hypothesized to originate from the passivation of dissolved transition metals upon deposition at the negative electrode.[93]

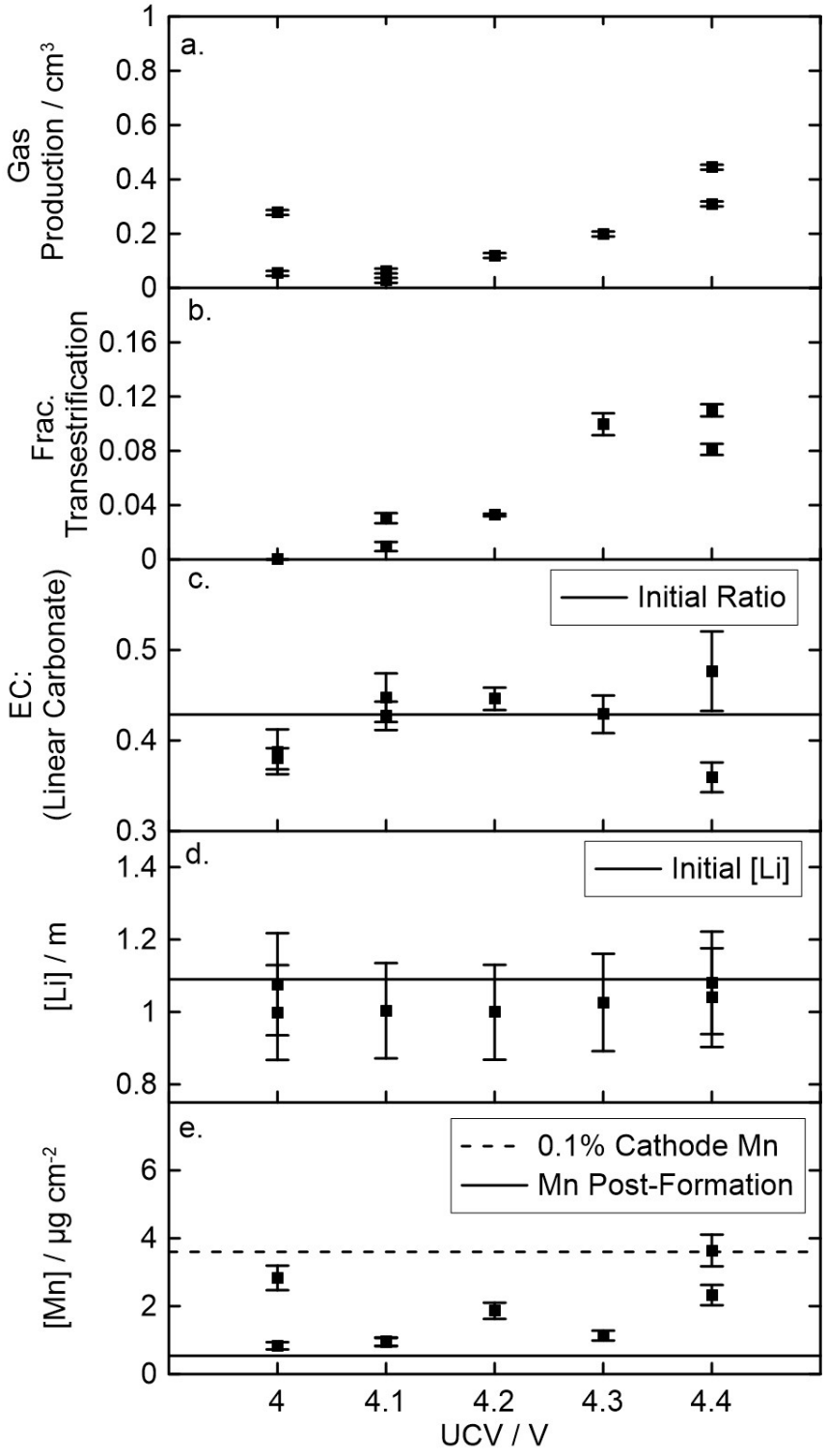

Figure 4.2 - Post-testing analysis results for the cells described by Figure 4.1. a) gas produced. b) mass fraction of trans-esterification. c) EC: (linear carbonate) mass ratio. d) Li^+ concentration. e) Mn loading on the negative electrode all plotted vs. upper cutoff potential.

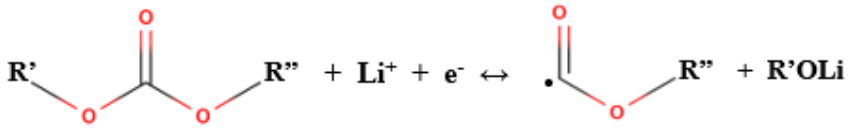

(4.1)

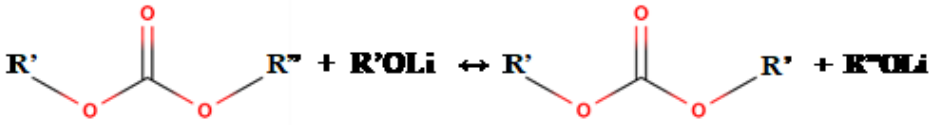

(4.2)

However, limited transition metals found at the negative electrode, as discussed below, suggests another mechanism is involved. Li-alkoxides can also facilitate reactions between linear carbonates and EC. DEOHC and DMOHC are dimerization products also expected in the presence of Li-alkoxides as shown by Equation 4.3.[28,30,45]

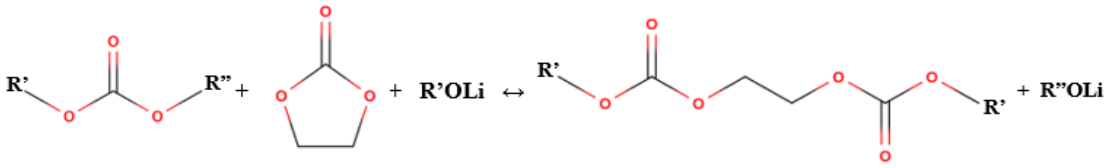

(4.3)

DMOHC and DEOHC were not observed in any of the electrolyte samples to the detection limit of 50 ppm by weight. The detection limit was determined by smallest distinguishable peak area of DMOHC and DEOHC. This suggests that Li-alkoxides were not present and another mechanism is responsible for the transesterification of linear carbonates and that the dimerization reaction of EC and EMC can be facilitated by another species. Some studies, such as that conducted by Zhang et al. have suggested that the presence of PF_5, a decomposition product of PF_6 (see Equation 2.2), can act as a Lewis acid to open the EC ring.[10,94] The opened ring can then react with EMC/DEC to form DEOHC. This reaction,

as shown in Equation 2.2, would be accompanied by Li^+ consumption, which is also not observed in this matrix (see Figure 4.2d).

Figure 4.2c shows the EC to linear carbonate (EMC, DMC and DEC) ratio. The EC:linear carbonate ratio was also monitored to observe any possible changes to the initial 3:7 weight ratio (shown by solid line in Figure 4.2c). The plotted ratios show no significant difference to the original EC:EMC ratio. Even cells with high fractions of transesterification have the same linear carbonate:EC ratio as the original electrolyte. This suggests that any EC or linear carbonate loss (gas formation, SEI formation) occurs at the approximately the same rate or is very small compared to the original amount of solvents in the cell. Given that the maximum volume of gas measured in a cell was only 0.4 mL, that 1 mL of electrolyte was added to the cells and a typical 700:1 gas:liquid volume ratio (at 1 atm pressure) for a typical liquid:gas transition one might conclude that only a small amount of solvent could have reacted. However, Ellis et al.[61] have recently shown that many gases generated in cells are also consumed, so that the amount of gas remaining in a cell may not represent the total amount generated during the life of the cell. In any event, whatever the mechanism, the EC : linear carbonate ratio in these cells does not change after about 750 cycles at 55ºC.

Figure 4.2d shows the Li^+ concentration remaining in the electrolyte measured by ICP-MS. The original Li^+ concentration is shown as the solid horizontal line. The results show no significant difference between measured Li^+ concentration and the original Li^+ concentration. This suggests that Li^+ has not been consumed or has been consumed at the same rate as the solvent in these cells. Readers should take care to notice that these are very good cells showing excellent capacity retention at 55ºC (see Figure 4.1a).

Figure 4.2e shows the Mn loadings found at the negative electrode for each cell. The results show an increase in Mn deposited at the negative electrode in cells tested at higher upper cutoff potentials. However, one pair cell at 4.0 V also shows higher amounts of Mn, making it hard to determine a definitive trend. The Mn loading found on freshly formed cells is included as the solid line to show that the amount of Mn on the negative electrode did not increase substantially for cells tested to upper cutoffs of 4.1 and 4.3 V compared to freshly formed cells. The original NMC532 positive electrode loading of 21.3 mg cm^{-2} yields a Mn loading in the positive electrode of 3.6 mg cm^{-2}. If 0.1% of the Mn from the positive electrode migrated to the negative electrode, a loading on the negative electrode of 3.6 μg cm^{-2} would be expected. This loading level is shown in Figure 4.2e as the dashed line.

For spherical NMC532 particles having a radius of 3 μm (an approximation for the single crystal NMC532 used in these cells) complete removal of 0.1% of the transition metals would represent a layer that is 0.5 nm thick or one to two atomic layers thick.[72] This is certainly an underestimate of the depth from which transition metals might dissolve in the NMC532 particles. If 10% of the transition metals in near-surface layers were to dissolve, then this might impact a depth of 5 nm or so which is consistent with many TEM images of reconstructed surfaces on NMC particles after testing. This comparison is included to emphasize the small magnitude of Mn dissolution in this matrix compared to prior cells which have experienced severe surface layer dissolution.

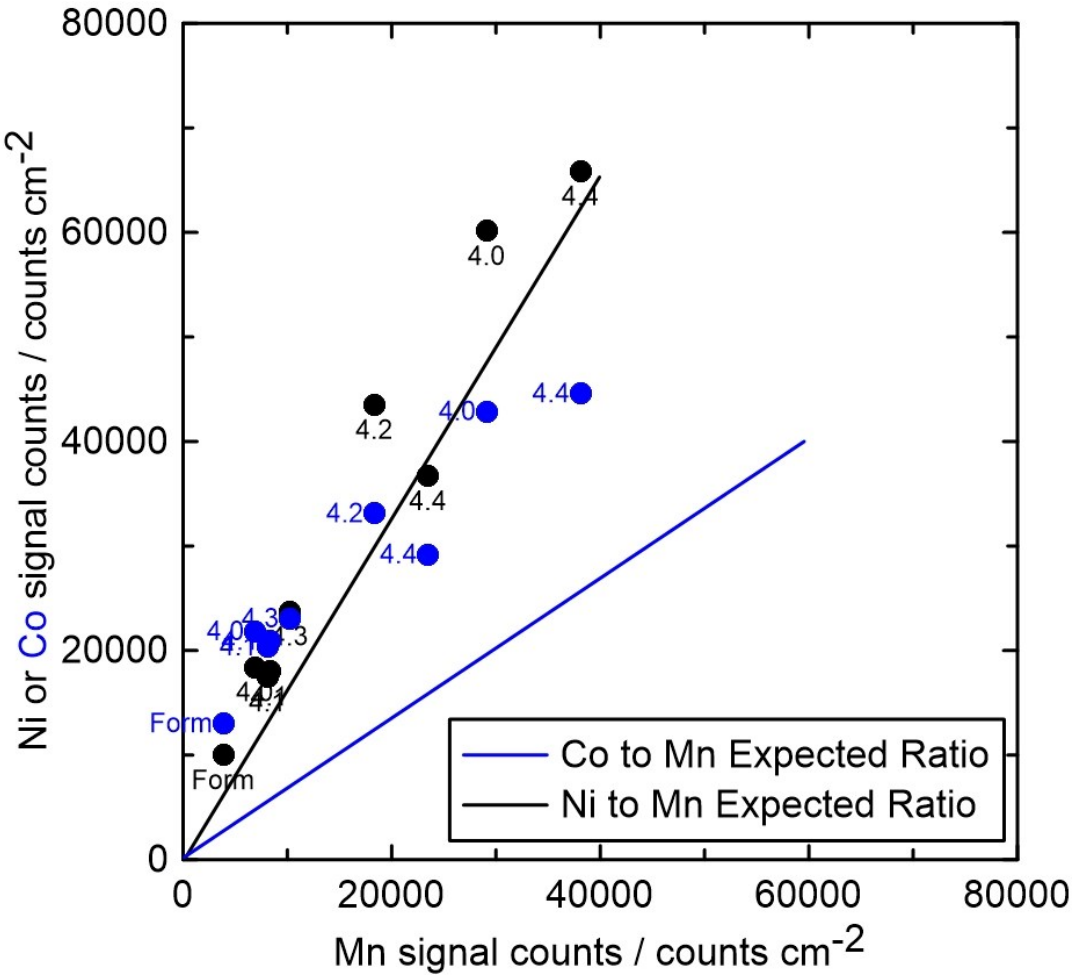

Figure 4.3 - Comparing the Ni (black) and Co (blue) μ-XRF signals to the Mn μ-XRF signal for the negative electrodes recovered from the cells described by Figure 4.1 and Figure 4.2. The solid black and solid blue lines represent the expected ratios of all transition metals have equal probability for dissolution from NMC532.

Figure 4.3 compares the raw μ-XRF count rates for Ni (black data points) and Co (blue data points) compared to Mn as found on the negative electrodes in the tested cells. The solid black and solid blue lines in Figure 4.3 represent the expected ratios based on equal probabilities for dissolution of Ni, Mn and Co from NMC532. The relative sensitivity of the μ-XRF instrument was estimated by measuring the count rates per cm^2 from pure Ni, Co and Mn metal samples which were found to be in the ratio 1:0.96:0.81. These correction factors have not been applied to the data in Figure 4.3. The purpose of Figure 4.3 is to

show that Ni and Co dissolve from the NMC532 positive electrode to approximately the expected extent and that Mn does not dissolve in far greater quantities than Ni and Co. In a recent study published by Gilbert et al.[95] it was also observed that transition metals were deposited onto the negative electrode at the expected mass ratios.

Comparison to results from Gilbert et al.[95]

Figure 4.4 compares results for Mn deposition on the negative electrode from this study to those recently published by Gilbert et al.[95] Gilbert et al. used cells containing NMC532 and NCA positive electrodes (average secondary particle radius of 6 μm) and a graphite negative electrode. Gilbert et al. reported the Mn content as weight fraction of the negative electrode, so it was necessary to convert the data in Figure 4.2 into the same units. This required some thought, because the positive and negative electrode loadings used in ref. 94 were different than those used here. Gilbert et al. used a positive loading of 9.2 mg cm^{-2} while a loading of 21.3 mg cm^{-2} was used here. However, because the negative/positive electrode mass ratios in the cells ref. 94 and the cells studied here were about the same, the negative electrode loading scales with the positive electrode loading. Therefore, in the end, it was only necessary to divide the Mn mass loadings in Figure 4.2 by the negative electrode mass per unit area (12.8 mg cm^{-2}) to get a meaningful comparison.

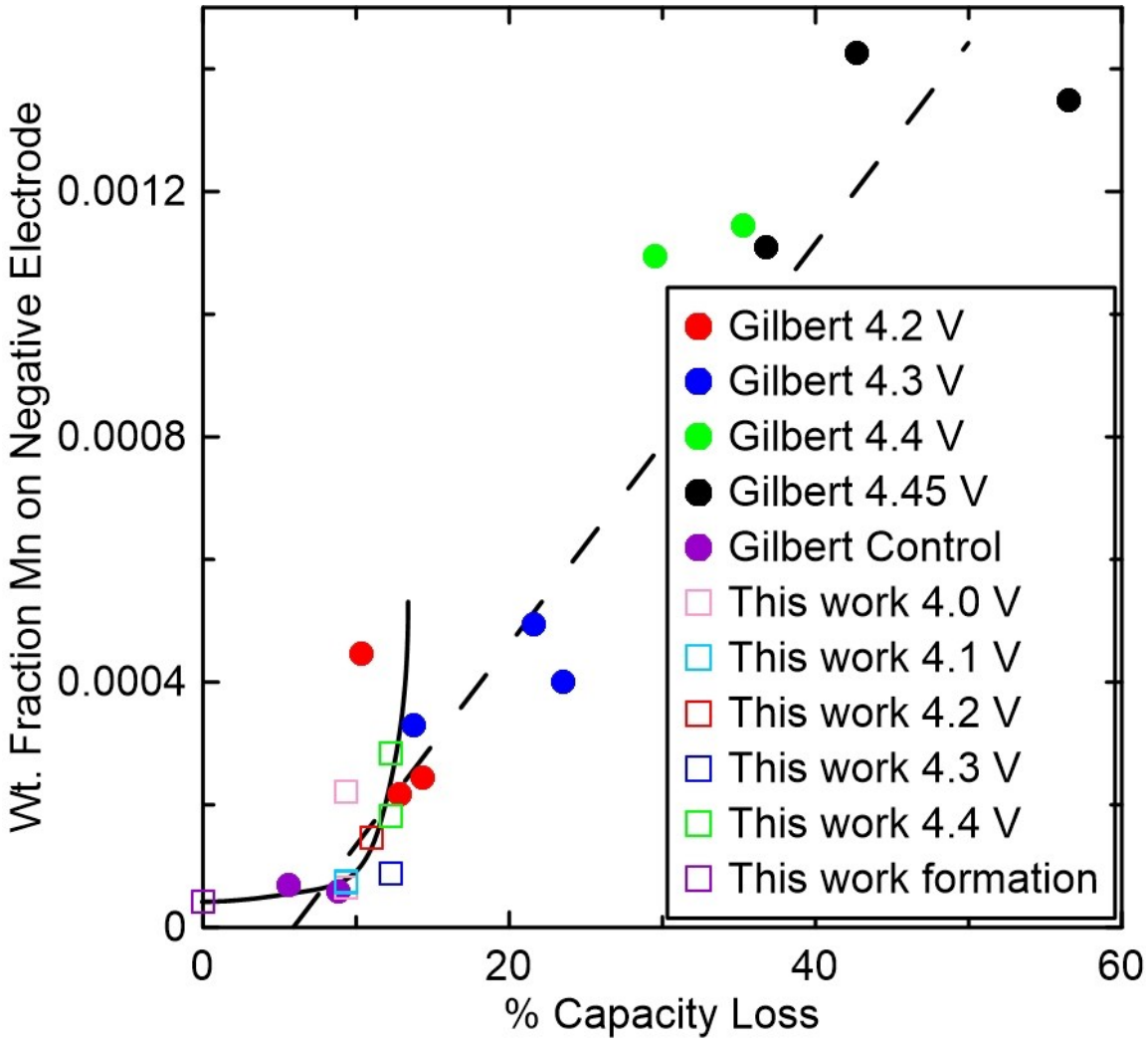

Figure 4.4 - Comparing results for Mn deposition on the negative electrode in this study to those from Gilbert et al.[95] The legend in the Figure indicates the upper cutoff voltage and which study the data points correspond to. The solid line shows a trendline for the data from this work. The dashed line shows a linear fit of data from Gilbert et al. Cells in the Gilbert et al. study were tested at 30ºC for 900 hours. Cells in this study were tested at 55ºC for 5000 hours.

Gilbert et al. found that the amount of Mn deposition at the negative electrode increased as the fraction of capacity loss increased. The NMC532/graphite coin cells in their study contained 1.1 M $LiPF_6$ in EC:EMC (3:7) and no additives. Their cells experienced 37% capacity loss after cycling between 3.0 and 4.4 V at 30ºC for only about 900 hours (200

cycles at C-rate). By contrast, cells in this study experienced a maximum of 12.2% capacity loss after cycling for over 5000 hours at 55°C (750 cycles at C/3 rate). Figure 4.4 suggests that the Mn loading found on cycled negative electrodes in this study appears to fall within the trend identified by Gilbert et al. However, it very important to realize that the Mn loading on the negative electrodes in the cells of this study measured directly after formation (with no capacity loss) does not agree with the trend proposed by Gilbert et al., but rather suggests a relationship schematically shown by the curved solid line in Figure 4.4.

The data in Figure 4.4 for the cells in this study suggests that when transition metal dissolution is controlled through the selection of suitable additives and/or other strategies, transition metal dissolution and subsequent deposition on the negative electrode does not play a dominant role in the failure mechanism of NMC/graphite Li-ion cells. This is a very important point that readers need to appreciate.

Gilbert et al.[95] state in their conclusions: "… *it is our belief that controlling TM dissolution from the oxide surfaces through various possible preventive measures can lead to the development of high voltage LIBs with extended operation time. Any method of reducing the stress and fracture of oxide particles that leads to enhanced TM dissolution should reduce both capacity fade and impedance rise. These methods could include changes in oxide synthesis conditions to strengthen primary particle boundaries, oxide coatings and electrolyte additives to minimize corrosion reactions at the oxide-electrolyte interfaces, etc.*"

The electrolyte mixture in this study likely provides more stable SEI layers on both the positive and negative electrode which prevents severe transition metal dissolution. Since

transition metal dissolution has been shown to be driven by HF formation from PF_6^-,[96] it could also be that the difference in the results from this study and the Gilbert study originates from relative amounts of formed PF_5 and HF. This is also consistent with the lack of dimerization products measured in the electrolyte in this study.[97] Additionally, Li et al found that NMC532/graphite pouch cells with single crystal positive electrode materials, as used in this study, had longer cycling lifetime and better performance than cells with polycrystalline materials.[98] Figure 4.4 suggests that further reductions in transition metal dissolution and deposition at the negative electrode may have little impact on lifetime, however, more data points are needed, particularly at larger capacity losses, to make an adequate comparison and prediction.

Fraction of transesterification and Mn loading vs. impedance growth

Figure 4.1b showed that the difference in average charge and discharge voltage (ΔV) increased with cycle number more rapidly as the upper cutoff potential increased. Since ΔV is a measure of impedance growth in the cells it is interesting to see how it correlates to the amounts of degradation products found. The value of ΔV at the end of the testing in Figure 4.1b was used for comparison. Figure 4.5a shows that the fraction of transesterification products (DMC and DEC) increased as ΔV increased, suggesting that the amount of transesterification may be related the impedance growth. It would not be prudent to suggest causality without knowing the reaction mechanisms responsible for the transesterification. Similarly, Figure 4.5b may suggest the Mn loading at the negative electrode increases as ΔV increases but the data shows significant scatter. Again, it is not

possible to suggest a causal relationship between Mn on the negative electrode and impedance growth, when the amount of Mn on the negative electrode is very small.

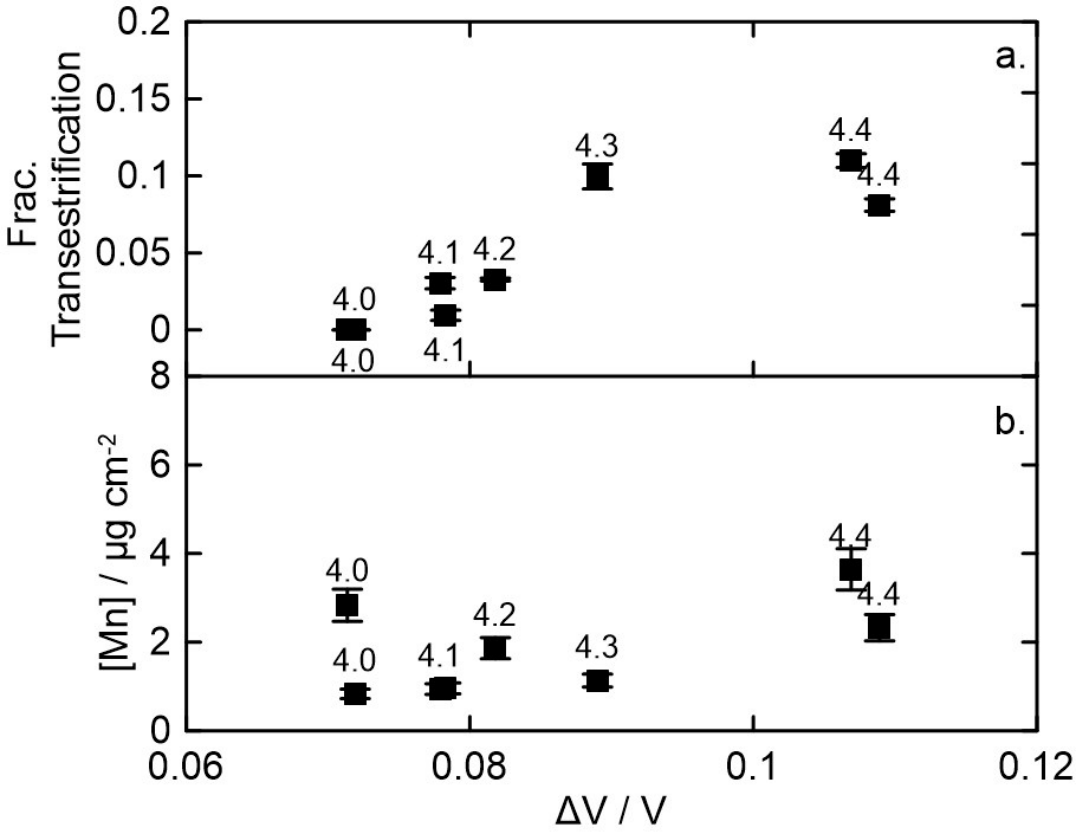

Figure 4.5 - a) Fraction of transesterification compared to ΔV measured at the end of the charge-discharge testing shown in Figure 4.1. b) Mn loading on the negative electrode compared to ΔV.

Concluding remarks

The results showed that increased upper cutoff potential increased the amount of the transesterification products DMC and DEC. The increased fraction of transesterification products in cells tested to higher potential correlated well to the increase in impedance growth rate (Figure 4.1b and Figure 4.5a) in cells tested to higher potential. This suggests that the mechanism of impedance growth is associated with electrolyte oxidation at the

positive electrode side and that transesterification is an indicator or a product of these reactions.

The amount of transition metals transferred from the positive to the negative electrode was less than 0.1% of all the transition metals in the positive electrode for all the cells tested. There may be an increase in the amount of transition metals transferred with upper cutoff potential, but scatter in the data makes it hard to discern if this trend is real. Cells tested at 4.1 V and at 4.3 V for 8 months and 55ºC showed only about twice as much Mn on the negative electrode as freshly formed cells (Figure 4.2e). It is therefore difficult for the authors to believe that transition metal dissolution in **these cells** is a significant contributor to cell capacity loss.

There was no significant change in salt content or EC:linear carbonate ratio in these cells compared to the original electrolyte even for cells tested to 4.4 V. These results are not too surprising given that all cells had less than 10 % capacity loss and were all decreasing in capacity at similar, steady rates with no indication of cell failure. Future studies will consider older cells with more extreme capacity loss.

The results from this study were compared to those of a similar study by Gilbert et al.[95] The amounts of Mn and other transition metals found on the negative electrode were an order of magnitude smaller than the Gilbert et al. study, even though cells studied here were tested for 5 times longer and at 55ºC (this work) instead of 30ºC (Gilbert et al.). These results point to the importance of electrolyte additives and other strategies in controlling transition metal dissolution.

5. CHAPTER 5 – ELECTROLYTE AND NEGATIVE ELECTRODE ANALYSIS FOR NMC532 CELLS CONTAINING MA AND CYCLED TO VARIOUS UPPER CUTOFF POTENTIALS

Lauren Thompson prepared the pouch cells for this study and measured the gas production. Lauren Thompson developed the electrolyte extraction method, preparation and validation, the GC-MS modified method, preparation and validation and the ICP-MS method preparation and validation used in this study. The GC-MS instrumentation method was adapted from Remi Petibon and the ICP-MS instrumentation method was adapted from Nathan Smith and Jong Kim. Ahmed Eldesoky performed XRF analysis under supervision of Chris McFarlane. Lauren Thompson prepared the text and all figures except Figure 5.4 (adapted from Jeff Dahn). Jeff Dahn provided guidance throughout method design, validation and interpretation.

Recently low viscosity co-solvents have been explored to decrease electrolyte viscosity, increase electrolyte conductivity and allow for increased charging rates of Li-ion cells.[99-101] For this cell design and these electrode loadings (described in Chapter 3), the cells containing MA could be charged at 2C while cells without MA showed unwanted Li-plating at 1.5C.[102] However, too much MA as a solvent can decrease cell lifetime and it has been found that a reasonable fraction of MA is around 20% MA.[100] The results discussed in this chapter include electrolyte analysis from cells both with and without MA as a co-solvent that have been charged and discharged for over 700 cycles. Due to limited charger availability the 4.1 V cell with MA was omitted.

Results from this matrix will need to be replicated as future work due to a combination of limited cell availability (one cell per condition), potentially poor instrumental connections, errors in GC-MS sampling (wrong inlet liner) and mis-labeled linear carbonate (labeled EC:EMC by manufacturer then tested as EC:DMC). Still, the findings from the electrolyte and XRF analysis including the salt concentrations from the ICP-MS, the lack of detected dimerization products, and measured transition metals on the negative electrode expose clues of electrolyte fate and cell aging mechanisms.

Cell and cycling specifications

Figure 5.1 shows the capacity vs. cycle count for the NMC532/graphite cells included in this matrix. A Moli cycling instrument was used to charge and discharge these cells at C/3 (80 mA) in a 55.0 ± 0.1 ºC temperature-controlled box. Every 50 cycles a current of C/20 was used for 2 charge and discharge cycles to check the absolute capacity. The electrolyte used was either 1.1 m $LiPF_6$ in EC:DMC + 2% FEC + 1% DTD or 1.1 m $LiPF_6$ in 80% EC:DMC, 20% MA + 2% FEC + 1% DTD. The upper cutoff potentials for the tested cells were 4.1, 4.3, and 4.5 V. As the upper cutoff potential increased, the capacity also increased. For both electrolytes used, cells cycled at higher upper cutoff potentials (4.5 V) had lost ~55 mAh of capacity where the cells (without MA) cycled to (4.1 and 4.3 V) had lost ~30 mAh of capacity. All cells lost on average 16 ± 5 % capacity after almost 750 cycles at 55ºC.

Figure 5.1a also shows inconsistent capacity measurements around 220 cycles. This drop in capacity for all cells was due to a change in the charging program which had a lower

upper cutoff potential but was corrected after ~20 cycles. The second inconsistent measurements occurred for both cells cycled to 4.5 V and for one of the cells without MA cycled to 4.3 V at around to 550 cycles. This occurred after the cells were measured via differential thermal analysis (DTA) and could be from capacity loss or, more likely, a poor electrical connection.

Figure 5.1b shows the difference in average charge and discharge voltage (ΔV) vs. cycle count for both electrolytes in this matrix. The polarization tracks impedance growth and is shown to increase as upper cutoff potential increases. In early stages of cycling, the cells cycled to 4.5 V experienced a notably higher rate of impedance increase. The cells cycled to 4.3 V and lower had very little polarization growth. The cycling protocol changes mentioned in the previous paragraph appear to also affect the impedance growth. A slight decrease in polarization can be observed around 220 cycles where the protocol was modified, however a significant difference is not discernable due to charge potential variations. The poor reconnection around 550 cycles and the sudden drop in capacity for the cells charged to 4.5 V also coincides with a sudden increase in measured impedance, which could also originate from a poor electrical connection. Also, after this time, the cell cycled to 4.3 V without MA experienced an inconsistent but overall increase in impedance, but the cell cycled to 4.3 V with MA had a slight decrease in measured impedance. These results are likely due to a poor electrical connection causing irregular voltage readings.

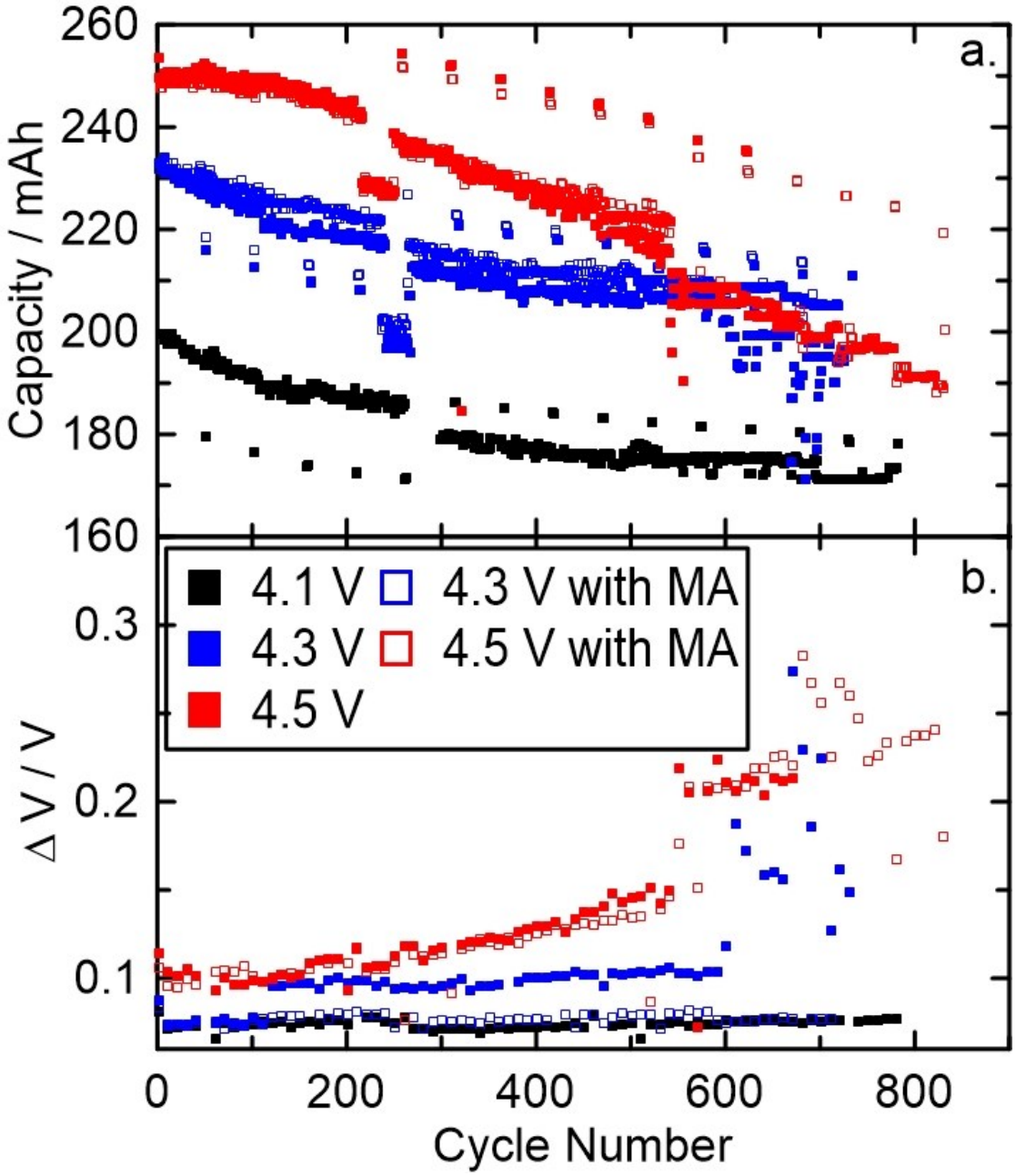

Figure 5.1 – Discharge capacity (mAh) vs. cycle number for NMC532/graphite cells tested using currents of C/3 (CCCV) at 55ºC. The upper cutoff potential of the various cells is given in the legend.

Results

Figure 5.2a shows the volume of gas produced after cycling at the various upper cutoff potentials. As the upper cutoff potential increased, the volume of gas produced increases. As measured in previous studies, the cells containing MA showed larger volumes of gas produced, especially when cycled to 4.5 V.[100,102] The gas produced is likely due to electrolyte oxidation at the positive electrode[100] and is consistent with the lack of Li^+ inventory loss as will be presented below. Overall the gas production for all cells is small (< 0.6 mL) compared to the original volume of these cells (2.5 mL).

Figure 5.2b shows the fraction of MA remaining in the cells as well as the original calculated fraction of MA for the electrolyte (solid line). As expected, no MA was found in cells that did not originally contain MA. The measured fraction of MA for cells containing MA was within the original fraction (0.193 ± 0.008) for the cell cycled to 4.3 V and slightly smaller for the cell cycled to 4.5V.

In an additional matrix, the fraction of MA was measured after formation. The fraction of MA in the solvent found after formation was slightly higher (0.21 ± 0.02) than the original MA fraction (0.171 ± 0.008), indicating the solvent or additives were consumed faster than MA. The fraction of MA found in electrolyte after about 750 cycles is within the range of the fraction found after formation for cell cycled to 4.3 V but slightly lower for cells cycled to 4.5 V.

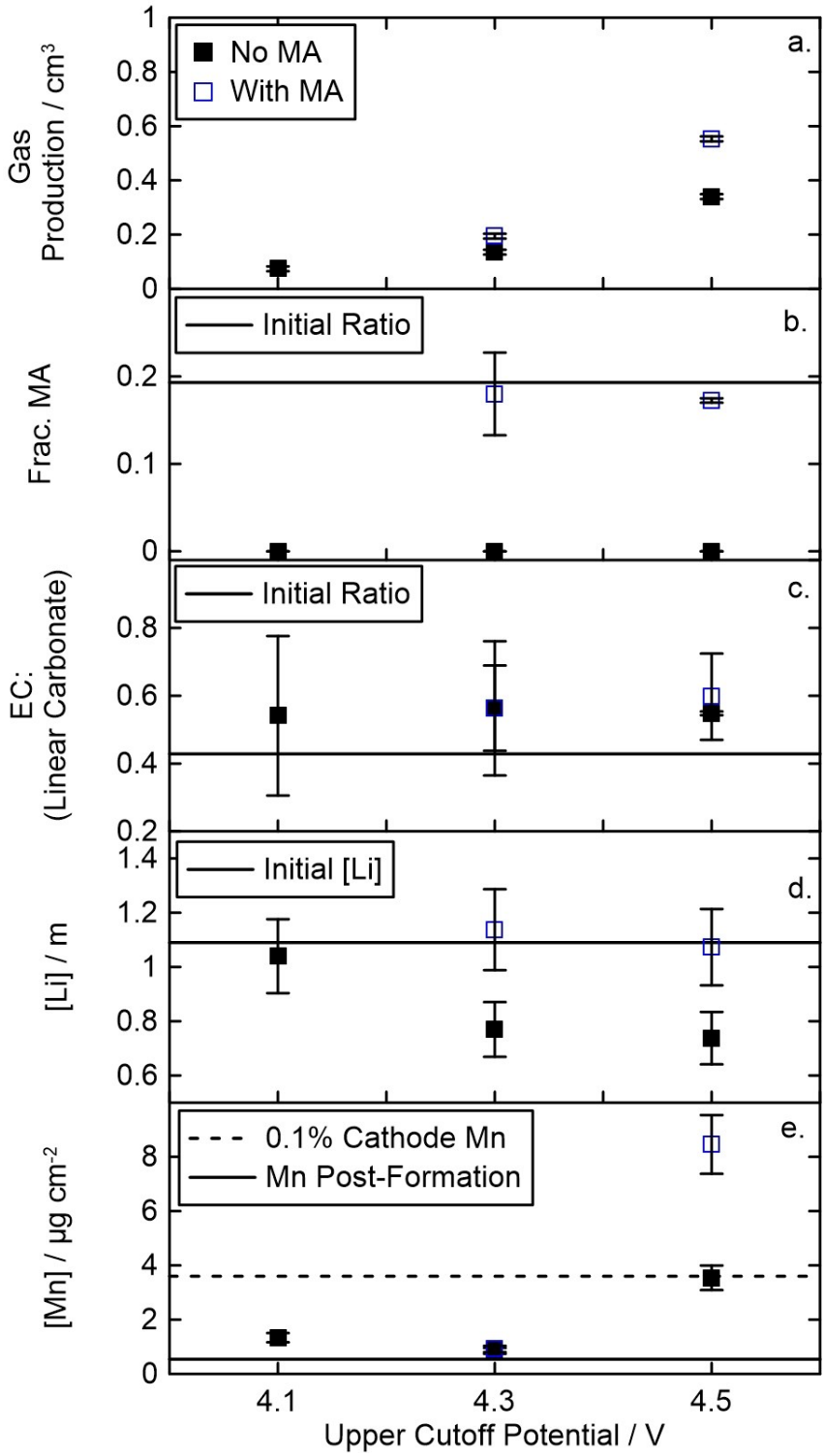

Figure 5.2 - Post-testing analysis results for the cells described by Figure 5.1. a) gas produced. b) mass fraction of MA. c) EC: (linear carbonate) mass ratio. d) Li^+ concentration. e) Mn loading on the negative electrode all plotted vs. upper cutoff potential.

Figure 5.2c shows the calculated EC:linear carbonate ratio for the various upper cutoff potentials and the electrolyte mixtures. On average, the measured ratios are larger than the original EC:DMC ratio of 3:7. These results are inconsistent with the ratios observed in Chapter 4 and are not as reliable as previous findings as the wrong inlet liner (for splitless rather than split injection) was used during sample delivery. This also explains the larger variation in ratios for the same sample as shown by the confidence intervals.

The fraction of transesterification was not able to be calculated for these cells as the transesterification product of DMC is DMC. GC-MS analysis also showed no DMOHC or DEOHC for these cells which is consistent with the results from Chapter 4.

Figure 5.2d shows the Li^+ concentrations measured using ICP-MS compared to the original calculated Li^+ concentration (solid line). The results show a decrease in salt concentrations (~30%) for the cells without MA cycled to 4.3 V and 4.5 V while the salt concentration for the cell cycled to 4.1 V is not significantly different from the original concentration. For cells containing MA, the Li^+ concentration is also not significantly different than the original Li^+ concentration. While the performance and impedance for these cells are similar (see Figure 5.1) it is interesting that the concentration of Li^+ differs for these cells.

The disappearance of Li^+ from the electrolyte must also consume an anion species as well. Products of these reactions, discussed in Chapter 2, include LiF and $LiPO_2F_2$. LiF and PF_5, as described by Equation 2.1, originate from the decomposition of $LiPF_6$. $LiPO_2F_2$ originates from the reaction between $LiPF_6$ and trace water (Equation 2.2) and from the reaction between Li_2CO_3 and $LiPF_6$ as shown in Equation 5.1.[61,103]

$$2\,Li_2CO_{3\,(s)} + LiPF_{6\,(sol)} \leftrightarrow 2\,CO_{2(g)} + 4\,LiF_{(s)} + LiPO_2F_{2\,(s)} \qquad (5.1)$$

Li_2CO_3 is a product of EC reduction as shown in route (b.) of Figure 2.3, however, Zhang et al. found that CO_2 produced by electrolyte oxidation in cells can later be consumed to form Li_2CO_3.[103] It is expected that at the higher upper cutoff potentials, more CO_2 is produced via electrolyte oxidation which can react with Li^+ and e^- to form Li_2CO_3 and can further consume $LiPF_6$ to remove salt from the electrolyte solution.[61] This proposed reaction would explain why electrolyte from cells cycled to the higher upper cutoff potentials experience a decrease in salt concentration.

These salt consumption reactions do not appear to occur in cells with MA. This is potentially due to alternative reduction and/or oxidation reactions that occur on the negative and positive electrode, respectively. Glazier et al. found that increasing MA content in electrolytes showed increased oxidation reactions occurring at the positive electrode in Li-ion cells.[100] Ma et al. also found through storage tests that parasitic reactions occur at the positive and negative electrode when 20% MA is used.[102] Perhaps the oxidation or reduction of MA initiates a shuttle reaction between electrodes which either limits CO_2 production or EC reduction and therefore limits Li_2CO_3 formation. This would limit the extent of reaction with $LiPF_6$ and therefore the consumption of electrolyte salt.

Future studies that include post-cycling electrode analysis will help identify the mechanism of Li^+ consumption in these electrolytes. This could help identify LiF or $LiPO_2F_2$ at the electrode surfaces. Gas characterization could also help in identifying the organic reactions that take place. Pouch bag storage experiments containing separate electrodes will also help identify any oxidation or reduction shuttle reactions in the presence of MA.

Figure 5.2e shows the measured Mn loading on the negative electrode taken from these cells. The solid line shows the level of Mn loading after formation while the dotted line represents 0.1% of the Mn loading from the positive electrode as described in Chapter 4. The Mn loadings on the negative electrodes from cells cycled to 4.1 V and 4.3 V were much less than 0.1% of Mn loading from the cathode and were comparable to the Mn loading on the negative electrode found after formation. For cells charged to 4.5 V, the Mn deposition was equal to or larger than 0.1% of the positive electrode loading. The cell containing MA also had a Mn loading close to double the loading of the cell without MA, yet both these cells had similar capacity fade (~20%). This suggests the capacity fade is independent of Mn dissolution.

Figure 5.3 shows the concentration of Li^+ in the electrolyte (a.) and the loading of Mn found on the negative electrode (b.) vs. capacity loss. For cells without MA, increasing capacity loss coincides with decreasing Li^+ concentration while cells with MA did not experience significant salt loss. These results suggest that capacity loss is independent of the Li^+ concentration, at least for the cells studied here.

Figure 5.3b shows the Mn deposition found at the negative electrode for cells both with and without MA vs. capacity loss. Like the observed trend between Mn deposition and capacity loss in found in cells discussed in Chapter 4, the results from this study follows a "hooked" trend. This trend appears independent of electrolyte composition, however, additional data points for cells containing MA and cells with more capacity loss are needed to identify a relationship.

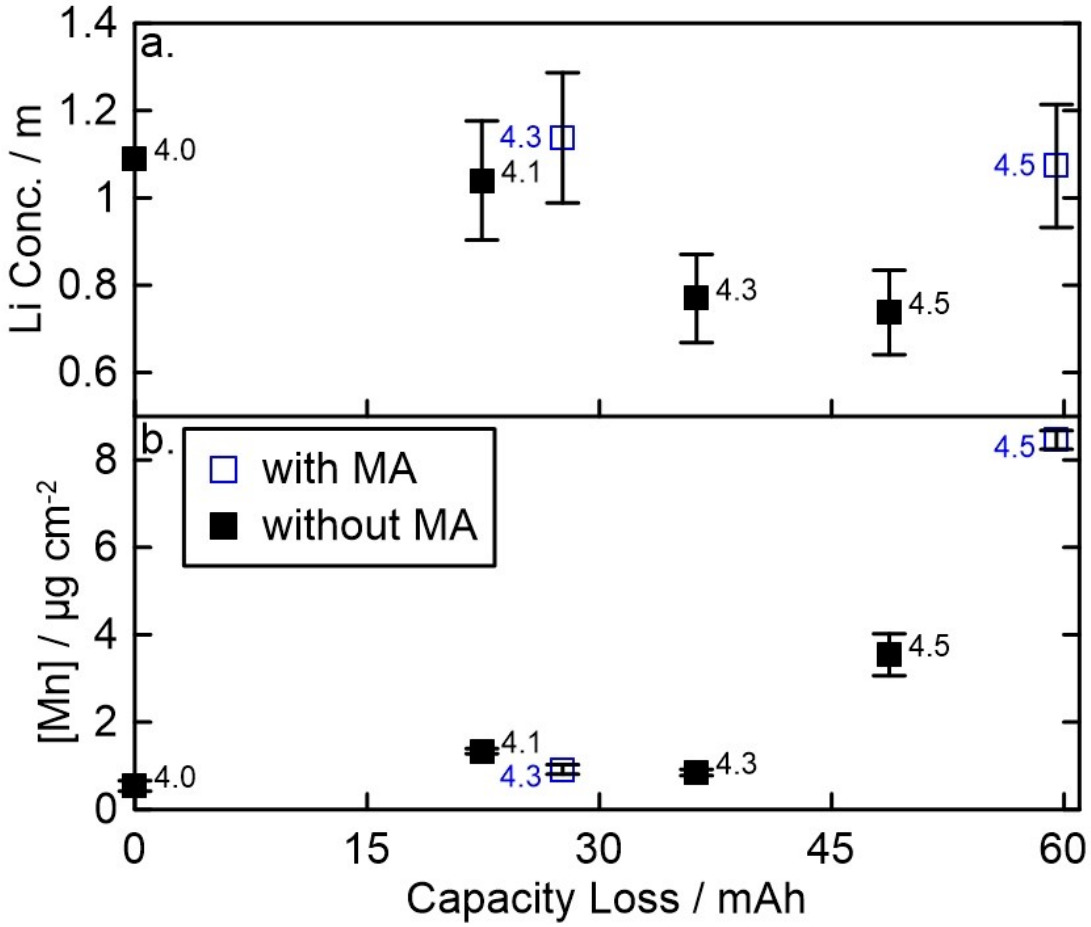

Figure 5.3 - a) Li^+ concentration in electrolyte post-cycling compared to capacity loss. b) Mn loading on the negative electrode compared to capacity loss.

Comparison to results from Gilbert et al.

Figure 5.4 compares the results for Mn deposition on the negative electrode to the data recently published on Mn deposition by Gilbert et al.[95] as discussed in Chapter 4. The cells cycled in this study experienced much more extreme cycling conditions including higher temperature and more cycle counts yet reached a maximum of only 24% capacity loss compared to the 37% reached by cells from Gilbert et al.[95] which experienced much less aggressive cycling conditions. Similar to the results in Chapter 4, Mn deposition appears

to follow a 'hooked' trend where the extent Mn deposition is constant after formation and as capacity loss increases until about 20% capacity loss where the Mn deposition suddenly increases. This contrasts Gilbert et al.'s conclusion that Mn deposition is directly proportional to capacity loss.

Also similar to results discussed in Chapter 4, cells in this study are far superior to the cells used by Gilbert et al.[95] The cycling history for these cells was more extreme, yet the capacity losses were less than Gilbert et al.'s cells cycled to 4.4 and 4.45 V.[95] This exemplifies that a well-designed electrolyte mixture and/or an improved positive electrode material, such as single crystal NMC532, can control Mn deposition.

The Li^+ concentration of the electrolyte and the Mn deposition at the negative electrode are compared to the increase in ΔV, or impedance growth, of the cells both with and without MA in Figure 5.5. A cell after 4.0 V formation is shown with $\Delta V = 0$. Figure 5.5a shows the Li^+ concentration measured in the electrolyte sample. For cells without MA, the increasing impedance coincides with a decrease in Li^+ electrolyte concentration. This relationship is not linear, suggesting loss of salt is not the primary contributor to impedance growth. However, the removal of Li^+ from the electrolyte has the potential to increase solution resistance by decreasing conductivity. Therefore, this relationship will require further study through electrochemical impedance spectroscopy and symmetrical cell studies. Figure 5.5a also shows that cells containing MA do not show a decrease in Li^+ concentration but rather retain their Li^+ concentrations even when impedance increases.

Figure 5.5b shows that the Mn deposition at the negative electrode is not directly proportional to the impedance growth within the range studied. Figure 5.5b also shows

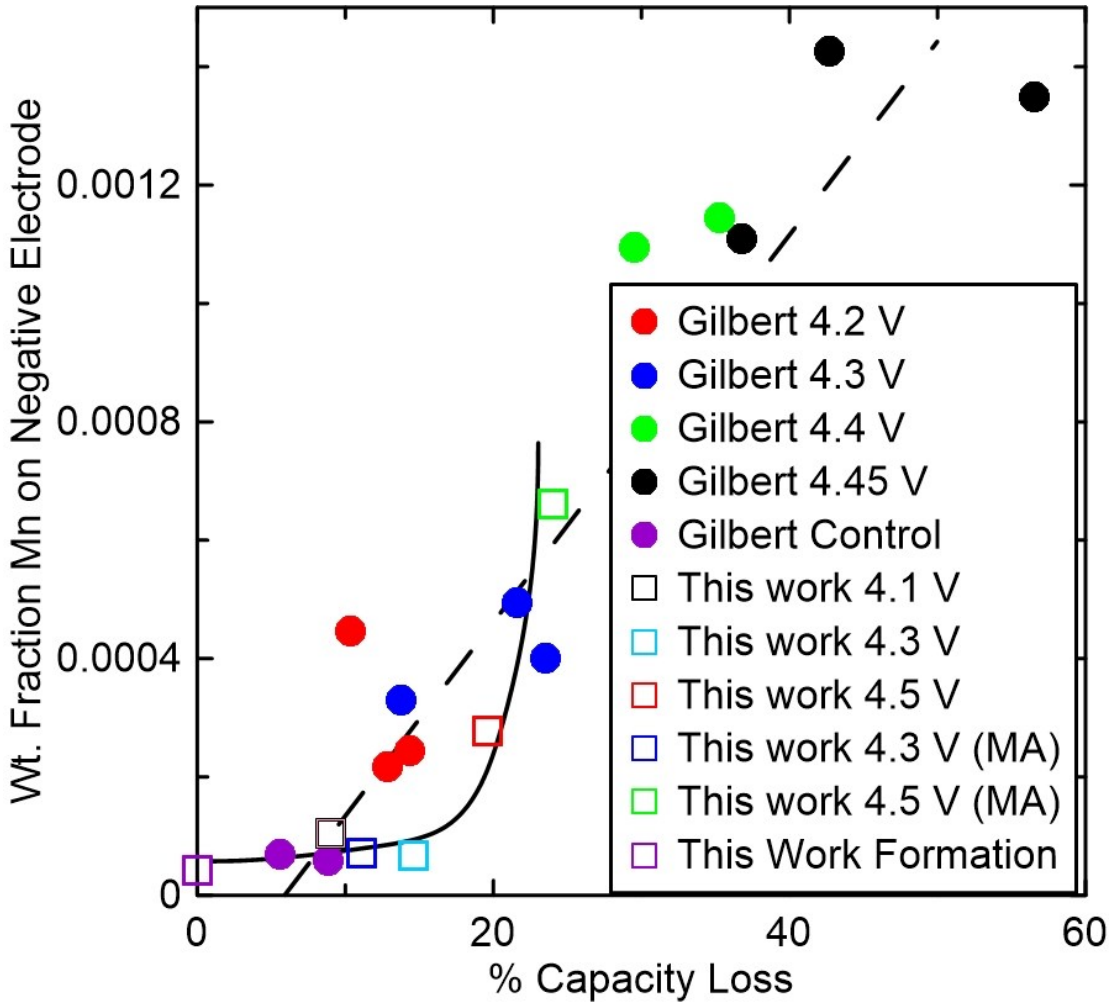

Figure 5.4 - Comparing results for Mn deposition on the negative electrode in this study to those from Gilbert et al.[95] The legend in the Figure indicates the upper cutoff voltage and which study the data points correspond to. Cells in the Gilbert et al. study were tested at 30ºC for 900 hours. Cells in this study were tested at 55ºC for 5000 hours.

that while the impedance increases in cells cycled to 4.5 V both with and without MA are comparable, the Mn deposition for the cell containing MA is double the deposition for the cell without MA. These findings suggest that Mn deposition is not primarily responsible for impedance growth.

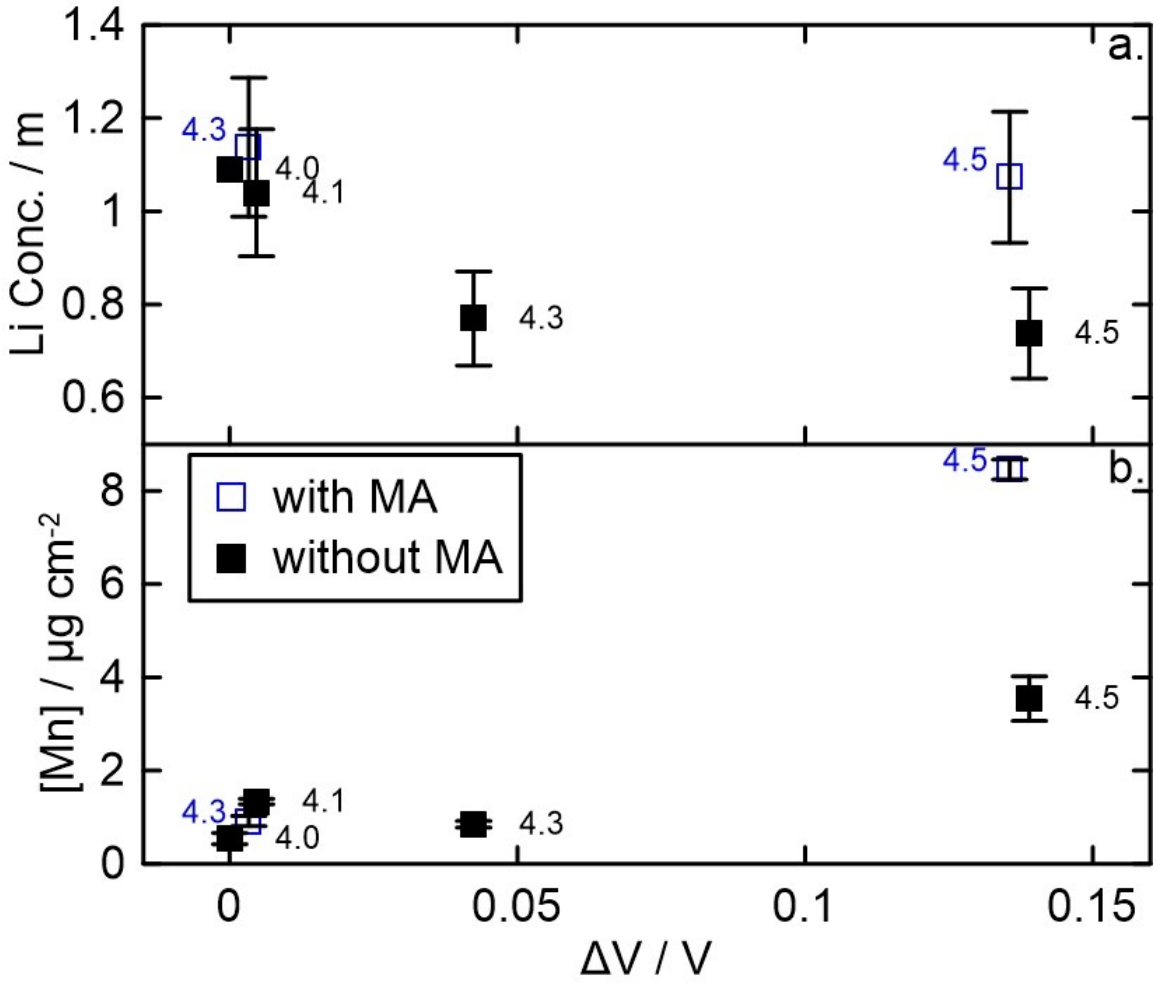

Figure 5.5 - a) Li^+ concentration in electrolyte post-cycling compared to increase in ΔV measured at the end of the charge-discharge testing shown in Figure 5.1b. b) Mn loading on the negative electrode compared to increase in ΔV.

Concluding remarks

The results from electrolyte analysis and negative electrode analysis for single crystal NMC532 cells charged and discharged for over 700 cycles were presented in this chapter. Two electrolyte mixtures were studied at various upper cutoff potentials.

Analyses of the Li^+ concentration in the electrolyte found that cells containing MA retained a Li^+ concentration comparable to the original concentration while the electrolyte studied

from cells without MA and that were charged to higher upper cutoff potentials experienced Li^+ loss. This loss must coincide with the removal of an anion from solution. Based on previous research, it is likely the removal of salt occurs between Li_2CO_3 and $LiPF_6$. The retention of salt concentration measured in MA containing cells indicates an alternative reduction and oxidation reaction occurs at the respective electrodes which does not increase Li_2CO_3 in solution. Future work is required to confirm the mechanism for Li^+ removal from solution and the relationship between MA and Li^+ retention.

Mn loadings found on the negative electrodes were measured for all cells and shown to equivalent to less than 0.1% of the positive electrode Mn loading. For cells cycled to 4.1 and 4.3 V, Mn loading at the negative electrode was comparable to the Mn loading found after cell formation. For this matrix, Mn deposition does not appear to contribute significantly to capacity loss.

These results of Mn deposition were compared to the results presented by Gilbert et al. Like the results discussed in Chapter 4, cells from this study did not indicate a linear relationship between Mn deposition and capacity loss.

6. CHAPTER 6 – CONCLUSIONS

Concluding remarks

Li-ion batteries are currently used for many portable electronics yet, if made more safe, affordable and long-lasting, the applications for Li-ion batteries could expand to more portable devices, more affordable electric vehicles and expanded electrical grid installations. In this work, the importance of the electrolyte was highlighted as a contributor to the SEI composition and as the Li-ion transport facilitator between both electrodes. A stable SEI layer is critical to long lifetime for cells while effective Li-ion transport can decrease overall cell resistance. The methods in Chapter 3 were developed to uncover the degradation reactions that occur in the electrolyte and in cells via reconstructing the electrolyte composition and allowing the electrodes to be recovered for further analysis.

The electrolyte extraction method, analysis methods and the proof of concepts were presented in Chapter 3. It was shown that the pure electrolyte could be centrifuged from the jelly roll without significant solvent loss and that with adequate time before analysis, is an accurate representation of the entire electrolyte. The existing GC-MS method could be modified to use this pure electrolyte and to quantify the fraction of organic solvents. Using the pure electrolyte, an additional organic solvent extraction could be used to quantify the fraction of MA. An aqueous extraction of the electrolyte could also be performed to measure Li^+ content via ICP-MS. Since the electrodes were not exposed to additional solvent, they were recovered for further analysis. In this work, the negative electrodes were recovered for μ-XRF analysis.

Chapters 4 and 5 discussed initial findings using the methods developed in this work. In Chapter 4, it was found that when the upper cutoff potential increased the fraction of transesterification increased. The lack of dimerization suggested that for these cells, the transesterification and dimerization processes do not rely on the same activating species. The small amount of Mn deposition at the negative electrode for most cells was comparable to the Mn deposition after formation.

The matrix in Chapter 5, which included two electrolyte mixtures, showed that the cells had comparable performance and impedance growth, however, the cells without MA experienced salt loss. The salt loss was likely due to $LiPF_6$ reacting with Li_2CO_3 to form mostly insoluble LiF and $LiPO_2F_2$. Further characterization of gas products and electrode surfaces will be required to identify the difference in salt consumption mechanisms between cells with and without MA. The amount of Mn deposition in cells both with and without MA is also comparable to that after formation, apart from cells cycled to 4.5 V.

Future work

Many additional studies are underway that contain cells destined for these analyses. These include plans to recreate the study using MA as a co-solvent. With the correct electrolyte, consistent analysis methods and an adequate number of cells, the fraction of transesterification can be calculated, the EC:EMC ratio can be determined, and pair cells can be reserved for periodic testing (for example, before and after cell failure).

Analysis is underway on another set of cells containing NMC622 positive electrodes and 1.1 m $LiPF_6$ in EC:EMC (3:7) with 2% VC. This matrix was also designed to include

cycling protocols and storage protocols with two different upper cutoff potentials (4.1 V and 4.3 V). Figure 6.1 shows the discharge capacity vs. cycle number for the cycled cells. The cells were either cycled or stored at three different temperatures (20°C, 40°C, 55°C). The storage cells are included to observe electrolyte reactions at the positive electrode. The results from this study will probe the effect of increased upper cutoff potential and increased temperature. The temperature study will potentially allow reaction kinetics to be determined. Half of these cells have been removed after 400 cycles and analyzed while the second half continued cycling and will be opened for analysis soon.

Another matrix in the process of cycling and disassembly includes both NMC532 (1.1 m $LiPF_6$ in EC:EMC (3:7) with 2%VC and 1% DTD) and NMC622 (1.1 m $LiPF_6$ in EC:EMC (3:7) with 2%VC, 1% methylene methanedisulfonate (MMDS) and 0.5% $LiPO_2F_2$ (LFO)) positive electrodes. This large matrix includes cells that are designated for cycling and storage at both 4.3 V and 4.4 V. Figure 6.2 and Figure 6.3 show the discharge capacity plotted vs. cycle number for NMC532 and NMC622 cells. The cells are stored or cycled at both 40°C and 55°C. Enough cells were formed so that cells could be removed every three months for one year (some cells since have been removed prematurely due to cell failure). The results from this study will not only show the effect of increased upper cutoff potentials and increased temperature but will provide a time dependent look at the electrolyte and negative electrode compositions throughout cycling or storage life.

Recently, the electrolyte centrifuge extraction method has been modified to be performed in a sealed pouch bag. After centrifuging, the lower section of the bag containing the electrolyte layer is heat sealed from the upper section containing the jelly roll. With this method, the electrodes can be recovered for symmetric cells, full cells, or XPS analysis.

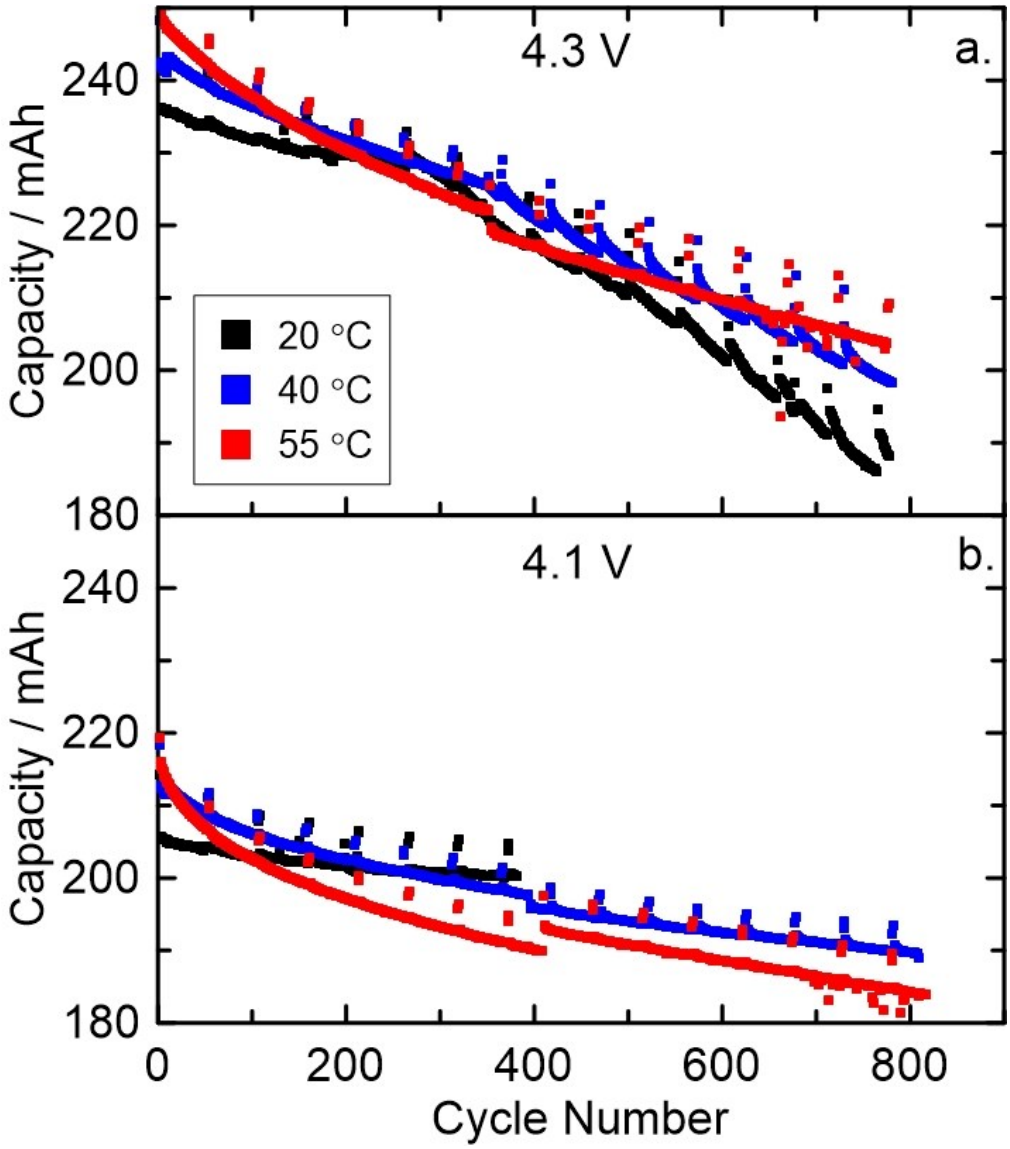

Figure 6.1 – Discharge capacity vs. cycle number for NMC532 cells with 1.1 m $LiPF_6$ in EC:EMC (3:7) and 2% VC + 1% DTD at 20℃ (black), 40℃ (blue), 55℃ (red) with a.) Upper cutoff potential of 4.3 V and b.) upper cuttof potential 4.1 V.

This will help determine the impedance contributions from the positive and negative electrodes for the large matrices of cells that are soon to be opened for analysis. For example, results from this analysis could confirm the difference in surface species on

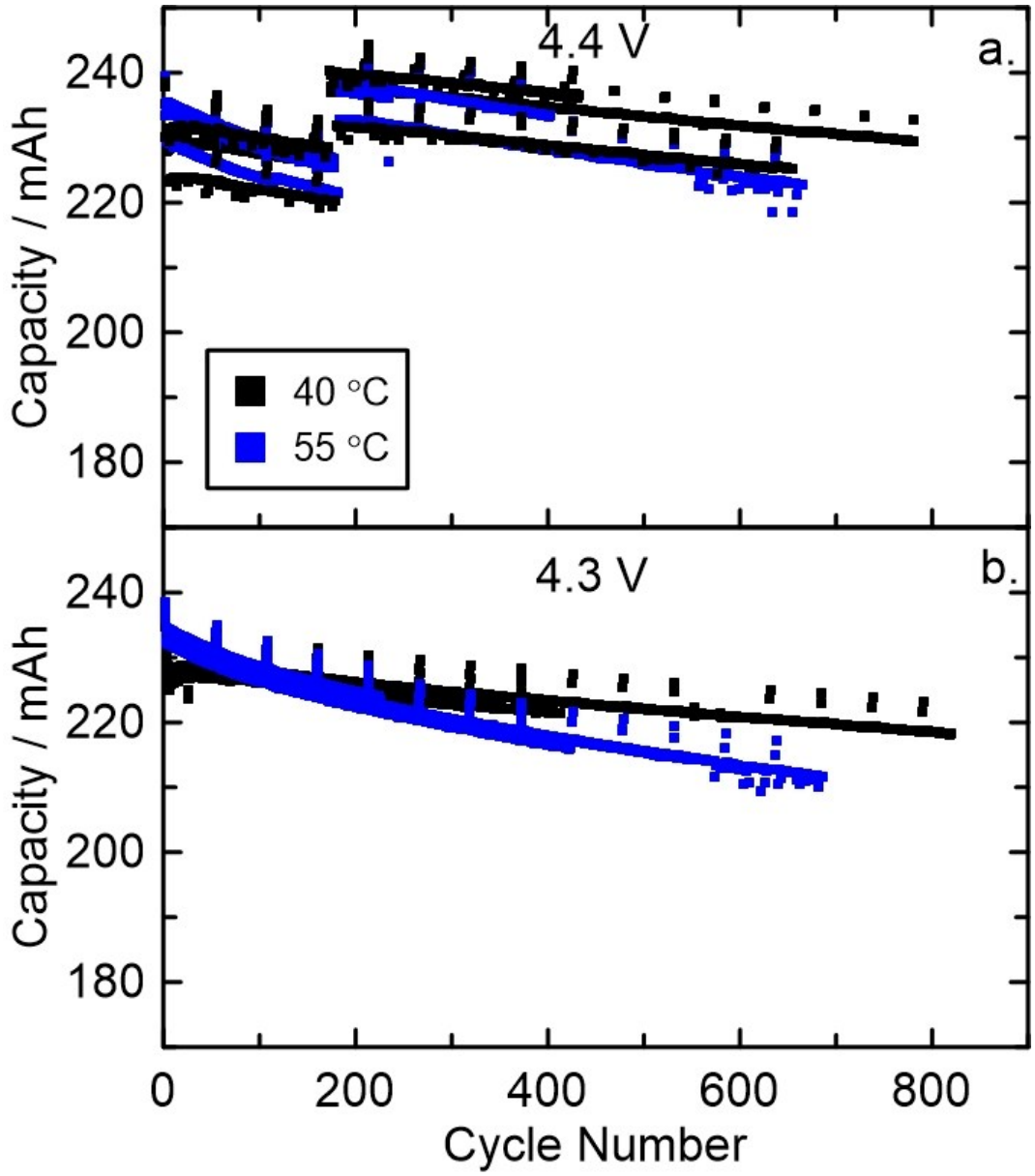

Figure 6.2 - Discharge capacity vs. cycle number for NMC532 cells containing 1.1 m $LiPF_6$ in EC:EMC (3:7) with 2% VC and 1% DTD cycled at 40°C and 55°C at upper cutoff potentials a.) 4.4 V and b.) 4.3 V.

electrodes from cells both with and without MA discussed in Chapter 5. This would help to identify the mechanism for electrolyte salt consumption in cells without MA and electrolyte salt retention in cells with MA.

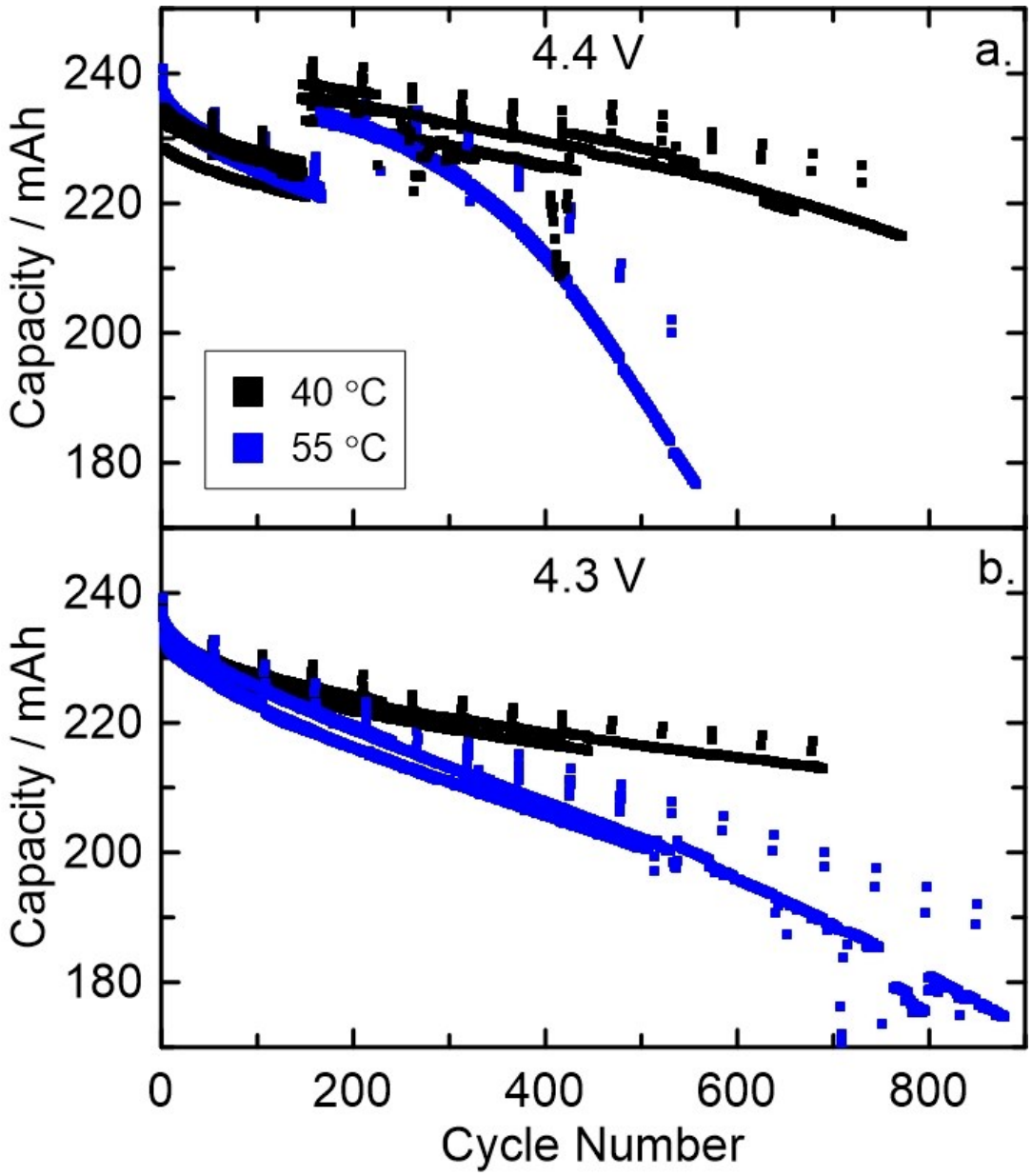

Figure 6.3 - Discharge capacity vs. cycle number for NMC622 cells containing 1.1 m $LiPF_6$ in EC:EMC (3:7) with 2% VC, 1% MMDS and 0.5% LFO cycled at 40°C (black) and 55°C (blue) at upper cutoff potentials a.) 4.4 V and b.) 4.3 V.

As gas is often a product of the electrolyte reactions, future work will likely include cells destined for gas characterization. The pouch bag extraction set up introduced in this chapter could potentially be modified to remove gas from a cell for characterization. This would

allow results including gas composition, electrolyte composition and electrode composition to be compared to proposed chemical mechanisms. The method would allow one cell to be used for analysis and for all components of the cell to be compared. Additionally, computationally models can be employed to evaluate the agreement between theoretical chemical reactions and the observed organic, inorganic and gaseous products.

Other techniques used for electrolyte characterization can be coupled with this work including Li-ion DTA[54] and Fourier transformed infra-red spectroscopy (FTIR).[104] DTA uses the reheating profile of a cell to track changes in salt and solvent content. This is nondestructive and can be performed at any stage of life.[54] The DTA results for a cell can be used to estimate the extent of electrolyte changes and to determine when to open a cell for the destructive GC-MS and ICP-MS analysis. FTIR has been explored as a method to measure salt and solvent composition using as little as a drop of electrolyte.[104] This method uses standards to characterize the infra-red absorption patterns of the salt and solvent bonds then to quantify an unknown electrolyte composition. The FTIR method is destructive but is a rapid way to measure organic and aqueous electrolyte components.

In the future, the methods developed in this work will also be used to measure changes to electrolyte that occur in cells with different electrode compositions. This could include an analysis of electrolyte from other positive electrode materials, such as NCA (Ni, Co and Al) as well as a comparison to results found in this work from NMC positive electrodes. Other electrode materials, such as Si-containing negative electrodes, could be studied to observe their effect on electrolyte composition. This would help identify potential electrode-electrolyte interactions different to the graphite interactions discussed in this work.

Like the pouch bag analysis discussed in Chapter 2,[57,58] the methods in this study could be used to compare the organic and salt content of electrolytes exposed to only one electrode and to both electrodes. This would isolate electrode and electrolyte reactions and help identify potential shuttle mechanisms that occur in the full cell.

Other new cell chemistries include the use of high-salt, non-flammable electrolytes (above 2-3 M) for cells with lithium metal negative electrodes.[105,106] These electrolytes can improve cycling lifetime and improve safety of cells by limiting dendrite growth.[105,106] Analysis of the electrolyte from these cells throughout their cycling life would identify the degradation mechanisms occurring in the liquid solution. This would include probing salt loss and solvent degradation for these high-salt chemistries.

The combined results from the work presented in this thesis as well as the large number of studies underway and planned will combine to identify the mechanisms that lead to failure of a wide variety of all cell chemistries.

REFERENCES

1. Nova Scotia Department of Energy Electricity System Review. **2015**, 1.

2. Click Energy 12 Countries Leading the Way in Renewable Energy. *https://www.clickenergy.com.au/news-blog/12-countries-leading-the-way-in-renewable-energy/* (accessed June 17, 2018).

3. EV Volumes Global Plug-In Sales. *http://www.ev-volumes.com/country/total-world-plug-in-vehicle-volumes/* (accessed June 17, 2018).

4. International Energy Agency Renewables. *https://www.iea.org/topics/renewables/* (accessed June 17, 2018).

5. Amin, A. Energy Storage and Renewables. *International Renewable Energy Agency* **2017**, 1-132.

6. Salomon, M.; Dahn, J.; Ehrlich, G. M.; Linden, D. *Linden's Handbook of Batteries;* McGraw-Hill: New York, 2011.

7. Ned Lithium and Lithium-Ion Battery Technology. *http://theelectricenergy.com/lithium-and-lithium-ion-battery/* (accessed June 18, 2018).

8. Smith, A. J.; Dahn, H.; Burns, J. C.; Dahn, J. R. Long-Term Low-Rate Cycling of $LiCoO_2$/Graphite Li-Ion Cells at 55°C. *J. Electrochem. Soc.* **2012***, 159*, A705.

9. King, A. Battery Builders Get the Cobalt Blues. *https://www.chemistryworld.com/news/battery-builders-get-the-cobalt-blues/3008738.article* (accessed June 18, 2018).

10. Xu, K. Nonaqueous Liquid Electrolytes for Lithium-Based Rechargeable Batteries. *Chem. Rev.* **2004***, 104*, 4303.

11. Foos, J. S.; McVeigh, J. Lithium Cycling in Polymethoxymethane Solvents. *J. Electrochem. Soc.* **1983***, 130*, 628.

12. Abraham, K. M.; Goldman, J. L.; Natwig, D. L. Characterization of Ether Electrolytes for Rechargeable Lithium Cells. *J. Electrochem. Soc.* **1982***, 129*, 2404.

13. Zhang, S. S.; Jow, T. R. Aluminum Corrosion in Electrolyte of Li-ion Battery. *J. Power Sources* **2002***, 109*, 458.

14. Nanjundiah, C.; Goldman, J. L.; Dominey, L. A.; Koch, V. R. Electrochemical Stability of $LiMF_6$ (M = P,As,Sb) in Tetrahydrofuran and Sulfolane. *J. Electrochem. Soc.* **1988***, 135*, 2914.

15. Angell, C. A.; Choi, Y. Crystallization and Vitrification in Aqueous Systems. *J. Microsc.* **1986***, 141*, 251.

16. Krause, L. J.; Lamanna, W.; Summerfield, J.; Engle, M.; Korba, G.; Loch, R.; Atanasoski, R. Corrosion of Aluminum at High Voltages in Non-aqueous Electrolytes Containing Perfluoroalkylsulfonyl Imides; New Lithium Salts for Lithium-ion Cells. *J. Power Sources* **1997***, 68*, 320.

17. Sloop, S. E.; Pugh, J. K.; Wang, S.; Kerr, J. B.; Kinoshita, K. Chemical Reactivity of PF_5 and $LiPF_6$ in Ethylene Carbonate/Dimethyl Carbonate Solutions. *Electrochemical and Solid-State Letters* **2001***, 4*, A42.

18. Kawamura, T.; Okada, S.; Yamaki, J. Decomposition Reaction of $LiPF_6$-based Electrolytes for Lithium ion Cells. *J. Power Sources* **2006***, 156*, 547.

19. Burns, J. C.; Sinha, N. N.; Jain, G.; Ye, H.; VanElzen, C. M.; Scott, E.; Xiao, A.; Lamanna, W. M.; Dahn, J. R. The Impact of Intentionally Added Water to the Electrolyte of Li-ion Cells. *J. Electrochem. Soc.* **2013***, 160*, A2281.

20. Burns, J. C.; Sinha, N. N.; Jain, G.; Ye, H.; VanElzen, C. M.; Scott, E.; Xiao, A.; Lamanna, W. M.; Dahn, J. R. The Impact of Intentionally Added Water to the Electrolyte of Li-Ion Cells II. Cells with Lithium Titanate Negative Electrodes. *J. Electrochem. Soc.* **2014***, 161*, A247.

21. Zaban, A.; Zinigrad, E.; Aurbach, D. Impedance Spectroscopy of Li Electrodes. 4. A General Simple Model of the Li-Solution Interphase in Polar Aprotic Systems. *J. Phys. Chem.* **1996***, 100*, 3089.

22. Aurbach, D.; Markovsky, B.; Salitra, G.; Markevich, E.; Talyossef, Y.; Koltypin, M.; Nazar, L.; Ellis, B.; Kovacheva, D. Review on Electrode-Electrolyte Solution Interactions, Related to Cathode Materials for Li-ion Batteries. *J. Power Sources* **2007***, 165*, 491.

23. Logan, E. R.; Tonita, E. M.; Gering, K. L.; Ma, L.; Bauer, M. K. G.; Li, J.; Beaulieu, L. Y.; Dahn, J. R. A Study of the Transport Properties of Ethylene Carbonate-Free Li Electrolytes. *J. Electrochem. Soc.* **2018***, 165*, A705.

24. Logan, E. R.; Tonita, E.; Gering, K. L.; Li, J.; Ma, X.; Beaulieu, L. Y.; Dahn, J. R. A Study of the Physical Properties of Li-Ion Battery Electrolytes Containing Esters. *J. Electrochem. Soc.* **2018***, 165*, A21.

25. Matsuda, Y.; Satake, H. Mixed Electrolyte Solutions of Propylene Carbonate and Dimethoxyethane for High Energy Density Batteries. *J. Electrochem. Soc.* **1980***, 127*, 877.

26. Ding, M. S.; Xu, K.; Zhang, S. S.; Amine, K.; Henriksen, G. L.; Jow, T. R. Change of Conductivity with Salt Content, Solvent Composition, and Temperature for Electrolytes of $LiPF_6$ in Ethylene Carbonate-Ethyl Methyl Carbonate. *J. Electrochem. Soc.* **2001***, 148*, A1196.

27. Ding, S. P.; Jow, T. R.; Xu, K. Toward Reliable Values of Electrochemical Stability Limits for Electrolytes. *J. Electrochem. Soc.* **1999***, 146*, 4172.

28. Ma, L.; Glazier, S. L.; Petibon, R.; Xia, J.; Peters, J. M.; Liu, Q.; Allen, J.; Doig, R. N. C.; Dahn, J. R. A Guide to Ethylene Carbonate-Free Electrolyte Making for Li-Ion Cells. *J. Electrochem. Soc.* **2017***, 164*, A5008.

29. Fong, R.; von Scacken, U.; Dahn, J. R. Studies of Lithium Intercalation into Carbons Using Nonaqueous Electrochemical Cells. *J. Electrochem. Soc.* **1990***, 137*, 2009.

30. Petibon, R.; Rotermund, L.; Nelson, K. J.; Gozdz, A. S.; Xia, J.; Dahn, J. R. Study of Electrolyte Components in Li Ion Cells Using Liquid-Liquid Extraction and Gas Chromatography Coupled with Mass Spectrometry. *J. Electrochem. Soc.* **2014***, 161*, A1167.

31. Strehle, B.; Solchenbach, S.; Metzger, M.; Schwenke, K. U.; Gasteiger, H. The Effect of CO_2 on Alkyl Carbonate Trans-Esterification during Formation of Graphite Electrodes in Li-Ion Batteries. *J. Electrochem. Soc.* **2017***, 164*, A2513.

32. Burns, J. C.; Kassam, A.; Sinha, N. N.; Downie, L. E.; Solnickova, L.; Way, B. A.; Dahn, J. R. Predicting and Extending the Lifetime of Li-Ion Batteries. *J. Electrochem. Soc.* **2013***, 160*, A1451.

33. Zhang, S. S. A Review on Electrolyte Additives for Lithium-ion Batteries. *J. Power Sources* **2006***, 162*, 1379.

34. Genieser, R.; Ferrari, S.; Loveridge, M.; Beattie, S. D.; Beanland, R.; Amari, H.; West, G.; Bhagat, R. Lithium ion batteries (NMC/graphite) cycling at 80 °C: Different Electrolytes and Related Degradation Mechanism. *J. Power Sources* **2018***, 373*, 172.

35. Campion, C. L.; Li, W.; Lucht, B. L. Thermal Decomposition of $LiPF_6$-Based Electrolytes for Lithium-Ion Batteries. *J. Electrochem. Soc.* **2005***, 152*, A2327.

36. Wilken, S.; Treskow, M.; Scheers, J.; Johansson, P.; Jacobsson, P. Initial Stages of Thermal Decomposition of $LiPF_6$- based Lithium-ion Battery Electrolytes by Detailed Raman and NMR Spectroscopy. *RSC Adv.* **2013***, 3*, 16359.

37. Nie, M.; Chalasani, D.; Abraham, D. P.; Chen, Y.; Bose, A.; Lucht, B. L. Lithium Ion Battery Graphite Solid Electrolyte Interphase Revealed by Microscopy and Spectroscopy. *J. Phys. Chem. C* **2013***, 117*, 1257.

38. Onuki, M.; Kinoshita, S.; Sakata, Y.; Yanagidate, M.; Otake, Y.; Ue, M.; Deguchi, M. Identification of the Source of Evolved Gas in Li-Ion Batteries Using ^{13}C-labeled Solvents. *J. Electrochem. Soc.* **2008***, 155*, A794.

39. Verma, P.; Maire, P.; Novák, P. A Review of the Features and Analyses of the Solid Electrolyte Interphase in Li-ion Batteries. *Electrochim. Acta* **2010***, 55*, 6332.

40. Sasaki, T.; Abe, T.; Iriyama, Y.; Inaba, M.; Ogumi, Z. Formation Mechanism of Alkyl Dicarbonates in Li-ion Cells. *J. Power Sources* **2005***, 150*, 208.

41. Yoshida, H.; Fukunaga, T.; Hazama, T.; Terasaki, M.; Mizutani, M.; Yamachi, M. Degradation Mechanism of Alkyl Carbonate Solvents Used in Lithium-ion Cells During Initial Charging. *J. Power Sources* **1997***, 68*, 311.

42. G. Gachot; P. Ribière; D. Mathiron; S. Grugeon; M. Armand; J. Leriche; S. Pilard; S. Laruelle Gas Chromatography/Mass Spectrometry As a Suitable Tool for the Li-Ion Battery Electrolyte Degradation Mechanisms Study. *Analytical Chemistry* **2011***, 83*, 478.

43. Zhang, B.; Metzger, M.; Solchenbach, S.; Payne, M.; Meini, S.; Gasteiger, H. A.; Garsuch, A.; Lucht, B. L. Role of 1,3-Propane Sultone and Vinylene Carbonate in Solid Electrolyte Interface Formation and Gas Generation. *J. Phys. Chem. C* **2015***, 119*, 11337.

44. Takeuchi, E. S.; Gan, H.; Palazzo, M.; Leising, R. A.; Davis, S. M. Anode Passivation and Electrolyte Solvent Disproportionation: Mechanism of Ester Exchange Reaction in Lithium-Ion Batteries. *J. Electrochem. Soc.* **1997***, 144*, 1944.

45. Kim, H.; Grugeon, S.; Gachot, G.; Armand, M.; Sannier, L.; Laruelle, S. Ethylene bis-Carbonates as Telltales of SEI and Electrolyte Health, Role of Carbonate Type and New Additives. *Electrochimica Acta* **2014***, 136*, 157.

46. Peng, H. J.; Urbonaite, S.; Villevieille, C.; Wolf, H.; Leitner, K.; Novák, P. Consequences of Electrolyte Degradation for the Electrochemical Performance of $Li_{1+x}(Ni_aCo_bMn_{1-a-b})_{1-x}O_2$. *J. Electrochem. Soc.* **2015***, 162*, A7072.

47. Petibon, R.; Chevrier, V. L.; Aiken, C. P.; Hall, D. S.; Hyatt, S. R.; Shunmugasundaram, R.; Dahn, J. R. Studies of the Capacity Fade Mechanisms of $LiCoO_2$/Si-Alloy: Graphite Cells. *J. Electrochem. Soc.* **2016***, 163*, A1146.

48. Besenhard, J. O.; Wagner, M. W.; Winter, M.; Jannakoudakis, A. D.; Jannakoudakis, P. D.; Theodoridou, E. Inorganic Film-forming Electrolyte Additives Improving the Cycling Behaviour of Metallic Lithium Electrodes and the Self-discharge of Carbon-Lithium Electrodes. *J. Power Sources* **1993***, 44*, 413.

49. Petibon, R.; Xia, J.; Burns, J. C.; Dahn, J. R. Study of the Consumption of Vinylene Carbonate in $LiNi_{0.33}Mn_{0.33}Co_{0.33}]O_2$/Graphite Pouch Cells. *J. Electrochem. Soc.* **2014***, 161*, A1618.

50. Sloop, S. E.; Kerr, J. B.; Kinoshita, K. The Role of Li-ion Battery Electrolyte Reactivity in Performance Decline and Self-Discharge. *J. Power Sources* **2003***, 119*, 330.

51. Christe, K. O.; Dixon, D. A.; McLemore, D.; Wilson, W. W.; Sheehy, J. A.; Boatz, J. A. On a Quantitative Scale for Lewis Acidity and Recent Progress in Polynitrogen Chemistry. *J. Fluorine Chem.* **2000***, 101*, 151.

52. Kim, G. Interaction Between Cathode and Anode and its Impact on the Production of Alkyl Dicarbonates in Lithium Ion Batteries. *Electrochimica Acta* **2016***, 200*, 46.

53. Li, W.; Lucht, B. L. Inhibition of the Detrimental Effects of Water Impurities in Lithium-Ion Batteries. *Electrochemical and Solid-State Letters* **2007***, 10*, A115.

54. Day, R. P.; Xia, J.; Petibon, R.; Rucska, J.; Wang, H.; Wright, A. T. B.; Dahn, J. R. Differential Thermal Analysis of Li-Ion Cells as an Effective Probe of Liquid Electrolyte Evolution during Aging. *J. Electrochem. Soc.* **2015***, 162*, A2577.

55. Richard, M. N.; Dahn, J. R. Accelerating Rate Calorimetry Study on the Thermal Stability of Lithium Intercalated Graphite in Electrolyte. I. Experimental. *J. Electrochem. Soc.* **1999***, 146*, 2068.

56. Andersson, A. M.; Edstram, K. Chemical Composition and Morphology of the Elevated Temperature SEI on Graphite. *J. Electrochem. Soc.* **2001***, 148*, A1100.

57. Xiong, D. J.; Petibon, R.; Nie, M.; Ma, L.; Xia, J.; Dahn, J. R. Interactions between Positive and Negative Electrodes in Li-Ion Cells Operated at High Temperature and High Voltage. *J. Electrochem. Soc.* **2016***, 163*, A546.

58. Xiong, D. J.; Ellis, L. D.; Petibon, R.; Hynes, T.; Liu, Q. Q.; Dahn, J. R. Studies of Gas Generation, Gas Consumption and Impedance Growth in Li-Ion Cells with Carbonate or Fluorinated Electrolytes Using the Pouch Bag Method. *J. Electrochem. Soc.* **2017***, 164*, A340.

59. Ikeda, S.; Takagi, T.; Ito, K. Selective Formation of Formic Acid, Oxalic Acid, and Carbon Monoxide by Electrochemical Reduction of Carbon Dioxide. *Bull. Chem. Soc. Jpn.* **1987***, 60*, 2517.

60. Amatore, C.; Saveant, J. M. Mechanism and Kinetic Characteristics of the Electrochemical Reduction of Carbon Dioxide in Media of Low Proton Availability. *J. Am. Chem. Soc.* **1981***, 103*, 5021.

61. L. D. Ellis; J. P. Allen; L. M. Thompson; J. E. Harlow; W. J. Stone; Hill, I. G.; Dahn, J. R. Quantifying, Understanding and Evaluating the Effects of Gas Consumption in Lithium-Ion Cells. *J. Electrochem. Soc.* **2017***, 164*, A3518.

62. Dedryvere, R.; Foix, D.; Franger, S.; Patoux, S.; Daniel, L.; Gonbeau, D. Electrode/Electrolyte Interface Reactivity in High-Voltage Spinel $LiMn_{1.6}Ni_{0.4}O_4/Li_4Ti_5O_{12}$ Lithium-Ion Battery. *J. Phys. Chem. C* **2010***, 114*, 10999.

63. Wang, E.; Ofer, D.; Bowden, W.; Iltchev, N.; Moses, R.; Brandt, K. Stability of Lithium Ion Spinel Cells. III. Improved Life of Charged Cells. *J. Electrochem. Soc.* **2000***, 147*, 4023.

64. Nitta, N.; Wu, F.; Lee, J. T.; Yushin, G. Li-ion Battery Materials: Present and Future. *Materials Today* **2015***, 18*, 252.

65. Gu, M.; Belharouak, I.; Zheng, J.; Wu, H.; Xiao, J.; Genc, A.; Amine, K.; Thevuthasan, S.; Baer, D. R.; Zhang, J.; Browning, N. D.; Liu, J.; Wang, C. Formation of the Spinel Phase in the Layered Composite Cathode Used in Li-ion Batteries. *ACS nano* **2013***, 7*, 760.

66. Zhan, C.; Wu, T.; Lu, J.; Amine, K. Dissolution, Migration, and Deposition of Transition Metal Ions in Li-ion Batteries Exemplified by Mn-based Cathodes - A Critical Review. *Energy Environ. Sci.* **2018***, 11*, 243.

67. Jarry, A.; Gottis, S.; Yu, Y.; Roque-Rosell, J.; Kim, C.; Cabana, J.; Kerr, J.; Kostecki, R. The Formation Mechanism of Fluorescent Metal Complexes at the $Li_xNi_{0.5}Mn_{1.5}O_{4\text{-delta}}$/Carbonate Ester Electrolyte Interface. *J. Am. Chem. Soc.* **2015***, 137*, 3533.

68. Zhan, C.; Lu, J.; Kropf, A. J.; Wu, T.; Jansen, A. N.; Sun, Y.; Qiu, X.; Amine, K. Mn(II) Deposition on Anodes and its Effects on Capacity Fade in Spinel Lithium Manganate-carbon Systems. *Nat. Commun.* **2013***, 4*, 2437.

69. Zheng, T.; Gozdz, A. S.; Amatucci, G. G. Reactivity of the Solid Electrolyte Interface on Carbon Electrodes at Elevated Temperatures. *J. Electrochem. Soc.* **1999***, 146*, 4014.

70. Jang, D. H.; Shin, Y. J.; Oh, S. M. Dissolution of Spinel Oxides and Capacity Losses in 4 V Li/Li x Mn_2O_4 Cells. *J. Electrochem. Soc.* **1996***, 143*, 2204.

71. Xia, Y.; Zhou, Y.; Yoshio, M. Capacity Fading on Cycling of 4 V $Li/LiMn_2O_4$ Cells. *J. Electrochem. Soc.* **1997***, 144*, 2593.

72. Li, J.; Cameron, A. R.; Li, H.; Glazier, S.; Xiong, D.; Chatzidakis, M.; Allen, J.; Botton, G. A.; Dahn, J. R. Comparison of Single Crystal and Polycrystalline $LiNi_{0.5}Mn_{0.3}Co_{0.2}O_2$ Positive Electrode Materials for High Voltage Li-Ion Cells. *J. Electrochem. Soc.* **2017**, *164*, A1534.

73. Burns, J. C.; Petibon, R.; Nelson, K. J.; Sinha, N. N.; Kassam, A.; Way, B. M.; Dahn, J. R. Studies of the Effect of Varying Vinylene Carbonate (VC) Content in Lithium Ion Cells on Cycling Performance and Cell Impedance. *J. Electrochem. Soc.* **2013**, *160*, A1668.

74. Nelson, K. J.; d'Eon, G. L.; Wright, A. T. B.; Ma, L.; Xia, J.; Dahn, J. R. Studies of the Effect of High Voltage on the Impedance and Cycling Performance of LiNi0.4Mn0.4Co0.2]O2/Graphite Lithium-Ion Pouch Cells. *J. Electrochem. Soc.* **2015**, *162*, A1054.

75. Aiken, C. P.; Xia, J.; Wang, D.; Stevens, D. A.; Trussler, S.; Dahn, J. R. An Apparatus for the Study of In Situ Gas Evolution in Li-Ion Pouch Cells. *J. Electrochem. Soc.* **2014**, *161*, A1548.

76. Danzer, K. *Analytical Chemistry: Theoretical and Metrological Fundamentals;* Springer: Berlin, NY, 2007.

77. Schultz, C.; Vedder, S.; Streipert, B.; Winter, M.; Nowak, S. Quantitative Investigation of the Decomposition of Organic Lithium Ion Battery Electrolytes with LC-MS/MS. *RCS Adv.* **2017**, *7*, 27853.

78. Dettmer-Wilde, K.; Engewald, W.; Adachour, M. *Practical Gas Chromatography: A Comprehensive Reference;* Springer: Berlin, 2014.

79. Agilent Technologies J and W Column Selection Guide. *https://www.agilent.com/cs/library/catalogs/public/5990-9867EN_GC_CSG.pdf* (accessed May 22, 2018).

80. Hiraoka, K. *Fundamentals of Mass Spectrometry;* Springer: New York, NY, 2013.

81. Bruice, P. Y. *Organic Chemistry;* Pearson: Glenview, IL, USA, 2011; , pp 501.

82. Ashcroft, A. E. *Ionization Methods in Organic Mass Spectrometry;* Royal Society of Chemistry: Cambridge, UK, 1997.

83. Millour, S.; Noel, L.; Kadar, A.; Chekri, R.; Vastel, C.; Guerin, T. Simultaneous Analysis of 21 Elements in Foodstuffs by ICP-MS After Closed-Vessel Microwave Digestion: Method Validation. *Journal of Food Composition and Analysis* **2011**, *24*, 111.

84. Ogra, Y.; Hirata, T. *Metallomics: Recent Analytical Techniques and Applications;* Springer: Tokyo, Japan, 2017.

85. Hill, S. J. *Inductively Coupled Plasma Spectrometry and its Applications;* Oxford: Ames, Iowa, 2006.

86. Thermo Scientific *iCAP Q Operating Manual;* Thermo Fisher Scientific Inc.: Waltham, MA, USA, 2012.

87. Smith, N. K. Investigating the Association between Arsenic Exposure and Chronic Disease Using Toenail Speciation Biomarkers: A Pilot Study in Atlantic Canada, M.Sc. Thesis - Dalhousie University, 2017.

88. Danzer, K. *Analytical Chemistry: Theoretical and Metrological Fundamentals;* Springer: New York, NY, 2007.

89. Dahn, J. R.; Trussler, S.; Hatchard, T. D.; Bonakdarpour, A.; Mueller-Neuhaus, J. R.; Hewitt, K. C.; Fleischauer, M. Economical Sputtering System To Produce Large-Size Composition-Spread Libraries Having Linear and Orthogonal Stoichiometry Variations. *Chemistry of Materials* **2002***, 14*, 3519.

90. Bruker Periodic Table of Elements and X-ray Energies. *https://www.bruker.com/fileadmin/user_upload/8-PDF-Docs/X-rayDiffraction_ElementalAnalysis/HH-XRF/Misc/Periodic_Table_and_X-ray_Energies.pdf* (accessed June 12, 2018).

91. Prince, E. *International Tables for Crystallography, Mathematical, Physical and Chemical Tables;* Wiley: 2004.

92. Speight, S. C.; Lentz, D. R.; McFarlane, C. R. M. Petrographic and µ-XRF study of the Kam Group lithologies in the Au-bearing Yellowknife greenstone belt, Northwest Territories, Canada. *Mineral Rescources to Discover* **2017***, 1*, 191.

93. Pieczonka, N.; Liu, Z.; Lu, P.; Olsen, K. L.; Moote, J.; Powell, B. R.; Kim, J. H. Understanding Transition-Metal Dissolution Behavior in $LiNi_{0.5}Mn_{1.5}O_4$ High-Voltage Spinel for Lithium Ion Batteries. *J. Phys. Chem. C* **2013***, 117*, 15947.

94. Zhang, X.; Ross, P. N.; Kostecki, R.; Kong, F.; Sloop, S.; Kerr, J. B.; Striebel, K.; Cairns, E. J.; McLarnon, F. Diagnostic Characterization of High Power Lithium-Ion Batteries for Use in Hybrid Electric Vehicles. *J. Electrochem. Soc.* **2001***, 148*, A463.

95. Gilbert, J.; Shkrob, I.; Abraham, D. Transition Metal Dissolution, Ion Migration, Electrocatalytic Reduction and Capacity Loss in Lithium-Ion Full Cells. *J. Electrochem. Soc.* **2017***, 164*, A389.

96. Banerjee, A.; Ziv, B.; Shilina, Y.; Luski, S.; Aurbach, D.; Halalay, I. C. Acid-Scavenging Separators: A Novel Route for Improving Li-Ion Batteries' Durability. *ACS Energy Lett.* **2017***, 2*, 2388.

97. Li, W.; Lucht, B. L. Inhibition of the Detrimental Effects of Water Impurities in Lithium-Ion Batteries. *Electrochemical and Solid-State Letters* **2007***, 10*, A115.

98. Li, J.; Cameron, A. R.; Li, H.; Glazier, S.; Xiong, D.; Chatzidakis, M.; Allen, J.; Botton, G. A.; Dahn, J. R. Comparison of Single Crystal and Polycrystalline $LiN_{i0.5}Mn_{0.3}Co_{0.2}O_2$ Positive Electrode Materials for High Voltage Li-Ion Cells. *J. Electrochem. Soc.* **2017***, 164*, A1534.

99. Ma, X.; Li, J.; Glazier, S.; Ma, L.; Gering, K.; Dahn, J. R. A Study of Highly Conductive Ester Co-solvents in $Li[Ni_{0.5}Mn_{0.3}Co_{0.2}]O_2$ /Graphite Pouch Cells. *Electrochim. Acta* **2018***, 270*, 215.

100. Glazier, S. L.; Li, J.; Ma, X.; Ellis, L. D.; Allen, J. P.; Gering, K. L.; Dahn, J. R. The Effect of Methyl Acetate, Ethylene Sulfate, and Carbonate Blends on the Parasitic Heat Flow of NMC532/Graphite Lithium Ion Pouch Cells. *J. Electrochem. Soc.* **2018***, 165*, A867.

101. Li, J.; Li, H.; Ma, X.; Stone, W.; Glazier, S.; Logan, E.; Tonita, E. M.; Gering, K. L.; Dahn, J. R. Methyl Acetate as a Co-Solvent in NMC532/Graphite Cells. *J. Electrochem. Soc.* **2018***, 165*, A1027.

102. Ma, L.; Ellis, L.; Glazier, S. L.; Ma, X.; Liu, Q.; Li, J.; Dahn, J. R. $LiPO_2F_2$as an Electrolyte Additive in $Li[Ni_{0.5}Mn_{0.3}Co_{0.2}]O_2$/Graphite Pouch Cells. *J. Electrochem. Soc.* **2018***, 165*, A891.

103. Zhang, S. S. Insight into the Gassing Problem of Li-ion Battery. *Frontiers in Energy Research* **2014***, 2*, 59.

104. Ellis, L. D.; Buteau, S.; Hames, S. G.; Thompson, L. M.; Hall, D. S.; Dahn, J. R. A New Method for Determining the Concentration of Electrolyte Components in Lithium-Ion Cells, Using Fourier Transform Infrared Spectroscopy and Machine Learning. *J. Electrochem. Soc.* **2018***, 165*, A256.

105. Suo, L.; Hu, Y.; Li, H.; Armand, M.; Chen, L. A New Class of Solvent-in-Salt Electrolyte for High-Energy Rechargeable Metallic Lithium Batteries. *Nature Communications* **2013***, 4*, 1481.

106. Matsumoto, K.; Nakahara, K.; Inoue, K.; Iwasa, S.; Nakano, K.; Kaneko, S.; Ishikawa, H.; Utsugi, K.; Yuge, R. Performance Improvement of Li Ion Battery with Non-Flammable TMP Mixed Electrolyte by Optimization of Lithium Salt Concentration and SEI Preformation Technique on Graphite Anode. *J. Electrochem. Soc.* **2014***, 161*, A831.

APPENDIX A – LICENSE AGREEMENTS

Electrochemical Society, Inc LICENSE TERMS AND CONDITIONS

Jul 12, 2018

This is a License Agreement between Lauren Thompson ("You") and Electrochemical Society, Inc ("Electrochemical Society, Inc") provided by Copyright Clearance Center ("CCC"). The license consists of your order details, the terms and conditions provided by Electrochemical Society, Inc, and the payment terms and conditions.

All payments must be made in full to CCC. For payment instructions, please see information listed at the bottom of this form.

License Number	4385020687724
License date	Jul 09, 2018
Licensed content publisher	Electrochemical Society, Inc
Licensed content title	Journal of the Electrochemical Society
Licensed content date	Jan 1, 1948
Type of Use	Thesis/Dissertation
Requestor type	Academic institution
Format	Print, Electronic
Portion	chart/graph/table/figure
Number of charts/graphs/tables/figures	1
The requesting person/organization is:	Lauren Thompson
Title or numeric reference of the portion(s)	Changes to the Electrolyte in Aged Li-ion cells, Chapter 2, Figure 2.1
Title of the article or chapter the portion is from	Change of Conductivity with Salt Content, Solvent Composition, and Temperature for Electrolytes of LiPF6 in Ethylene Carbonate-Ethyl Methyl Carbonate
Editor of portion(s)	N/A
Author of portion(s)	M. S. Ding, K. Xu, s. s. Zhang, K. Amine, G. L. Henriksen, and T. R. Jow
Volume of serial or monograph.	140
Issue, if republishing an article from a serial	10
Page range of the portion	A1197
Publication date of portion	September 13, 2001
Rights for	Main product
Duration of use	Current edition and up to 5 years
Creation of copies for the disabled	no
With minor editing privileges	no
For distribution to	Worldwide
In the following language(s)	Original language of publication
With incidental promotional use	no
The lifetime unit quantity of new product	Up to 499
Title	Changes to the Electrolyte in Aged Li-ion cells
Instructor name	Jeff Dahn
Institution name	Dalhousie University
Expected presentation date	Aug 2018
Billing Type	Invoice
Billing Address	Lauren Thompson 2364 Creighton St - Unit 2 Halifax, NS B3K 3R9 Canada Attn: Lauren Thompson
Total (may include CCC user fee)	0.00 USD

Electrochemical Society, Inc LICENSE TERMS AND CONDITIONS

Jul 12, 2018

This is a License Agreement between Lauren Thompson ("You") and Electrochemical Society, Inc ("Electrochemical Society, Inc") provided by Copyright Clearance Center ("CCC"). The license consists of your order details, the terms and conditions provided by Electrochemical Society, Inc, and the payment terms and conditions.

All payments must be made in full to CCC. For payment instructions, please see information listed at the bottom of this form.

License Number	4385041150984
License date	Jul 09, 2018
Licensed content publisher	Electrochemical Society, Inc
Licensed content title	Journal of the Electrochemical Society
Licensed content date	Jan 1, 1948
Type of Use	Thesis/Dissertation
Requestor type	Academic institution
Format	Print, Electronic
Portion	chart/graph/table/figure
Number of charts/graphs/tables/figures	1
The requesting person/organization is:	Lauren Thompson
Title or numeric reference of the portion(s)	Changes to the Electrolyte in Aged Li-ion cells, Chapter 2, Figure 2.2
Title of the article or chapter the portion is from	A Guide to Ethylene Carbonate-Free Electrolyte Making for Li-Ion Cells
Editor of portion(s)	N/A
Author of portion(s)	Lin Ma, S. L. Glazier, R. Petibon, Jian Xia, Jeremy M. Peters, Q. Liu, J. Allen, R. N. C. Doig, J. R. Dahn
Volume of serial or monograph.	164
Issue, if republishing an article from a serial	1
Page range of the portion	A5010
Publication date of portion	November 17, 2016
Rights for	Main product
Duration of use	Current edition and up to 5 years
Creation of copies for the disabled	no
With minor editing privileges	yes
For distribution to	Worldwide
In the following language(s)	Original language of publication
With incidental promotional use	no
The lifetime unit quantity of new product	Up to 499
Title	Changes to the Electrolyte in Aged Li-ion cells
Instructor name	Jeff Dahn
Institution name	Dalhousie University
Expected presentation date	Aug 2018
Billing Type	Invoice
Billing Address	Lauren Thompson 2364 Creighton St - Unit 2 Halifax, NS B3K 3R9 Canada Attn: Lauren Thompson
Total (may include CCC user fee)	0.00 USD